Study on high-quality food storage system for low carbon transport

by

Tao Zeng

A dissertation submitted to the graduate faculty in partial fulfillment of the requirements for the degree of
DOCTOR OF PHILOSOPHY

Major: Chemical Engineering

Academic Advisor: Associate Prof. Noriyuki Kobayashi

Nagoya University

2018

Contents

Chapter 1. Introduction

In this thesis, the development of a refrigerated container to realize long-term preservation transportation of agricultural products, together with the effective heat utilization of the transportation system has been experimentally investigated. The storage characteristics of agricultural products were examined; the effects of storage temperature and humidity on fresh commodities quality were experimentally obtained. An optimized storage condition to realize long-term preservation transportation of the container for agricultural and marine products has been developed. Furthermore, to effectively utilize the exhaust heat from the storage system, the performance of an activated carbon-ammonia adsorption refrigeration system has been experimentally investigated. Finally, the evaluation of performance of thermal and electrical hybrid adsorption chiller cycles with mechanical booster pumps has also been analyzed.

In the following sections of this chapter, background information regarding world energy and environmental issues, agricultural and marine products is briefly introduced. The motivations for studying on the development of a refrigerated container to realize long-term preservation transportation of agricultural and marine products are then summarized. Finally, the objectives and outline of this thesis are presented.

1.1 Background

1.1.1 Energy and environmental issues

Coal, petroleum, natural gas, renewables, hydro, and nuclear are consisted as the basic sources of energy in the world. With the rapid economic development and population explosion of recent decades, the global primary energy demand has dramatically increased. BP energy has summarized the global primary energy demand from 1970 to 2040, as shown in Figure 1-1 (2018 BP Energy Outlook, BP Global [1]). The global primary energy demand is predicted to grow from 13276 Mtoe in 2016 to 17983 Mtoe by 2040, an increase of 35.5%, with annual increasing ratio of 1.3%. Coal, petroleum, and natural gas are still the main energy sources all over the world, and account for more than half of the global energy

in 2040. Among them, oil, gas, and coal consumption amounts are predicting to change from 97 Mtoe to 105 Mtoe, 342 Mtoe to 502 Mtoe, 3732 Mtoe to 3762 Mtoe from 2016 to 2040, with a change ratio of 11.7 %, 46.7 %, and 0.8 %, respectively.

Billion toe
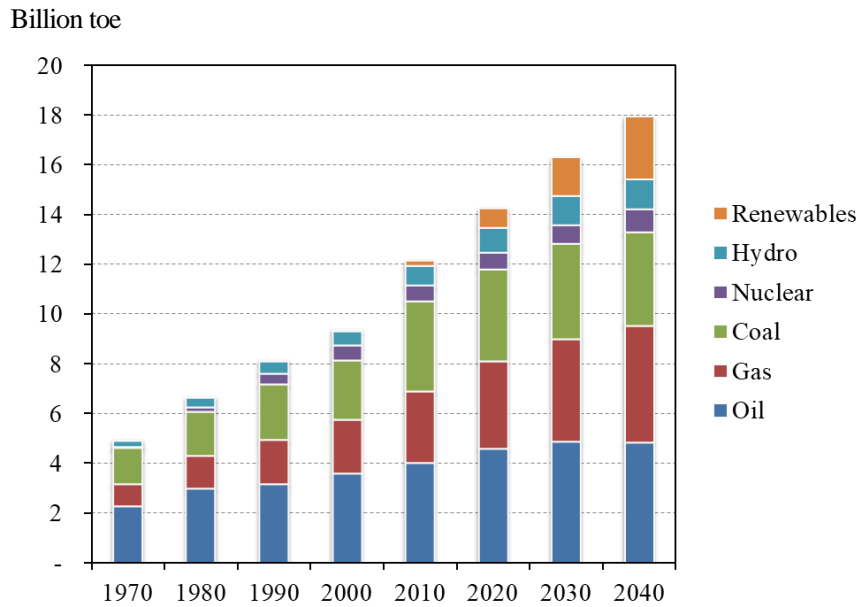
Figure 1-1. Primary energy demand by fuel (from BP Global, 2018 BP Energy Outlook [1])

Billion toe
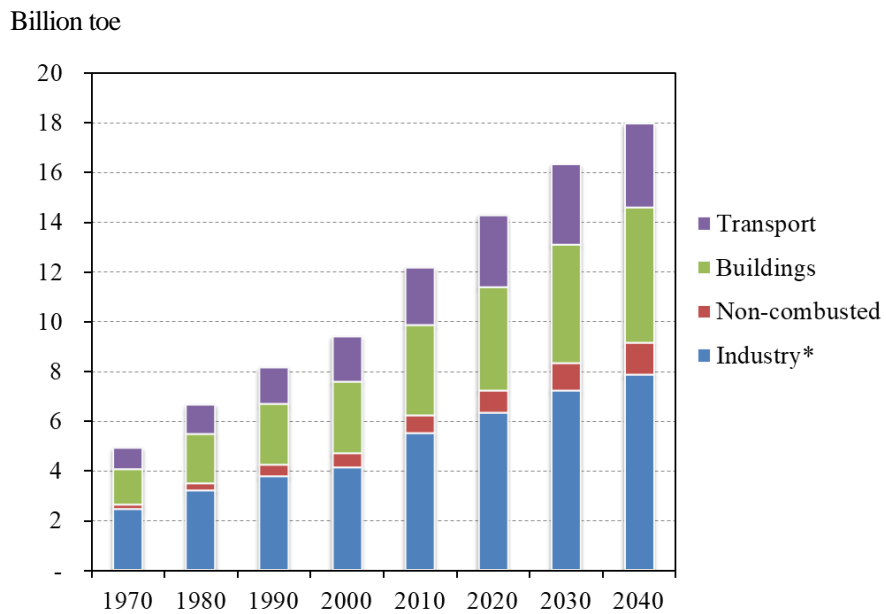
Figure 1-2. Primary energy consumption by sector (from BP Global, 2018 BP Energy

2

Outlook [1], *Industry excludes non-combusted use of fuels)

The end-use sector of primary energy demand is shown in Figure 1-2 (from BP Global, 2018 BP Energy Outlook [1]). The sectors of transport, industry, non-combusted, and buildings are predicted to show an increase ratio of 27.6%, 31.4%, 57.8%, and 42.3% in the coming decades (from 2662 Mtoe, 5965 Mtoe, 809 Mtoe, and 3840 Mtoe at 2016 to 3398 Mtoe, 7843 Mtoe, 1277 Mtoe, and 5466 Mtoe at 2040, respectively). The energy consumption by region from 1970 to 2040 is shown in Figure 1-3 (from BP Global, 2018 BP Energy Outlook [1]). It is evident from this figure that all of the growth in energy demand is from fast-growing developing economies, driven by increasing prosperity. In the next few decades, China, India and other emerging Asia will account for 2/3 of the growth in energy consumption, because of the growing energy consumption in countries with high rates of development in those regions.
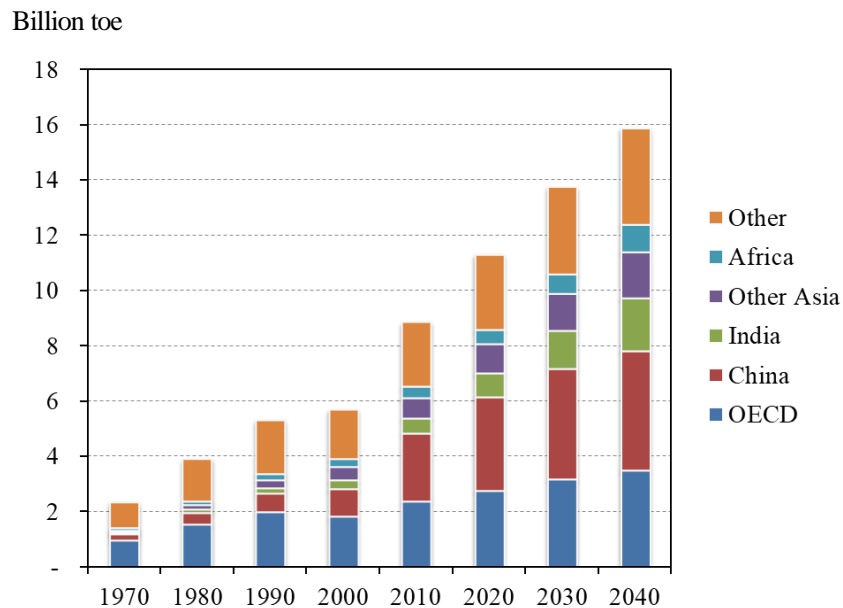
Figure 1-3. Primary energy consumption by region (from BP Global, 2018 BP Energy Outlook [1])

According to a survey by BP Global, published in the new Annual Energy Outlook of 2013 [1], based on the growth rates in 2013, the estimated global recoverable coal reserves will be exhausted within about 113 years if no new reserves are found; the estimated recoverable petroleum reserves can meet global demand for as long as 53.3 years; and the

estimated recoverable natural gas reserves are sufficient for 55.1 years of further supply. If new energy resources and technologies are not found, energy supply will become one of the biggest obstacles for economic and societal development.

Pollutants such as CO_2, CO, SO_2, NO_x, volatile organic compounds (VOCs), particulate matter (PM), lead, and various toxic species, including benzene, formaldehyde, acetaldehyde, and 1,3-butadiene, are released by the combustion of petroleum, coal, and natural gas fuels. CO_2 is the major contributor to global warming, SO_2 causes acid rain, NO_x and VOCs damage the ozone layer, while PM, lead, and toxic species adversely affect the human health, especially that of children and the elderly. Global warning and related climatic change from energy consumption has become one of the main threats to human society. Figure 1-4 shows global CO_2 emissions from the consumption of different fuels between 1990 and 2014; it is evident that total CO_2 emissions in 2014 (33.8×10^9 ton) were 1.58 times those in 1990 (21.4×10^9 ton). CO_2 emissions from liquid (mainly refer to petroleum), solid (mainly refer to coal), and gaseous fuel (mainly refer to natural gas) contribute to 35.6%, 44.6%, and 19.8% of fossil fuel emissions, respectively.
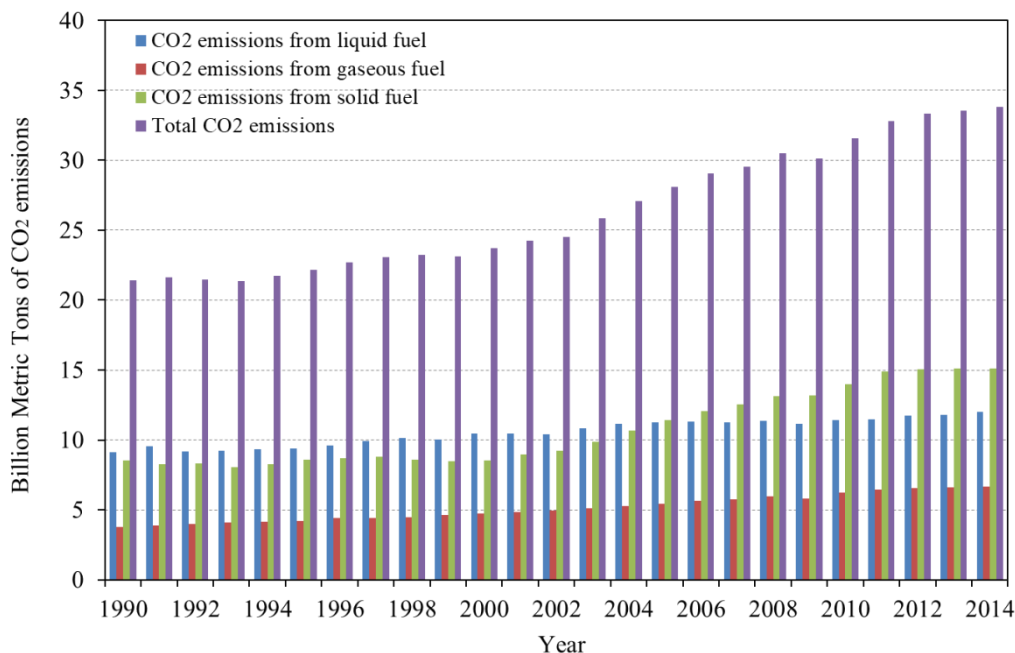
Figure 1-4. Global CO_2 emissions from 1990 to 2014 by fuel (from Carbon Dioxide Information Analysis Center [2])

According to statistical review world energy by BP [1], the ten countries with the highest CO_2 emissions in 2017 are the USA (15.2%), China (27.6%), India (7.0%), Russia (4.6%), Japan (3.5%), Germany (2.3%), South Korea (2.0%), Canada (1.7%), Iran (1.9%), and the Saudi Arabia (1.8%), and they account for two-thirds of global CO_2 emissions. The developing countries such as China and India will be confronted with considerable increases in CO_2 emissions associated with their high rate of economic growth.

As shown in Figure 1-5, refrigeration sector accounts for approximately 17% of the global electricity consumption. It demonstrates the significance of refrigeration sector that is expected to play a growing role in the situation of global warming and the increasing demand in various fields.
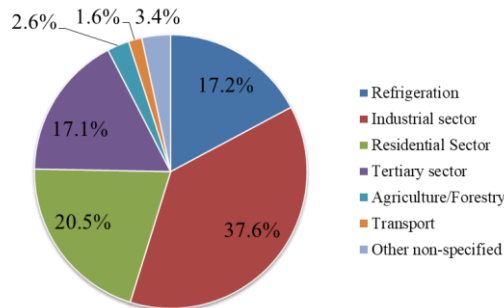
Figure 1-5. Comparison of the global refrigeration sector's electricity consumption with that of other sectors [3]

Data of global greenhouse gas emissions by gas in 2015 are indicated Figure 1-6 [4]. The figures are expressed in CO_2-equivalents and are rounded and hence do not add up to 100%. Overall, we can see that CO_2 accounts for about 81.2% of total greenhouse gas emissions. CH_4 (primarily from agriculture) and N_2O (mostly from industry and agriculture) contribute around 10% and 5.5% to the global greenhouse gas emissions, respectively. F-gases, as an abbreviation for fluorinated gases, are a family of HFCs, perfluorocarbons (PFCs), unspecified mix of PFCs and HFCs, sulphur hexafluoride (SF_6) and nitrogen trifluoride (NF_3). Although they only contribute 2.5% to global greenhouse gas emissions, occupy nearly 20% of refrigeration systems' global warming impact [3].
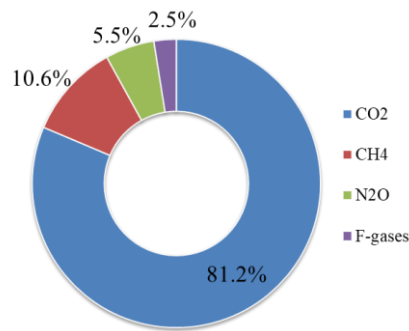
Figure 1-6. Global greenhouse gas emissions by gas in 2015 [4]

In the recent years, the development of new technologies aiming to reduce problems related to energy consumption, for application in both developed and developing countries, has become urgent, because of the increasing strictness of governmental regulation of energy and pollutant emissions. Such developments lead to the search for alternative fuels, and the increasing importance of renewable energy sources.

1.1.2 Transportation and food storage

In 2017, approximately 821 million (about one out of every nine) people in the world are estimated to affect by undernourishment. This situation is significantly worse in most countries of Africa, whose economies are highly dependent on the agriculture activity, with an increase number of undernourishments from 212.5 million in 2014 to a projected 256.5 million in 2017 [5]. IIR data [3] indicate that approximately 20% of world food supply are wasted (on average 9% and 23% for developed countries and developing countries, respectively) due to the poor cold train system include, such as shortage of appropriate transport systems and lack of efficient refrigeration facilities. Global population is expected to reach 9.1 billion by 2050, 2.3 billion more people than 2009, while at the same time an increase by about 70% in global food production will be needed in order to feed this enormous population growth [6]. Accordingly, establishing a reliable and quality food transportation system, especially in the developing countries, is necessary to maintain the quality of perishable commodities and reduce their loss.

There are three types of refrigerated transportation systems: road transport, marine

transport and air transport. According to the estimation from IIR [3], there are approximately 4 million refrigerated vehicles (vans at 40%, trucks at 30% and semi-trailers or trailers at 30%) and 1.2 million refrigerated containers in service around the world. Moreover, until 2030 the road freight transport growth rate is expected to 2.5% per annual globally. In comparison with the other two transport modes, air transport has the advantage of drastically shortening delivery period. Hence, commodities with extremely short shelf life such as strawberry or high value are often transported by air. However, Table 1-1 [7] indicates that the energy consumptions and CO_2 emissions of air transport are much higher compared to other transport modes, especially by railroad and water, despite various factors (such as the size or type of the vehicles, trade routes, power source and weather conditions) would influence the accuracy of the figures.

Table 1-1. Energy and carbon intensity of different freight transport modes

	MJ per ton-km	g CO_2e per ton-km
International water container	0.2	14
International water Tanker	0.1	7
Inland water	0.3	21
Rail	0.3	18
Truck	2.7	180
Air	10	680

In 2012, air transport ($ 127 / kg) could be over110 times more expensive than ship transport ($ 1.10 / kg) on the basis of weight [8]. For most customers, the freight costs are the decisive factor influencing the selection of transport mode.

About 90% (by volume) of global trades are delivered by the international shipping [9], and it accounts for about 31% [10] of the global fresh food transport, are a vital component of the transportation system, aim at maintaining and supplying safe and high quality food.

Figure 1-7 illustrates the average percent share of emissions by ship class from 2013 to 2015. A largest proportion (about 23%) CO_2 emissions can be ascribed to container ships, followed by 19% and 13% for bulk carriers and oil tankers, respectively. These three classes of ship together constituted 55% of the approximately 1 billion tons of CO_2 emissions in the period 2013 to 2015. Moreover, compared to other ship classes, they made up 84% of the total traded goods, which accounts for their 55% total CO_2 emissions.
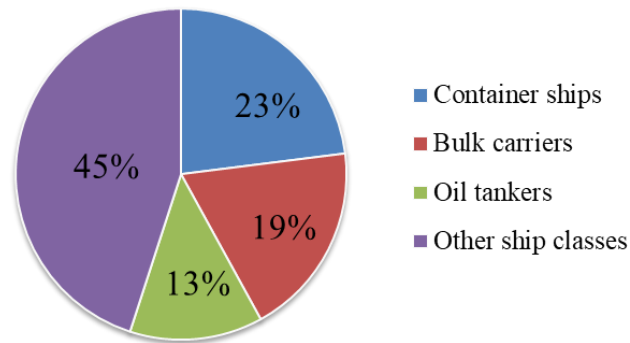
Figure 1-7. Average percent CO_2 emissions shared among ship class, 2013-2015 [11].

In light of the IMO's (Third International Maritime Organization) report in 2014 [12], international shipping greenhouse gas emissions in 2012 contributed to about 2.2% and 2.1% of the world CO_2 and CO_2 equivalent basis emissions, respectively. While these figures may appear as a considerably small proportion of global GHG emissions, if there is no further effective mitigation action, relevant emissions are predicted to increase by 50% ~ 250% by 2050 and could contribute to 17 % of the anthropogenic CO_2 emissions in 2050 [13].

Diesel engines have been extensively applied in marine ships as their prime movers or auxiliary systems. According to their operating cycle, diesel engines can be classified into two-stroke engine and four-stroke engine. The two-stroke diesel engine, due to its simplicity, cost less to manufacture, low friction and can run on cheaper heavy fuel oil compared to other types, is the most commonly used marine propulsion. To improve the fuel energy efficiency is the prime objective for marine transport, despite marine diesel engines can achieve a relatively high efficiency of around 50%.

As illustrated in Figure 1-8 [14], jacket water, exhaust gas and air cooler are the three principal waste heat sources from engine, accounts for about 5.2%, 25.5% and 16.5% of the total engine fuel energy, respectively. The temperature ranges of these three kinds of waste heat from a two-stroke diesel engine are about 70~120 ℃, 205~500 ℃ and 130~150 ℃ for jacket water, exhaust gas and air cooler, respectively [15]. It's self-evident that the

importance of improving the food transportation system's energy efficiency.
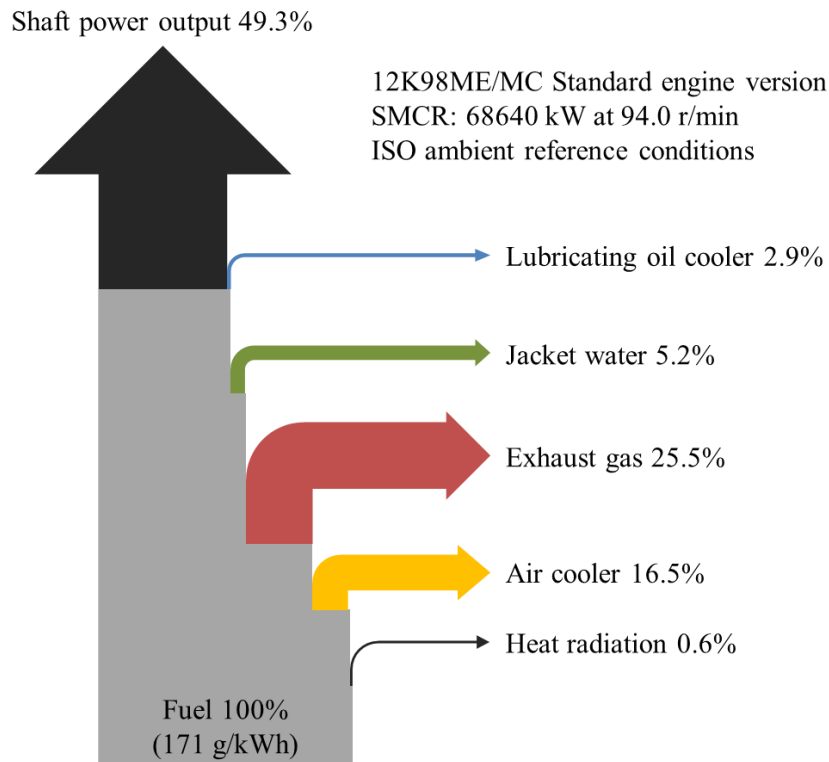
Figure 1-8. Heat balance diagram of nominally rated 12K98ME/MC engine of the standard engine version operating at ISO ambient reference conditions and at 100% SMCR (specified maximum continuous rating). ISO ambient reference conditions: barometric pressure: 1,000 mbar; turbocharger air intake temperature: 25 ℃; charge air coolant temperature: 25 ℃; relative air humidity: 30%.

Further endeavors are necessary to develop and optimize low environmental impact systems such as HFCs-free refrigerant. The HFCs have significant contributions to the climate change not only through direct influence that quantities of refrigerants emitted into environment (such as leakage), but also by indirect influence from the energy consumed to operate the refrigeration system. Taking into consideration the regulations on hydrofluorocarbons (HFCs) and the requirements of phase-out of high greenhouse gas potential refrigerants, it is imperative to investigate and develop alternative refrigerants and innovative systems that have low environmental impacts and high energetic performance.

1.2 Motivation

1.2.1 Storage conditions and quality evaluation of fruits and vegetables

In view of the fasting growing market for food storage and transportation, especially in developing countries, it is unavoidable to increase greenhouse gas emissions considerably in the future if no relevant action is taken. In order to reduce unnecessary energy consumption and CO_2 emissions in food transportation system, it requires not only proper regulation of storage conditions and efficient energy utilization, but also needs accurate and convenient food quality evaluation method.

Vegetables and Fruits, such as spinach (Spinacia oleracea L.), komatsuna (Brassica rapa var. perviridis) and strawberry (Fragaria × ananassa Duch.), provide essential micronutrients and vitamins to the human diet. Spinach is cultivated globally, and is an exceptional source of vitamins, notably high in vitamin K (270 μg/100g), vitamin B2 (200 μg/100g) and folate (210 μg/100g), as well as being a rich source of microelements, like potassium (690 mg/100g), iron (2.0 mg/100g) and magnesium (69 mg/100g) [16]. These phytonutrients are conducive to various physiological functions, like prevention of hemophilia, hypertension, and bone fracture [17]. Komatsuna is a traditional green leafy vegetable in Japan, which is sometimes called Japanese mustard spinach. As the term suggests, komatsuna also contains many phytonutrients that have disease prevention and health promotion effects as spinach, like vitamin K (210 μg/100g), potassium (500 mg/100g). Moreover komatsuna is an outstanding source of calcium (170 mg/100g) and iron (2.8 mg/100g), which can help prevent osteoporosis and anemia respectively [16]. Strawberry (Fragaria × ananassa Duch.) is a popular and attractive fruit due to its adorable appearance, delicious flavor and taste, potential sources of ascorbic acid (62 mg/100g), potassium (170 mg/100g) and calcium (17 mg/100g) [17]. In addition, strawberry also contains high contents of phenolic constituents such as phenolic acid, anthocyanins and flavones [18, 19], which have been demonstrated to be effective in neutralizing harmful free radicals and preventing thrombosis, tumorogenesis [20], lowering the risk of cardiovascular, cancer and arthritis disease [21]. Due to the characteristics mentioned above and the delicious flavor, they occupy an important position in the Japan's fruit markets. However,

the highly perishable nature of these products results in a very short postharvest life that is a big challenge for the production, transportation and marketing chain. Therefore, the management and inspection of fresh commodities quality are of critical importance throughout the whole chain.

Accurate food quality classification is critical for grading to meet the needs of customers and setting prices. Visual quality rating, a conventional method of evaluating the quality of vegetables and fruits, is widely used in the agricultural and food sector owing to its ease of implementation. Nevertheless, this method is subjective and the results would vary considerably among inspectors or even if by the same inspector over time [22]. There are four main characteristics that typically affect the purchasing decisions of consumers to a vegetable or fruit, and the color and appearance were thought to be the most important characteristics [23]. Prior to the purchase, consumers actually often evaluate fresh produces based mainly upon their color and appearance, for instance, discoloration of the leaves, browning at the petioles or objectionable softening in strawberries are causes that result in consumers refuse to purchase the produces.

The colors of vegetables and fruits are an indicator of their natural pigments and health. There are two main categories of color pigments in the leaves of plant: chlorophylls (appear green) and carotenoids (responsible for yellow, orange and red). The color of fresh green leafy vegetables, such as spinach or komatsuna, only show the green color due to the bright colors of carotenoids are concealed by chlorophylls [24]. In addition to being responsible for leaf greenness, chlorophyll plays an important role in the process of photosynthesis and can be an estimator of plant physiological or nutrient status. The conventional approaches to investigate chlorophyll, such as leaf solvent extraction and spectrophotometric analysis [25] [26] or high-performance liquid chromatography (HPLC) [27, 28], are widely used due to their high accuracy, but nonetheless they are destructive, time-consuming, labor intensive, and incapable of evaluating a large quantity of samples. In addition, these approaches require destruction of evaluated samples, and can therefore not evaluate the changes in chlorophylls over time for a single sample. Hyperspectral imaging, which was originally developed for remote sensing [29], has been applied in the fields of food safety and quality

control, such as contaminant detection [30], quality inspection [31-33], fungal infection [34, 35], and disease analysis [36, 37]. Hyperspectral imaging technique integrates imaging and spectroscopic techniques to capture both spatial and spectral information from sample radiative behavior. From the information, the internal characteristics and the distribution or change of pigment contents of sample can be derived.

Sun et al. [38] determined chlorophyll content in honey peaches by using hyperspectral imaging for distinguishing diseased peaches. Three chlorophyll content related optimal wavelengths were extracted from hyperspectral images through successive projections algorithm. It demonstrated that three band ratios, which were achieved by adopting the three optimal wavelengths, were applicable to discriminate the diseased peaches with 98.75% accuracy and the spatial distribution of decayed parts can be shown clearly. Schmilovitch et al. [39] used hyperspectral imaging technique to detect and map quality attributes (total soluble solids, ascorbic content, total chlorophyll and carotenoid) in three cultivars of bell pepper. Partial least squares regression model was applied to predicted the four quality attributes and achieved high coefficients of determination, low root mean squared errors of calibration and cross-validation. The results of this research indicated that hyperspectral imaging technology has the possibility of detecting the changes in pepper qualities during fruit maturation and being able to apply in online sorting systems for quality determination of peppers. Feng et al. [40] used hyperspectral imaging method to design an integrated image analysis pipeline that was capable of processing tremendous number of hyperspectral data automatically. They accurately quantified four kinds of pigments (chlorophyll a, chlorophyll b, total chlorophyll and carotenoid) in rice leaves by a liner model and indicated that the highest correlation region with these pigments was detected in the wavelength range of 700~760 nm. They also digitized the distribution of chlorophyll with high resolution of 0.11 mm/pixel by associating the hyperspectral data with the models developed. This research offers the potential to quantify the chlorophyll content in other crops. Bergsträsser et al. [41] assessed Cercospora beticola disease and leaf chlorophyll content of four different crops (barley, maize, rapeseed and tomato) by using an innovative imaging technique, which was named hyperspectral absorption-reflectance-transmittance imaging (HyperART) system. The HyperART system

can acquire the spatial and spectral information of reflected and transmitted light from the whole leaf simultaneously in the range of 400 ~ 2500nm, and therefore, allowing the computation of absorption spectra with one sensor. It demonstrated that the values measured by HyperART system were comparable to those measured by a well-established commercial spectroradiometer. It also indicted that as compared to identification by visual inspection, the HyperART system produced a more accurate and reliable result in the quantification of Cercospora beticola symptoms. Moreover, it shown that this system was able to precisely estimate and monitor the variations of chlorophyll content in four different species, and the estimation performance can be improved significantly by using the data of non-absorbed radiation which was the sum of reflectance and transmittance. The hyperspectral imaging technique has also been successfully employed in evaluating strawberry quality attributes, such as ripeness [42], moisture content, acidity and total soluble solids [43], firmness [44], bruise identification [45], fungal detection [46, 47].

In the light of aforementioned findings, hyperspectral imaging, which is considered as a powerful and nondestructive method, can be potentially applied to detect the visual quality change of fresh commodities in the whole production chain. Heretofore, there have been few studies contributed to the development of hyperspectral imaging system for the visual quality evaluation in fresh commodities. And to the best of our knowledge, no research has yet been conducted to investigate the relationship between the strawberry calyx and fruit quality by the application of hyperspectral imaging technique.

Properly operated food storage system will prolong the shelf life of produces by providing suitable storage condition that can effectively lower their microbiological change, retard ripening and slow physical processes. Temperature and relative humidity are two of the most crucial determinants for maintaining food quality and extending their shelf life. A stable temperature environment is indispensable during food transportation, as higher temperature will accelerate the respiration and transpiration rates, and thereby lead to a decrease in weight, wilting or spoilage; however, excessively low temperature will result in chilling injury. Therefore, it is necessary to investigate the storage limitations of perishable commodities under a range of storage conditions. Moreover, food quality monitoring during

transportation is also important for effective and safe transport during the storage period. On the other hand, recovering the large amount of energy contained in the waste heat is an attractive way to create a sustainable economic and environmentally friendly development in transportation system. Due to the capability of maintaining at a certain sailing speed for a long period, maritime transportation is easier to utilize more continuous and stable waste heat from the engine when compared with road transportation. The contribution of food transport refrigeration to the energy aspect of efficiency improvement could be demonstrated through the vital role of thermally driven refrigeration technologies for maintaining high food quality by optimization of storage conditions. The development of a high-quality food storage system with low carbon transportation is necessary. Adsorption technology appears to be an efficient and promising option for use in food refrigeration system, mitigating CO_2 emissions and reducing system fuel consumption.

1.2.2 Adsorption refrigeration systems for food transport

Adsorption refrigeration systems, as one of the promising effective energy conservation techniques and environmentally friendly applications, have been widely studied since the 1970s due to the oil crisis [48]. In comparison to vapor compression refrigeration systems, adsorption refrigeration systems can be driven by low-grade thermal energy sources, such as solar energy, geothermal energy, waste heat from industries/automobiles/fuel cells/combined heat and power systems (CHP) etc., instead of electricity consumed by a compressor, and therefore have large energy conservation potential. Moreover, adsorption refrigeration systems mainly use natural working refrigerants, like water, ammonia and methanol, have the advantage of zero global warming potential and zero ozone depletion potential [49]. Such systems can be applied in a variety of applications, such as air conditioning in buildings or automobiles, process cooling, ice making, food storage, medicine protection, thermal lift and so on.

Figure 1-9 illustrates the schematic layout of a continuous operating single stage two-bed adsorption refrigeration system, which is a closed system mainly consisting of an evaporator, a condenser, and two adsorbers/desorbers containing the adsorption cores. When one adsorber/desorber is in the adsorption and preheating process, the other one is in

14

desorption and precooling process. The condensed liquid refrigerant flows back to the evaporator through an expansion valve that is used to control the pressure difference between the evaporator and condenser.
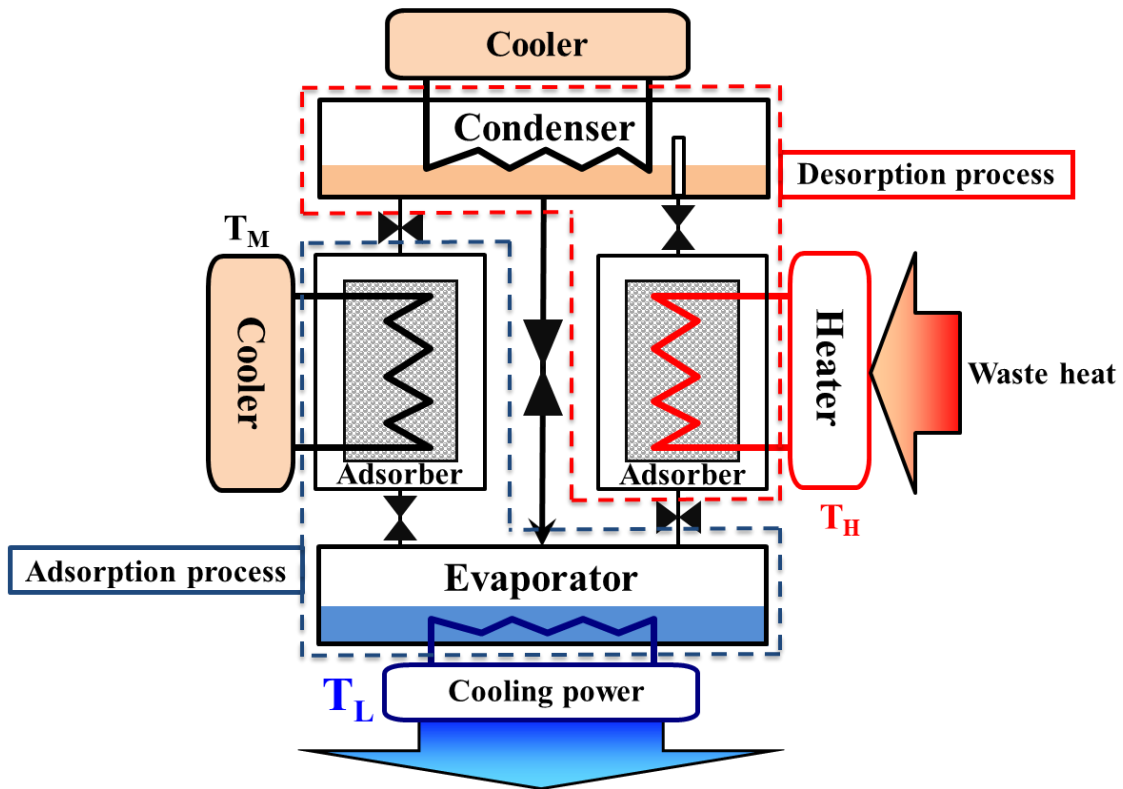
Figure 1-9. Schematic layout of a single stage two-bed adsorption refrigeration system.

A single stage two-bed adsorption refrigeration system is driven by three different temperatures, which are desorption temperature (T_H), adsorption temperature or condensing temperature (T_M), and evaporating temperature (T_L). The desorption temperature is the temperature of heat source (such as waste heat from engines, residences, industries, fuel cells or solar systems). The saturated refrigerant vapor pressure of each heat source temperature (T_L, T_M, and T_H) is P_L, P_M and P_H, respectively. The relative pressures are calculated by the following equations:

$$\phi_{ads} = \frac{P_L}{P_M}$$

(1-1)

$$\phi_{des} = \frac{P_M}{P_H}$$

$$(1\text{-}2)$$

The relative pressure of adsorption process ϕ_{ads} increases with the increase of T_L or the decrease of T_M, while with the increase of T_M or the decrease of T_H, ϕ_{des} increases. Figure 1-10 shows the NH_3 adsorption isotherm of AB14-02 activated carbon at 278 K, the amount adsorbed in adsorption process q_{ads} at the relative pressure of ϕ_{ads} and the amount adsorbed in desorption process q_{des} at the relative pressure of ϕ_{des} can be obtained from the adsorption isotherm and desorption isotherm, respectively.
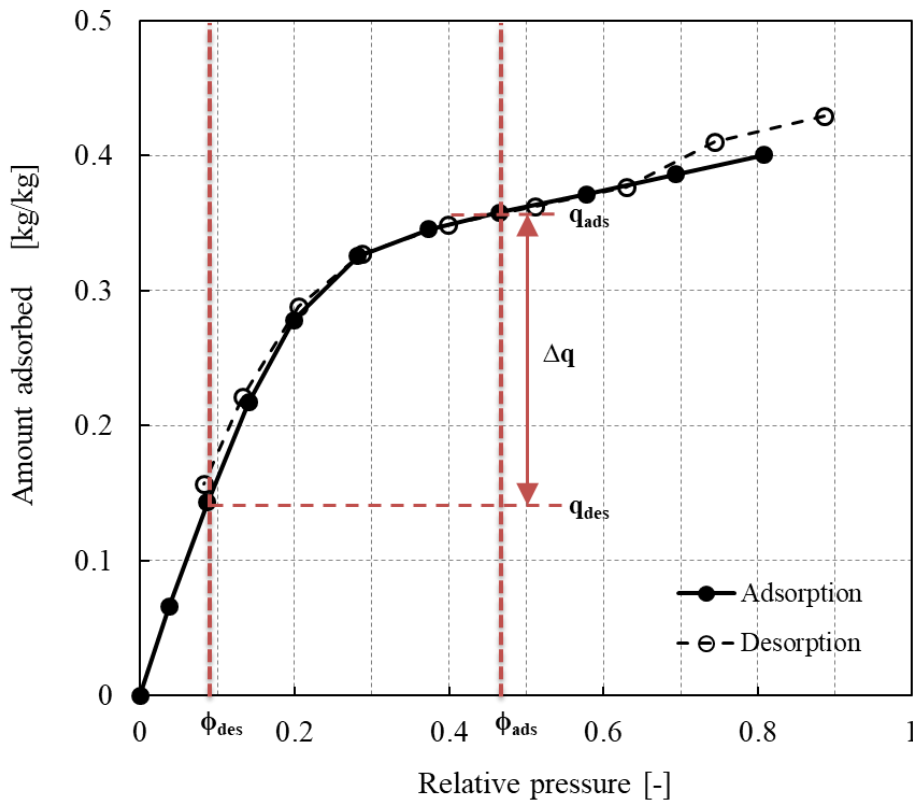
Figure 1-10. Adsorption isotherm of NH_3 on activated carbon (AB14-02) at 278 K.

Therefore, the cooling effect of the system can be calculated as follows:

$$Q_C = \Delta H_{eva} m \Delta q$$

$$(1\text{-}3)$$

where Δq ($= q_{ads}\text{-}q_{des}$) is the difference of adsorption capacity between adsorption process and desorption process, ΔH_{eva} is the heat of evaporation (kJ/kg$_{\text{-refrigerant}}$). Due to the adsorption isotherm is dependent on the characteristics of adsorbent and adsorbate, the

16

combination or selection of adsorbent/adsorbate pair is a critical factor for achieving a high cooling effect.

The basic adsorption refrigeration cycle consists of four thermodynamic processes which are preheating (①), desorption (②), precooling (③) and adsorption (④) as illustrates in Figure 1-11 and Figure 1-12. The refrigerant is initially adsorbed by the adsorbent which is packed inside the adsorption core at a temperature of T_1 and a pressure of P_L, and the amount of adsorbed refrigerant is q_{ads}.

Preheating process (①): This process is also named as isosteric heating. The valve between the adsorber/desorber and the condenser is closed. The adsorber/desorber is heated by the waste heat, with a corresponding increase in its temperature from T_1 to T_2 and pressure from P_L to P_M along the isosteric line ab. The mass of refrigerant in the adsorber/desorber stays constant at q_{ads}. The amount of heat required in this process is calculated as follows:

$$Q_{ab} = \int_{T_1}^{T_2} \left(m q_{ads} Cp_{ref} + m Cp_{ad} + m_{hex} Cp_{hex} \right) dT$$

(1-3)

where m is the mass of adsorbent (kg), m_{hex} is the mass of heat exchanger (kg), q_{ads} is the maximum amount adsorbed at adsorption process (kg-refrigerant/kg-adsorbent), Cp_{ref} is the specific heat of liquid refrigerant at constant pressure (kJ/kg/K), Cp_{ad} is the specific heat of adsorbent at constant pressure (kJ/kg/K), and Cp_{hex} is the specific heat of heat exchanger at constant pressure (kJ/kg/K).

Desorption process (②): After the preheating process, the valve between the adsorber/desorber and condenser is opened. Desorption process occurs, while the heating process continues uninterrupted. During the desorption process, the adsorber/desorber temperature increases from T_2 to T_H while the pressure remains constant (following the isobaric line bc), hence known as isobaric heating. The desorbed refrigerant vapor flows into the condenser and is condensed by releasing the condensation heat to the coolant. When the adsorption core reaches the highest temperature T_H, this process stops and the amount of adsorbed refrigerant declines to minimum value q_{des}. The amount of heat needed

17

for desorption process can be evaluated applying the following equation:

$$Q_{bc} = \int_{T_2}^{T_H} \left(mq_{ads}Cp_{ref} + mCp_{ad} + m_{hex}Cp_{hex} \right) dT + m\Delta H_{des}\left(q_{ads} - q_{des} \right)$$
(1-4)

where q_{des} is the minimum amount adsorbed at desorption process (kg-refrigerant/kg-adsorbent), ΔH_{des} is the heat of desorption (kJ/kg-refrigerant).

Precooling process (③): Similar to the preheating process, this process is also called isosteric cooling process. The valve between the adsorber/desorber and condenser is closed. The cooling water, which has a temperature of T_M, flows into the adsorber/desorber, and then extracts the sensible heat from the adsorber/desorber. During this process, the temperature and pressure of the adsorber/desorber decrease from T_H and P_C to T_3 and P_L along the isosteric line cd, respectively. The quantity of refrigerant in the adsorber/desorber is maintained at a constant value of q_{des}. The following equation is used to determine the amount of heat needs to be extracted from the adsorber/desorber during the precooling process:

$$Q_{cd} = \int_{T_H}^{T_3} \left(mq_{des}Cp_{ref} + mCp_{ad} + m_{hex}Cp_{hex} \right) dT$$
(1-5)

Adsorption process (④): The whole adsorption refrigeration cycle is ended by adsorption process, which is also named isobaric cooling. The valve between the adsorber/desorber and evaporator is opened. The refrigerant in the evaporator is vaporized by absorbing the heat from chilled water (with an initial temperature of T_L), and thus the cooling effect is generated. The refrigerant vapor flows into the adsorber/desorber and is adsorbed by the adsorbent. During this process, the adsorption heat is extracted from the adsorbent by the cooling water, and the temperature of adsorbent reduces from T_3 to T_1 along the isobaric line da. The adsorbent reaches its maximum refrigerant adsorbed amount of q_{ads} at T_1. The amount of heat rejected to the environment for this process is expressed by equation (3-4):

$$Q_{da} = \int_{T_3}^{T_1} \left(mq_{ads}Cp_{ref} + mCp_{ad} + m_{hex}Cp_{hex} \right) dT + m\Delta H_{ads} \left(q_{ads} - q_{des} \right)$$

where ΔH_{ads} is the heat of adsorption (kJ/kg-refrigerant).

① **Preheating process**

② **Desorption process**

③ **Precooling process**
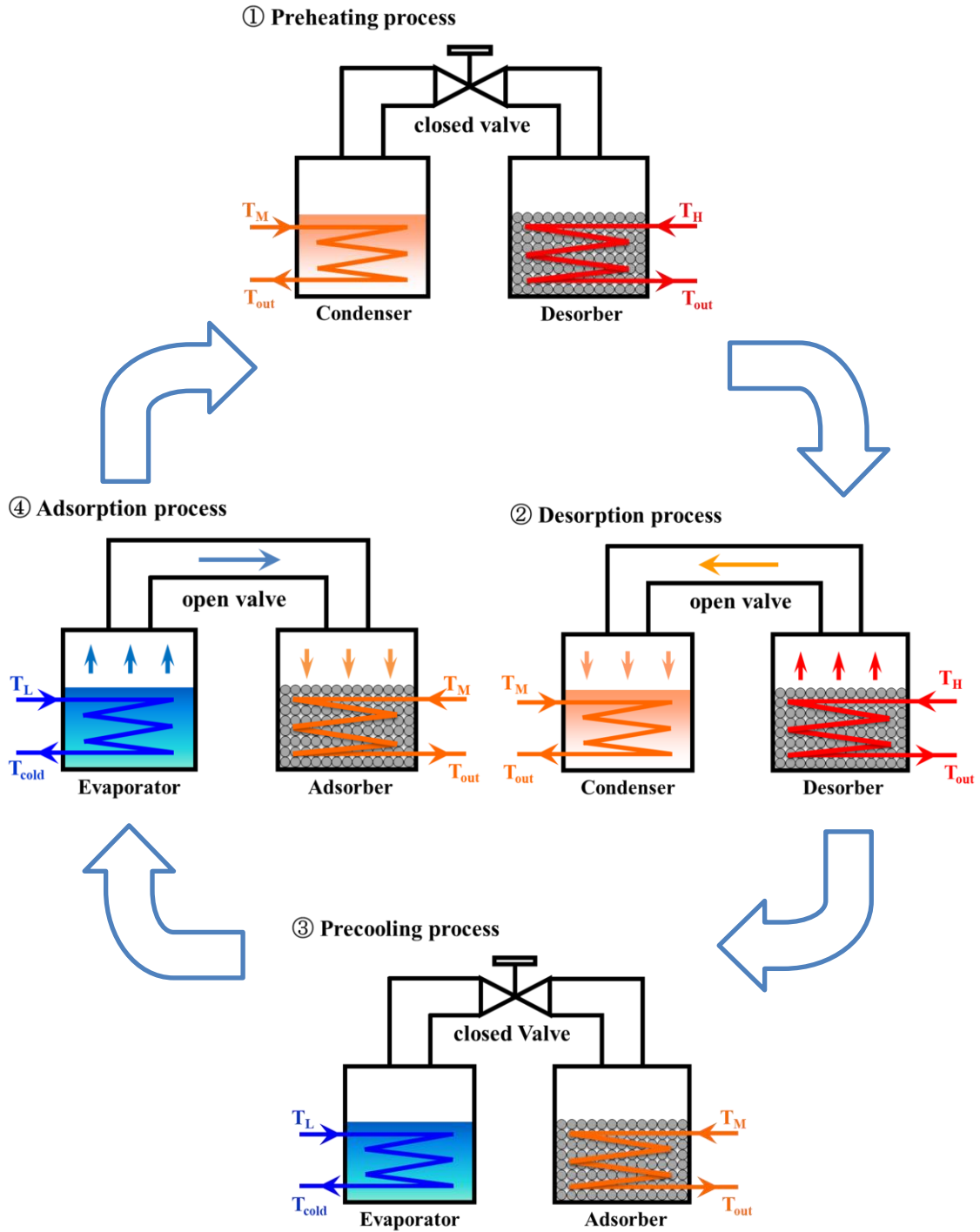
④ **Adsorption process**

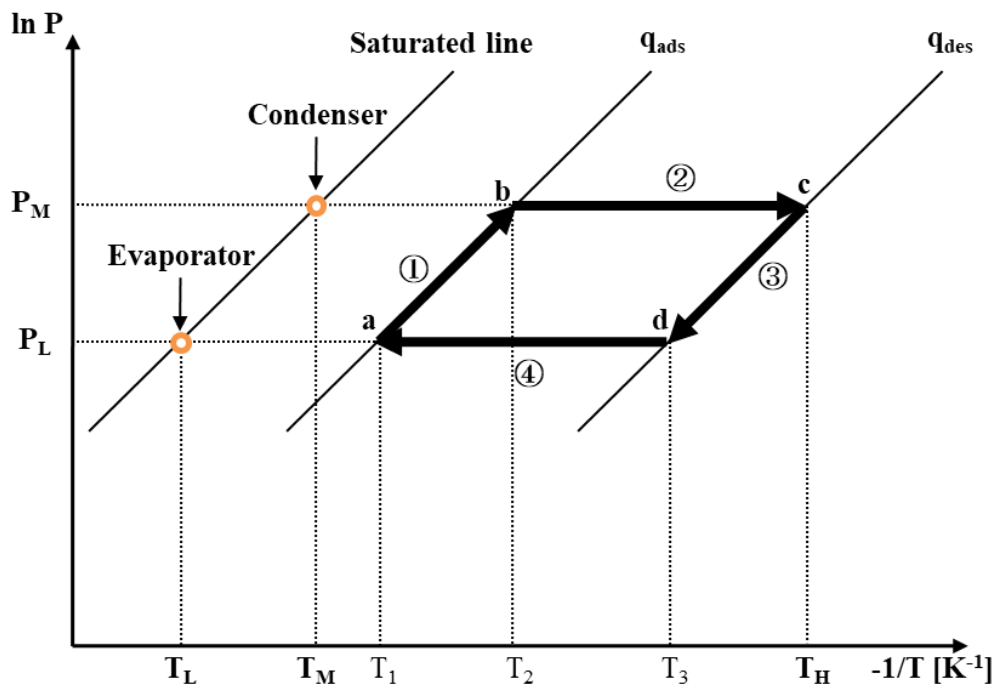Figure 1-11. Principle of adsorption refrigeration system.

Figure 1-12. Thermodynamic cycle of a basic adsorption refrigeration system.

Adsorption refrigeration systems have great potential to tackle the barriers of the places where the electricity supply is difficult (such as the rural areas of developing countries) by using solar energy or the refrigerated transport via the utilization of the waste heat of the engine.

Combining a thermally driven refrigeration system with a CHP system, which is defined as combined cooling, heating, and power (CCHP) system, can produce not only power and heating but also cooling simultaneously, with an overall efficiency may reach up to 90% compared to about 35% for the conventional coal-fired power station. Thus CCHP system, exhibits outstanding energy efficiency, economic feasibility and ecological advantage, is a promising integration for application in various sectors.

Absorption refrigeration systems are the most successful practical applications of CCHP and studies have been concentrated in lithium bromide-water [50-52] and water-ammonia [53, 54] absorption refrigeration systems. However, despite the above mentioned advantages and some new small-capacity products are market available in recent years (such as 2.5kW ENC, 10kW STJU, 10kW Mitsubishi Plastics, 13kW SorTecheZea

10IPS, 4-14kW Invensor LTC 10e, etc.), there are only a few real application of adsorption refrigeration systems installed in CCHP systems compared with absorption refrigeration systems [55-57].

The major challenges that we face are: (1) low coefficient of performance (COP) and (2) low specific cooling power (SCP) or volumetric cooling power (VCP) that make them large volume and weight, due to the low thermal conductivity and low adsorption capacity of adsorbents, and the poor heat and mass transfer performance of the adsorbent beds.

1.3 Objectives

The focus of this research is summarized in the following key objectives:

1) To better develop and optimize an objective, fast and efficient hyperspectral imaging system, the evaluation of agricultural products at various storage temperatures, relative humidity and storage periods are investigated, the laboratory-based hyperspectral imaging system for investigation of the chlorophyll distribution in three species of agricultural products for evaluating visual quality was established. The effects of storage temperature, humidity, and storage periods on the visual quality rating, water content, and total soluble solid of agricultural products have been investigated.

2) To effectively utilize the exhaust heat from the food storage system, an activated carbon-NH_3 adsorption refrigeration system with high ability and long durability is proposed. The performance of NH_3 refrigeration system at various evaporating temperatures and cycle times were experimentally investigated.

3) To effectively utilize the exhaust heat from the food storage system, a thermal and electrical hybrid adsorption chiller cycles with and without mechanical booster pump (MBP) was analyzed, the effect of MBP on the adsorption and desorption process was investigated.

1.4 Outline

This thesis includes four chapters. The literature review and background information on the high-quality food storage system are summarized in Chapter 1, as aforementioned.

Chapter 2 reports the experimental investigation of an objective, fast and efficient hyperspectral imaging system for agricultural products storage. The effects of storage temperature, humidity, and storage periods on the visual quality rating, water content, and total soluble solid of agricultural products have been investigated. A quality evaluation method for agricultural products storage with hyperspectral imaging technology was developed.

In Chapter 3, an activated carbon-NH_3 adsorption refrigeration system with high ability and long durability is proposed to effectively utilize the exhaust heat from the food storage system. The specific surface area, pore size distribution and morphological structure of the activated carbons have been characterized by N_2 adsorption, SEM, and XRD. The adsorption capacities of four kinds of activated carbons were compared based on adsorption isotherms at 30 °C. The performance of NH_3 refrigeration system at various evaporating temperatures and cycle times were experimentally investigated.

In Chapter 4, a lab-scale FAM-Z05/H_2O type adsorption chiller cycle with and without mechanical booster pump (MBP) was analyzed, the effect of MBP on the adsorption and desorption process was summarized.

Chapter 5 summaries the conclusions of this study and suggestions in the future work about the high-quality food system for low carbon transportation system.

1.5 Reference

［1］　　BP energy in worldwide energy use to 2040, BP Global, 2018.

［2］　　Carbon Dioxide Information Analysis Center, Environmental Sciences Division, Oak Ridge National Laboratory, Tennessee, United States.

［3］　　The role of refrigeration in the global economy.
http://www.iifiir.org/userfiles/file/publications/notes/NoteTech_29_EN.pdf

［4］　　Information on Data Sources.
https://unfccc.int/process/transparency-and-reporting/greenhouse-gas-data/greenhouse-gas-data-unfccc/information-on-data-sources

［5］   The state of food security and nutrition in the world.

https://reliefweb.int/sites/reliefweb.int/files/resources/English___The_State_of_Food_Secur ity_and_Nutrition_in_the_World_2018_-_Full_Report.pdf.

［6］   FAO, High Level Expert Forum - How to Feed the World in 2050

［7］   Weber, C. L., & Matthews, H. S. (2008). Food-miles and the relative climate impacts of food choices in the United States.

［8］   Shacklett, Mary. Air Cargo Redefines Its Business Outlook. World Trade: WT100; Dec 2014, p12.

［9］   International Maritime Organization, https://business.un.org/en/entities/13

［10］   Getahun, S. T. (2017). Investigating cooling performance and energy utilization of refrigerated shipping container packed with fresh Fruit using computational fluid dynamics modeling (Doctoral dissertation, Stellenbosch: Stellenbosch University).

［11］   Olmer, N. A. Y. A., Comer, B. R. Y. A. N., Roy, B. I. S. W. A. J. O. Y., Mao, X., & Rutherford, D. (2017). Greenhouse gas emissions from global Shipping, 2013–2015. The International Council on Clean Transportation.

［12］   Third IMO GHG Study 2014 Executive Summary and Final Report. Published in 2015 by the international maritime organization 4 Albert Embankment, London SE1 7SR.

［13］   United Nations publication. Review of Maritime Transport 2017.

https://unctad.org/en/PublicationsLibrary/rmt2017_en.pdf

［14］   MAN B&W Diesel A/S, Copenhagen, Denmark. Thermo efficiency system (TES) for reduction of fuel consumption and CO_2 emission.

http://www.123energy.net/resources/cogeneration.pdf.

［15］   Shu, G., Liang, Y., Wei, H., Tian, H., Zhao, J., & Liu, L. (2013). A review of waste heat recovery on two-stroke IC engine aboard ships. Renewable and Sustainable

Energy Reviews, 19, 385-401.

［16］　Office for Resources, Policy Division Science and Technology Policy Bureau. (2015) Standards Tables of Food Composition in Japan (Seventh Revised Edition). http://www.mext.go.jp/en/policy/science_technology/policy/title01/detail01/sdetail01/sdetail01/1385122.htm

［17］　農畜産業振興機構. (2012) 野菜ブック: 食育のために. Available online: https://www.alic.go.jp/content/000138364.pdf

［18］　Moradi, S. (2015) Study of Correlation and Regression Analysis in Strawberry. International Journal of Farming and Allied Sciences, 4(8): 621-624.

［19］　Yuan, W., Zhou, L., Deng, G., Wang, P., Creech, D., and Li, S. (2011). Anthocyanins, phenolics, and antioxidant capacity of Vaccinium L. in Texas, USA. Pharmaceutical Crops, 2, 11-23.

［20］　Kris-Etherton, P. M., Hecker, K. D., Bonanome, A., Coval, S. M., Binkoski, A. E., Hilpert, K. F., Griel, A. E., and Etherton, T. D. (2002) Bioactive compounds in foods: their role in the prevention of cardiovascular disease and cancer. The American journal of medicine, 113(9), 71-88.

［21］　Basu, A., Rhone, M., and Lyons, T. J. (2010) Berries: emerging impact on cardiovascular health. Nutrition reviews, 68(3), 168-177.

［22］　Bremer, D. J., Lee, H., Su, K., & Keeley, S. J. (2011). Relationships between normalized difference vegetation index and visual quality in cool-season turfgrass: I. Variation among species and cultivars. Crop science, 51(5), 2212-2218.

［23］　Barrett, D. M., Beaulieu, J. C., & Shewfelt, R. (2010). Color, flavor, texture, and nutritional quality of fresh-cut fruits and vegetables: desirable levels, instrumental and sensory measurement, and the effects of processing. Critical reviews in food science and nutrition, 50(5), 369-389.

［24］　Kidmose, U., Edelenbos, M., Christensen, L. P., & Hegelund, E. (2005). Chromatographic determination of changes in pigments in spinach (Spinacia oleracea L.) during processing. Journal of chromatographic science, 43(9), 466-472.

［25］　Porra, R. J., Thompson, W. A., & Kriedemann, P. E. (1989). Determination of accurate extinction coefficients and simultaneous equations for assaying chlorophylls a and b extracted with four different solvents: verification of the concentration of chlorophyll standards by atomic absorption spectroscopy. Biochimica et Biophysica Acta (BBA)-Bioenergetics, 975(3), 384-394.

［26］　Marr, I. L., Suryana, N., Lukulay, P., & Marr, M. I. (1995). Determination of chlorophyll a and b by simultaneous multi-component spectrophotometry. Fresenius' journal of analytical chemistry, 352(5), 456-460.

［27］　Shioi, Y., Fukae, R., & Sasa, T. (1983). Chlorophyll analysis by high-performance liquid chromatography. Biochimica et Biophysica Acta (BBA)-Bioenergetics, 722(1), 72-79.

［28］　Garrido, J. L., & Zapata, M. (2006). Chlorophyll analysis by new high performance liquid chromatography methods. In: Chlorophylls and Bacteriochlorophylls (pp. 109-121). Springer, Dordrecht.

［29］　Gowen, A. A., O'Donnell, C., Cullen, P. J., Downey, G., & Frias, J. M. (2007). Hyperspectral imaging–an emerging process analytical tool for food quality and safety control. Trends in Food Science & Technology, 18(12), 590-598.

［30］　EVERARD, Colm D.; KIM, Moon S.; LEE, Hoyoung. A comparison of hyperspectral reflectance and fluorescence imaging techniques for detection of contaminants on spinach leaves. Journal of Food Engineering, 2014, 143: 139-145.

［31］　NANYAM, Yasasvy, et al. A decision-fusion strategy for fruit quality inspection using hyperspectral imaging. Biosystems engineering, 2012, 111.1: 118-125.

［32］   LI, Bo, et al. Application of hyperspectral imaging for nondestructive measurement of plum quality attributes. Postharvest Biology and Technology, 2018, 141: 8-15.

［33］   Diezma, B., Lleó, L., Roger, J. M., Herrero-Langreo, A., Lunadei, L., & Ruiz-Altisent, M. (2013). Examination of the quality of spinach leaves using hyperspectral imaging. Postharvest biology and technology, 85, 8-17.

［34］   SIEDLISKA, Anna, et al. Detection of fungal infections in strawberry fruit by VNIR/SWIR hyperspectral imaging. Postharvest Biology and Technology, 2018, 139: 115-126.

［35］   Siripatrawan, U., Makino, Y., Kawagoe, Y., & Oshita, S. (2011). Rapid detection of Escherichia coli contamination in packaged fresh spinach using hyperspectral imaging. Talanta, 85(1), 276-281.

［36］   Qin, J., Burks, T.F., Zhao, X., Niphadkar, N., Ritenour, M.A., 2012. Development of a two-band spectral imaging system for real-time citrus canker detection. J. Food Eng. 108, 87.93.

［37］   ZHAO, Yan-Ru, et al. Hyperspectral imaging for determining pigment contents in cucumber leaves in response to angular leaf spot disease. Scientific reports, 2016, 6: 27790.

［38］   Sun, Y., Wang, Y., Xiao, H., Gu, X., Pan, L., & Tu, K. (2017). Hyperspectral imaging detection of decayed honey peaches based on their chlorophyll content. Food chemistry, 235, 194-202.

［39］   Schmilovitch, Z. E., Ignat, T., Alchanatis, V., Gatker, J., Ostrovsky, V., & Felföldi, J. (2014). Hyperspectral imaging of intact bell peppers. Biosystems engineering, 117, 83-93.

［40］　Feng, H., Chen, G., Xiong, L., Liu, Q., & Yang, W. (2017). Accurate Digitization of the Chlorophyll Distribution of Individual Rice Leaves Using Hyperspectral Imaging and an Integrated Image Analysis Pipeline. Frontiers in plant science, 8, 1238.

［41］　Bergsträsser, S., Fanourakis, D., Schmittgen, S., Cendrero-Mateo, M. P., Jansen, M., Scharr, H., & Rascher, U. (2015). HyperART: non-invasive quantification of leaf traits using hyperspectral absorption-reflectance-transmittance imaging. Plant methods, 11(1), 1.

［42］　GUO, Chentong, et al. Hyperspectral imaging analysis for ripeness evaluation of strawberry with support vector machine. Journal of Food Engineering, 2016, 179: 11-18.

［43］　ELMASRY, Gamal, et al. Hyperspectral imaging for nondestructive determination of some quality attributes for strawberry. Journal of Food Engineering, 2007, 81.1: 98-107.

［44］　TALLADA, Jasper G.; NAGATA, Masateru; KOBAYASHI, Taichi. Non-destructive estimation of firmness of strawberries (Fragaria× ananassa Duch.) using NIR hyperspectral imaging. Environmental Control in Biology, 2006, 44.4: 245-255.

［45］　NANYAM, Yasasvy, et al. A decision-fusion strategy for fruit quality inspection using hyperspectral imaging. Biosystems engineering, 2012, 111.1: 118-125.

［46］　SIEDLISKA, Anna, et al. Detection of fungal infections in strawberry fruit by VNIR/SWIR hyperspectral imaging. Postharvest Biology and Technology, 2018, 139: 115-126.

［47］　Qiang LiuKe SunJing PengMengke XingLeiqing PanKang Tu. Identification of Bruise and Fungi Contamination in Strawberries Using Hyperspectral Imaging Technology and Multivariate Analysis. Food Analytical Methods, 2018, Volume 11, Issue 5: 1518-1527.

［48］ GOYAL, Parash, et al. Adsorption refrigeration technology–An overview of theory and its solar energy applications. Renewable and Sustainable Energy Reviews, 2016, 53: 1389-1410.

［49］ Sah, R. P., Choudhury, B., & Das, R. K. (2016). A review on low grade heat powered adsorption cooling systems for ice production. Renewable and Sustainable Energy Reviews, 62, 109-120.

［50］ Yang, M., Lee, S.Y., Chung, J.T. and Kang, Y.T. (2017) High Efficiency H_2O/LiBr Double Effect Absorption Cycles with Multi-Heat Sources for Tri-Generation Application. Applied Energy, 187, 243-254.

［51］ Wang, Z., Han, W., Zhang, N., Liu, M. and Jin, H. (2017) Proposal and Assessment of a New CCHP System Integrating Gas Turbine and Heat-Driven Cooling/Power Cogeneration. Energy Conversion and Management, 144, 1-9.

［52］ Mohan, G., Kumar, U., Pokhrel, M.K. and Martin, A. (2016) Experimental Investigation of a Novel Solar Thermal Polygeneration Plant in United Arab Emirates. Renewable Energy, 91, 361-373.

［53］ Chitsaz, A., Hosseinpour, J. and Assadi, M. (2017) Effect of Recycling on the Thermodynamic and Thermoeconomic Performances of SOFC Based on Trigeneration Systems; A Comparative Study. Energy, 124, 613-624.

［54］ Moya, M., Bruno, J.C., Eguia, P., Torres, E., Zamora, I. and Coronas, A. (2011) Performance Analysis of a Trigeneration System Based on a Micro Gas Turbine and an Air-Cooled, Indirect Fired, Ammonia-Water Absorption Chiller. Applied Energy, 88, 4424-4440.

［55］ Grisel, R.J.H., Smeding, S.F. and Boer, R. (2010) Waste Heat Driven Silica Gel/Water Adsorption Cooling in Trigeneration. Applied Thermal Engineering, 30, 1039-1046.

［56］　Chorowski, M. and Pyrka, P. (2015) Modelling and Experimental Investigation of an Adsorption Chiller Using Low-Temperature Heat from Cogeneration. Energy, 92, 221-229.

［57］　Kong, X.Q., Wang, R.Z., Wu, J.Y., Huang, X.H., Huang fu, Y., Wu, D.W. and Xu, Y.X. (2005) Experimental Investigation of a Micro-Combined Cooling, Heating and Power System Driven by a Gas Engine. International Journal of Refrigeration, 28, 977-987.

Chapter 2. Study on storage conditions and quality evaluation of agricultural products

Storage temperature and relative humidity are dramatically influence the storage period of fruits and vegetables. Optimal storage conditions can extend the storage life by decelerating the development of physiological changes, inhibiting the growth of spoilage microorganisms and slowing the activity of pathogens. In food safety and quality evaluation of fruits and vegetables, the measurement and observation of chlorophyll contents and distributions in leaves are extensively applied for providing invaluable information about plant physiological activity such as leaf senescence and plant nutrient. Water is one of the most essential ingredients of fresh fruits and vegetables, which may exceed 90% of the weight. Moisture loss is a critical physiological process that is mainly attributed to transpiration. Moisture loss of fresh commodities will result in quality issues such as weight reduction, wilting, shriveling, discoloration, nutrient loss, which will render economic consequences. In general, most fresh commodities become unsalable when a reduction of moisture is more than 3 ~ 10% by weight [1]. For example, a moisture loss of 3% and 6% at spinach and strawberry respectively, may lead to the entire commodity unacceptable for sale [2]. Therefore, the analysis of moisture content during storage period can contribute to better apprehend the phenomenon of transpiration in fresh commodities and storage conditions, and thus reduce the quality loss. Total soluble solid (TSS), a crucial index with respect to fruits and vegetables quality, refers to the total amount of soluble constituents in a fruit or vegetable, will also be analyzed.

2.1 Storage container

The experiments were conducted inside a cold storage container has exterior dimensions of 3.6 m (length) × 1.8 m (width) × 2.5 m (height). The container wall was made of a layer of polyurethane foam panel (43 mm) between two layers of plywood (5 mm). The cold storage container was equipped with a refrigeration system (ERA- RP15B, Mitsubishi Electric Corporation, Japan), whose evaporator unit was located on the ceiling with refrigerating capacity of 3.71 ~ 4.39 kW and air volume of 50 ~ 55 m3/min. The

evaporator fans circulated the air throughout the container to remove the heat which was generated by the samples or infiltrated and conducted from the environment. To achieve uniform distribution cool air inside the container, a metal grill was located just under the refrigeration unit. The air velocity was adjustable a wide range corresponded to the speed of evaporator fan which could be changed by the frequency control panel located outside the container.

The relative humidity inside the container was monitored and controlled by a humidity controller (RHC-C11, H.IKEUCHI & Co., Ltd., Japan) nearby the returning air grille of the evaporator, with a measurement accuracy of ±3%. An AE-4 (03C) atomizer (AKIMist®"E", H.IKEUCHI & Co., Ltd., Japan) with a spray volume of 9.6 L/h at air pressure of 0.3 MPa, installed at the top of container, was controlled by the humidity controller. When the relative humidity monitored was lower than the setting value, the atomizer was switched on to increase the relative humidity until it reached the setting value. The atomizer was connected to the pressurized air and water branches. Pressurized air, which was supplied by an air compressor (SP-5S, Hitachi, Ltd., Japan, capacity: 22 ~ 27 L/min) located outside of the container, was injected to the atomizer as atomizing medium to disintegrate the water into fine spray droplets with mean diameter of 7.5 μm. The water that produced the droplets was pumped into the atomizer from a 120 L water tank (TXS-100, Tohkemy Corporation, Japan) by using an electromagnetic pump (MPA-200, Tohkemy Corporation, Japan). The water flow rate through the atomizer was adjusted by a frequency converter and had a maximal flow rate of 200 mL/min at proof pressure of 0.2MPa. Temperature and relative humidity were monitored by using a TA652 sensor (Toplas Engineering Co., Ltd., Japan) has an applicable range of -25 ~ 100 °C and 0 ~ 100% RH for temperature and relative humidity, respectively. This sensor was connected to a data acquisition system (NR-600, Keyence) to record temperature and relative humidity every 2 seconds. In order to reduce the ethylene, carbon dioxide or undesirable odors produced by the samples, the container was equipped with a ventilator capable of refreshing the air.
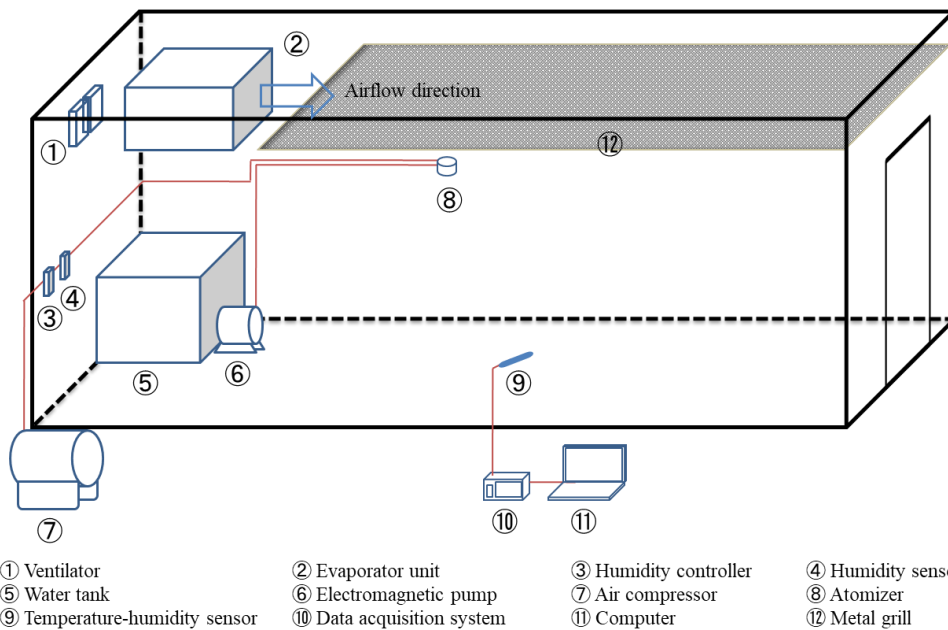
① Ventilator   ② Evaporator unit   ③ Humidity controller   ④ Humidity sensor
⑤ Water tank   ⑥ Electromagnetic pump   ⑦ Air compressor   ⑧ Atomizer
⑨ Temperature-humidity sensor   ⑩ Data acquisition system   ⑪ Computer   ⑫ Metal grill

Figure 2-1. The sketch of storage container: (a) External view (source from), (b) perspective drawing.

2.2 Materials and storage conditions

All samples used in this research, spinach (5 packages), komatsuna (5 packages), and two strawberry cultivars (1 punnet Benihopp and 1 punnet Yumenoka) were purchased on the same day from a supermarket located in Nagoya, Japan. 10 fresh unblemished spinach and komatsuna leaves, which free of decay, bruises and incurve, were selected respectively for hyperspectral imaging analysis and were placed on the transparent polypropylene boxes (331 mm × 260 mm × 48 mm). The remaining samples of spinach and komatusna were

used for visual quality evaluation and were divided into several unsealed polyethylene bags which were placed in a plastic vegetable crate (595 mm by 400 mm, 210 mm in height) having ventilation slots on the sides and bottom for rapid cooling. Fruits with symptoms of damage of strawberries were discarded.

Table 2-1 Samples and storage conditions

Sample	Storage temperature [°C]	Storage relative humidity %
Spinach,	0	80
		90
Komatsuna,		
	5	90
Strawberry		
	10	90

The measurements of hyperspectral images and visual quality ratings were conducted 8 times throughout the storage period: at day 1 (the day of purchase, data not shown), 2, 4, 6, 8, 10, 12 and 14.

2.3 Quality evaluation method

2.3.1 Hyperspectral imaging

The reflectance spectra of the samples were acquired through a lab-scale hyperspectral imaging system mainly consisting of a camera (Cosmos Eye HSC1702, Hokkaido Satellite Co., Ltd., Japan), a light source, and a computer. Figure 2-2 indicates the illustration of hyperspectral imaging system. The camera creates a spectrum from 350 to 1050 nm with a spectral resolution under 10 nm and a sampling interval of 5 nm, the chematic diagram of the hyperspectral camera is shown in Figure 2-3. The distance of the sample from the camera lens was 60 cm and the angle between the lens axis and the sample was 50˚. One incandescent lamp (PS60, 110 V, 60 W, Toyo Trading Ltd., Japan) was used as light source, fixed at an angle of 75˚ to illuminate the sample stage. The hyperspectral images were acquired through a computer (Dynabook Satellite B552/F, Toshiba Corporation, Japan) equipped with scanner software HSCamSharp (Hokkaido Satellite Co., Ltd., Japan). HSDAnalyzer (Hokkaido Satellite Co., Ltd., Japan) was used to analyze the hyperspectral

images by extracting an interested region (approximately 10000 data points) from each image of sample and the average value of the reflectance spectra was computed. As leaves do not discolor in a homogeneous way, appropriate selection of interested regions are extremely important and would largely influence the prediction performance of models. According to the results obtained from the hyperspectral images (Figure 2-3), the distal portion of a leaf blade (as illustrates in Figure 2-14) is selected as the location of interested region due to this portion is most susceptible to changes caused by different conditions. However, it is difficult to select the distal portion of calyx in strawberry as its small surface area; the whole part of calyx was chosen as interested region. In addition, the selection of interested regions was based on the hypothesis that the change of reflectance spectra can be neglected when the regions selected do not match completely.
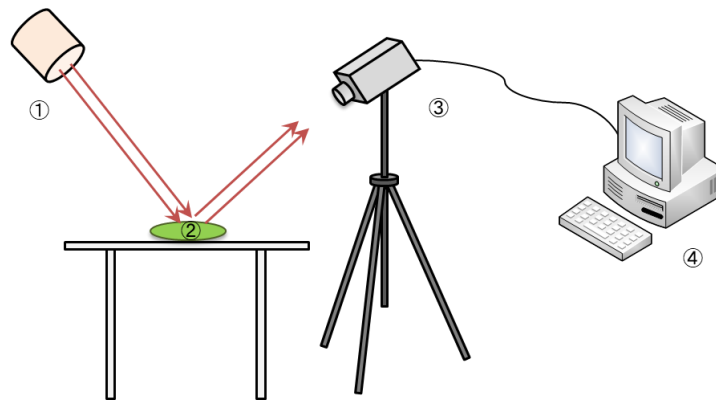
① Light source   ② Sample   ③ Hyperspectral camera   ④ Computer

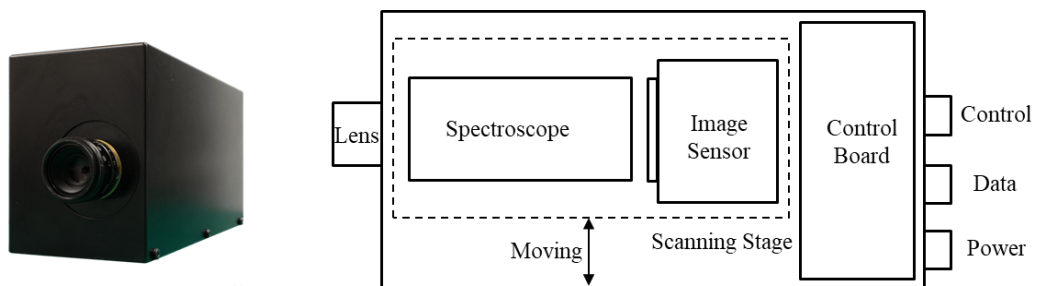**Figure 2-2**. The sketch of hyperspectral imaging system

Figure 2-3. Schematic diagram of the hyperspectral camera

2.3.2 Visual quality rating

Samples were evaluated subjectively by an observer on a 1 ~ 5 scoring system considering the severity of external symptoms (color, shape, gloss, mechanical damage, wilting and decay). The scoring system was modified from Ref. [3], where

5: excellent, (the initial attributes with no surface deterioration or discoloration);

4.5: symptoms between 4 and 5;

4: good (up to 5% surface deterioration or discoloration/yellowish-green color, slight loss of turgidity but no adjustment or only a slight adjustment is needed for sale);

3.5: symptoms between 3 and 4;

3: fair/acceptable (5 to 20% surface deterioration or discoloration, can be commercialized by adjustment);

2.5: symptoms between 2 and 3;

2: poor (20–50% surface deterioration or discoloration, unavailable for sale in spite of the fact that some parts of samples are still good in appearance);

1.5: symptoms between 1 and 2;

1: extremely poor/extremely deteriorated (>50% surface deterioration or discoloration, unavailable for sale completely).

Moreover, the assessment of deterioration concerns damaged or rotten spots and mold growth. The lower limit of shelf life (acceptability for sale) was fixed at 3. Digital images were collected from the samples with an iPhone 7 Plus (Apple Inc.) to illustrate the visual appearance change over the storage period.

2.3.3 Water content measurement

A thermogravimetric moisture analyzer (ML-50, A&D Co., Ltd., Japan), with a weighing resolution of 0.005 g and a minimum scale value of 0.1%, was used to measure the moisture loss. The analyzer used a 400W halogen lamp as heating source and had a heating temperature range of 50 ~ 200 °C (1 °C increment). Samples were placed onto a

stainless-steel pan before being put on the built-in balance of analyzer that was connected to a computer by serial interface cable and the results were monitoring and recording using "WinCT" software. Moisture content was calculated based on wet sample weight as follows:

$$\%mc = \frac{W_w - W_d}{W_w} \times 100 \tag{2-1}$$

where, W_w is wet sample weight and W_d is dried sample weight.

In this study, moisture content was analyzed in samples of spinach and komatsuna. Each analysis 3 ~ 4 leaves depending on the size of the leaf were plucked arbitrarily from the samples which were packaged in the polyethylene bags. All the leaves plucked were divided into two parts: blade and petiole that was analyzed separately due to the different moisture contents lead to different drying times. Three replicates per analysis, and the mean values were calculated.

2.3.4 Total soluble solid measurement

Brix% is an indicator of total soluble solid and is widely applied in the agriculture and food industries. The value detected from a Brix% instrument is used to define the number of grams of sucrose contained in 100 g of pure water. In this study, the total soluble solid of all samples was analyzed by applying a digital automatic temperature compensating refractometer (PAL-1, Atago Co., Ltd., Japan), which was expressed as Brix% with a range of 0~53% in 0.1% graduations.

As indicated in Figure 2-4, the juice was extracted from sample (four or five leave samples were randomly taken from the packages of spinach or komatsuna, and the selection of two to four fruit samples from each strawberry cultivar was also randomized) with a hand squeezer and was placed on the prism of the refractometer. The readings were recorded in Brix%, and the sum total of all readings for each sample was averaged to obtain a mean value.
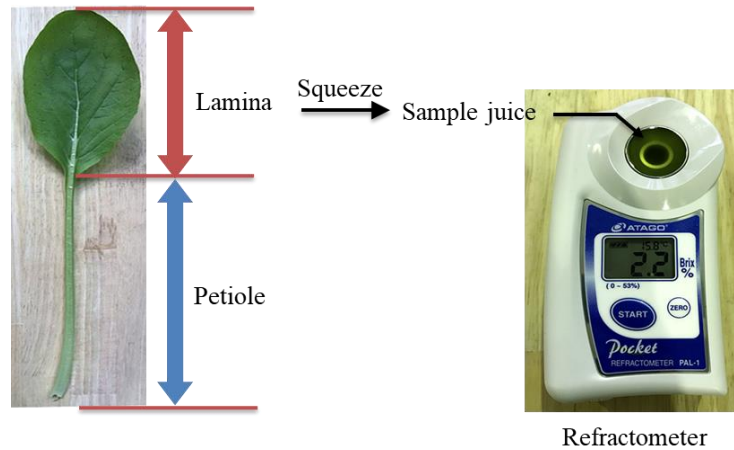
Refractometer

Figure 2-4. Schematic for total soluble solid measurement

2.4 Visual quality rating of samples

Substantial differences in the visual appearances were observed in the spinaches and komatsuna stored at different temperatures are shown in Figure 2-5 and Figure 2-6. During the first 2 days of storage, both samples maintained the same visual appearance scores as the initial day at all storage temperature conditions. From the third day of storage, however, samples stored at 10 °C and 5 °C exhibited rapid appearance deterioration and dropped below the acceptable value after 8 days and less than 9 days for spinach and after 10 days and 12 days for komatsuna, respectively. The inferior visual appearances of spinaches exposed to 10 °C and 5 °C were primarily due to discoloration (yellowing of the leaves), tissue softening, and loss of gloss and turgidity, which were considerably more pronounced for samples stored at 10 °C than at 5 °C, as can be seen from Figure 2-5. Similar trends were detected for appearance changes of komatsuna exposed to high storage temperatures, but the deteriorations were mainly reflected in the yellowing of the leaves and slight abscission of the leaves. The rapid and continuous changes in discoloration at higher storage temperature manifested the substantial decline in chlorophyll during the storage period. From Figure 2-5 and 2-6, it can be demonstrated that the visual appearances were sustained at a relative high level of 4 over the 14 days storage period when samples stored at 0 °C. These were also reflected in Figure 4-9 to 4-12, from which can be known that no visible discoloration, browning development or rotten spots were identified.
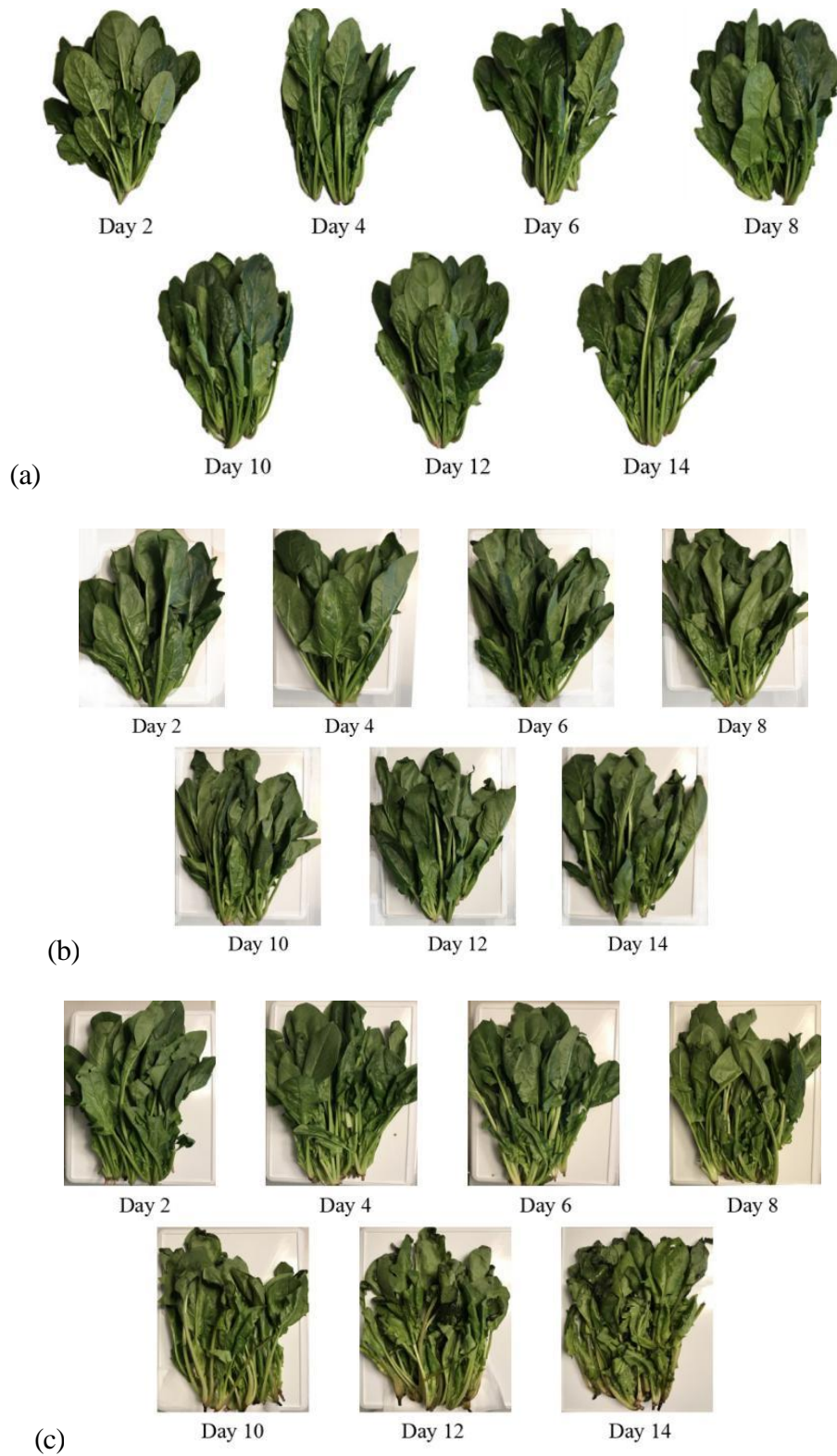
Figure 2-5. Visual quality changes of spinaches with various storage periods at various storage temperature: (a) 0 ℃; (b) 5 ℃; (c) 10 ℃
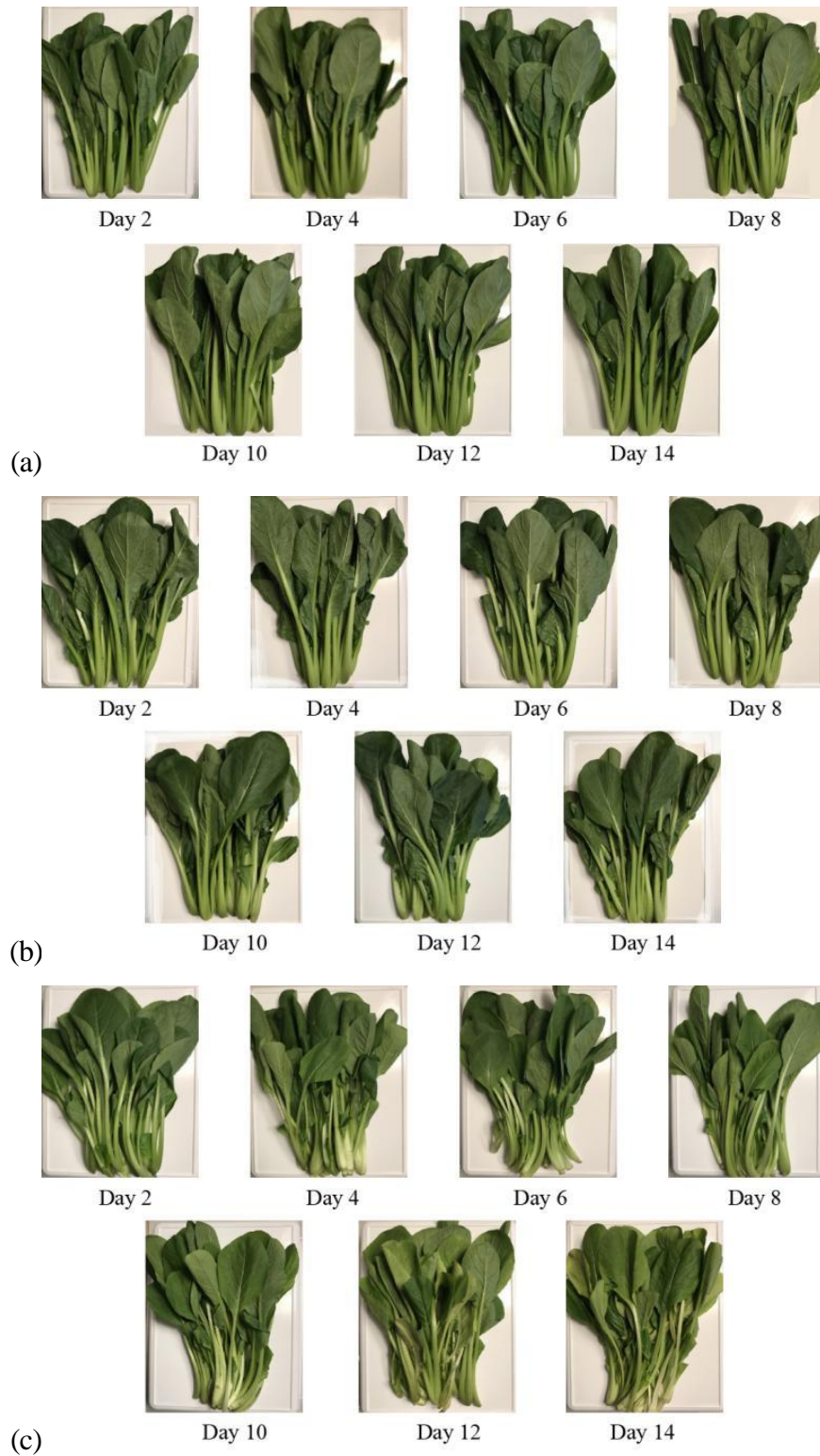
Figure 2-6. Visual quality changes of komatsuna with various storage periods at various storage temperature: (a) 0 °C; (b) 5 °C; (c) 10 °C

Substantial differences in the visual appearances were observed in the two types of strawberry (Yumenoka and Benihoppe) stored at different temperatures are shown in Figure 2-7 and Figure 2-8. As shown in Figure 2-7 and 2-8, there was no difference between Yumenoka and Benihoppe in shelf life stored at 0 ℃. Both of them maintained a good visual quality during the storage period, consequently, had relative high scores of 4 after 14 days of storage. However, the difference in shelf life between these two strawberry cultivars was significant when they were stored at 5 ℃. As storage proceeded, Yumenoka at 5 ℃ decreased significantly in visual quality and exceeded the unacceptable limit on day 8, while Benihoppe declined gradually and maintained an acceptable quality for sale during the two-week storage. After 9 days of storage, Yumenoka fruits appeared slight fungal growth and then increased rapidly. The fruits were thoroughly permeated with fuzzy gray mycelium after 12 days of storage. Benihoppe stored at 10 ℃ had a similar change of visual quality as Yumenoka at 5 ℃, showing a rapid decrease in visual quality from the initial day and the occurrence of fungal growth was discovered on day 7 and became more evident and severe until most of the fruits were completely covered with gray velvety spores. It is noteworthy that a small part of the Benihoppe became mushy and oozing out juice on day 6 before fungi were observed.
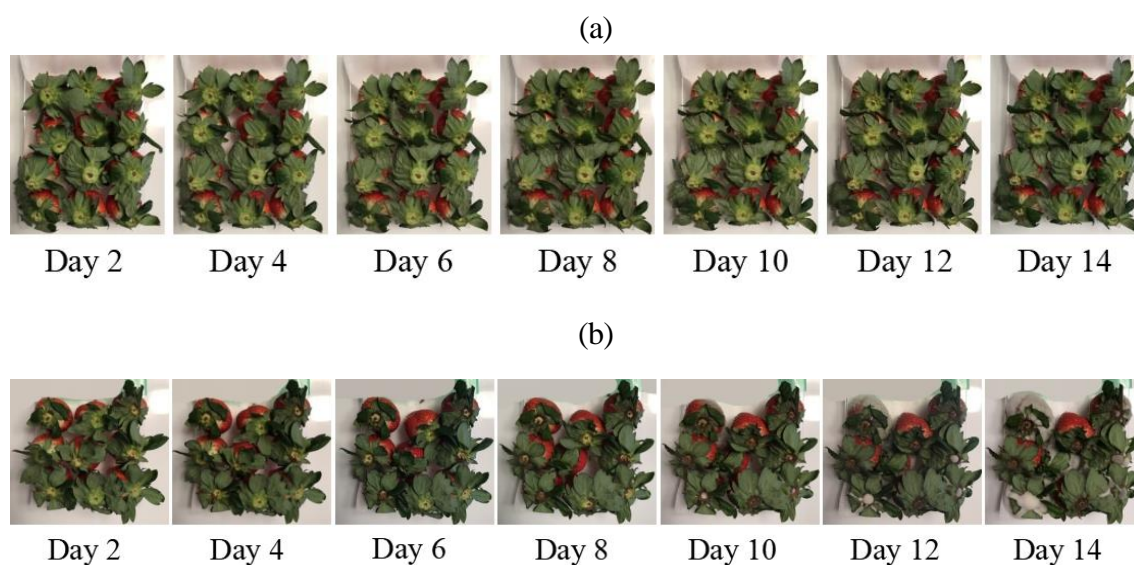
(a)

| Day 2 | Day 4 | Day 6 | Day 8 | Day 10 | Day 12 | Day 14 |

(b)

| Day 2 | Day 4 | Day 6 | Day 8 | Day 10 | Day 12 | Day 14 |

Figure 2-7. Visual quality changes of Yumenoka with various storage periods at various storage temperature: (a) 0 ℃; (b) 5 ℃

(a)

| Day 2 | Day 4 | Day 6 | Day 8 | Day 10 | Day 12 | Day 14 |

(b)

| Day 2 | Day 4 | Day 6 | Day 8 | Day 10 | Day 12 | Day 14 |

(c)

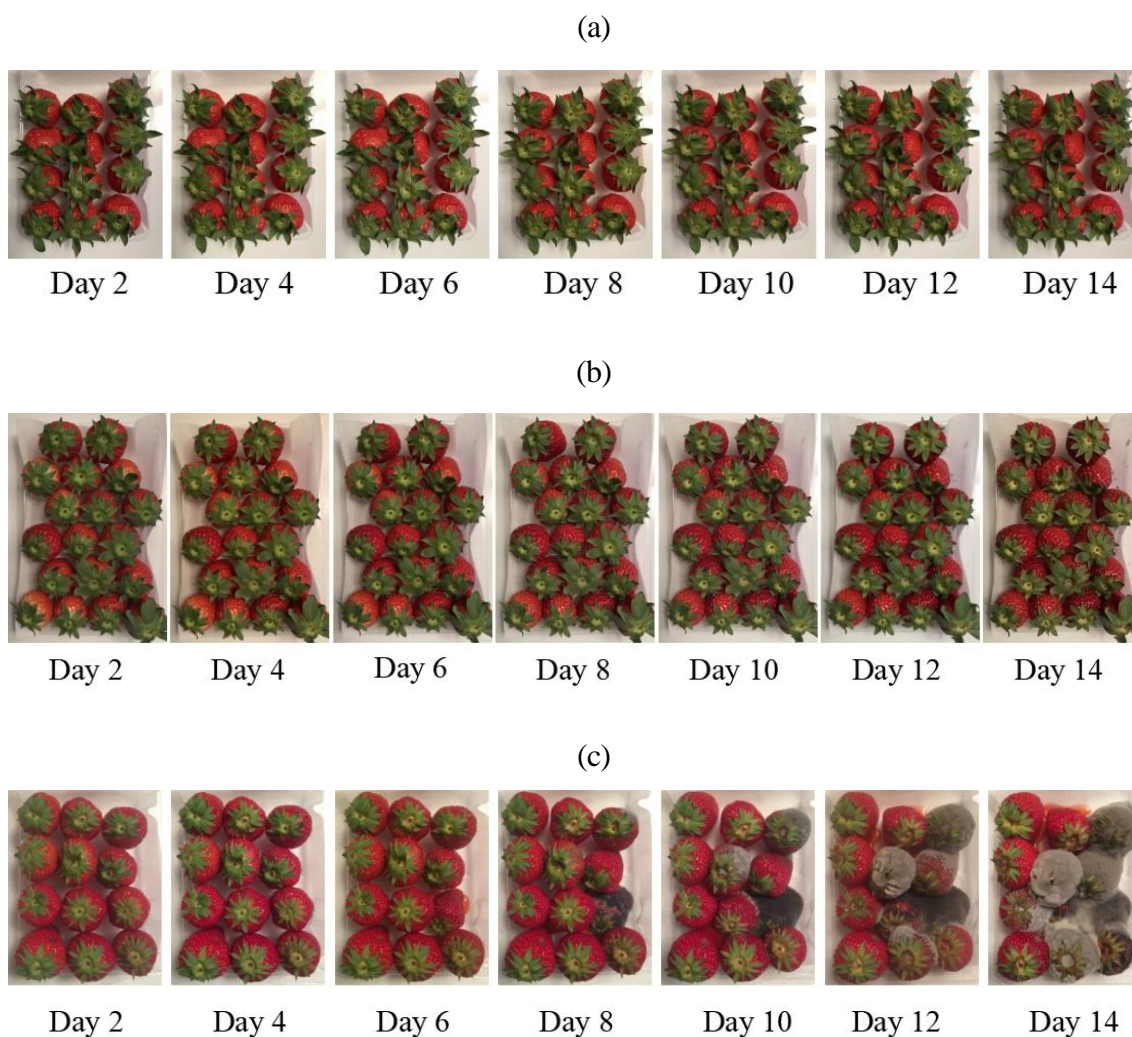| Day 2 | Day 4 | Day 6 | Day 8 | Day 10 | Day 12 | Day 14 |

Figure 2-8. Visual quality changes of Benihoppe with various storage periods at various storage temperature: (a) 0 °C; (b) 5 °C; (c)10 °C

Gray fungal, caused by Botrytis cinerea, is the most prevailing pathogen of strawberry and can infect fruits at any time. On average, the incidence of gray fungal found at strawberry is 10 ~ 15%, according to the study of Kim et al. [4]. Strawberries stored at 0 °C did not show fungal decay during the whole storage period, indicating that low storage temperature can effectively retard the fungal decay in strawberries. In addition, browning of the calyxes and overripe appearance (color changed from light red to dark red) were detected for Yumenoka at 5 °C and Benihoppe at 10 °C during storage time.

2.5 Hyperspectral images investigation

The hyperspectral images together with the related digital images that obtained from spinach, komatsuna, Yumenoka, and Benihoppe at three different storage temperatures were illustrated in Figure 4-9 to Figure 4-12, respectively. The hyperspectral images presented in this study were a combination of spectral images at two wavelength regions: the red (630 ~ 690 nm) and the near infrared (740 ~745 nm) regions.
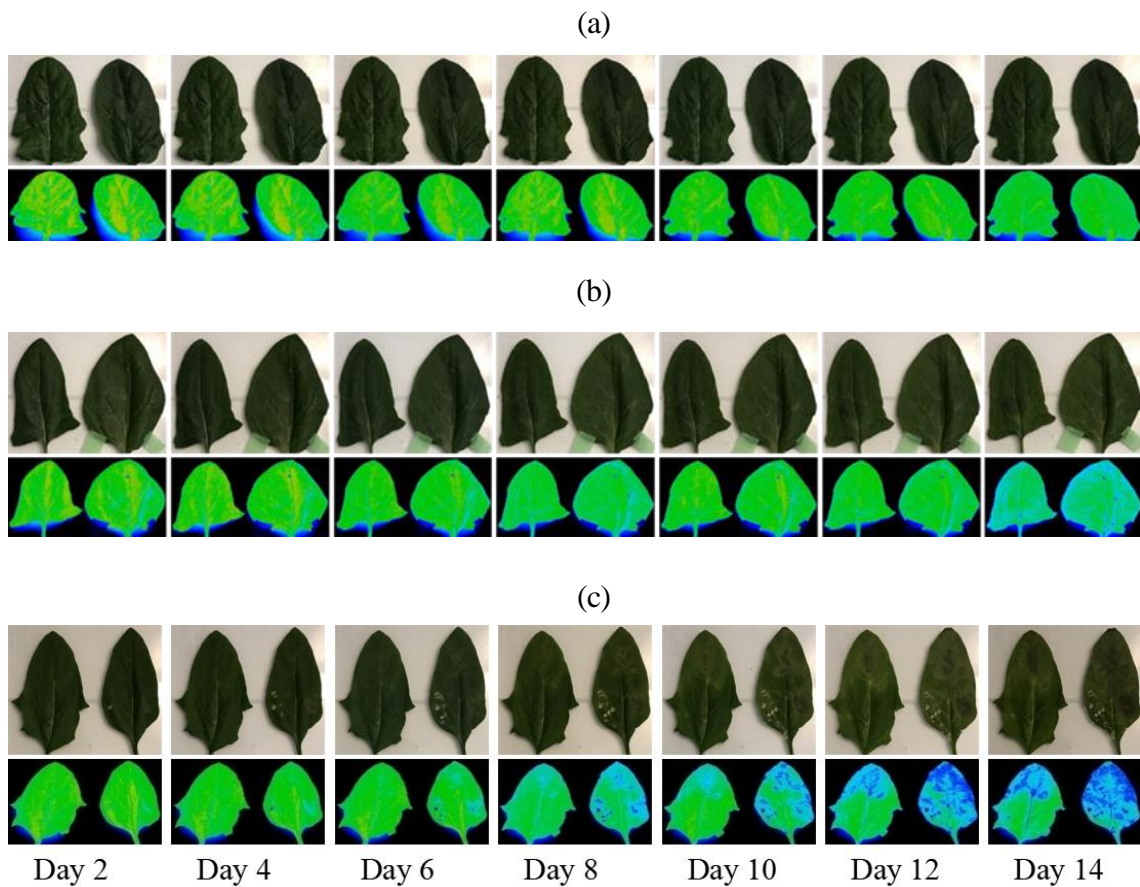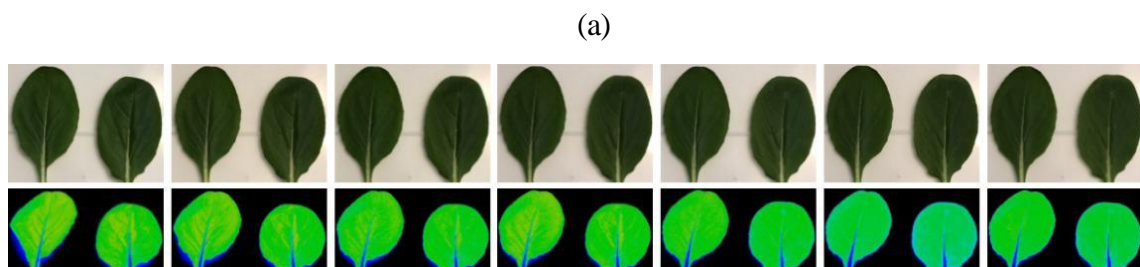
(a)

(b)

(c)

| Day 2 | Day 4 | Day 6 | Day 8 | Day 10 | Day 12 | Day 14 |

Figure 2-9. Hyperspectral images together with the related digital images of spinach over the storage period at various temperatures: (a) 0 ℃; (b) 5 ℃; (c) 10 ℃

(a)

(b)

(c)

| Day 2 | Day 4 | Day 6 | Day 8 | Day 10 | Day 12 | Day 14 |
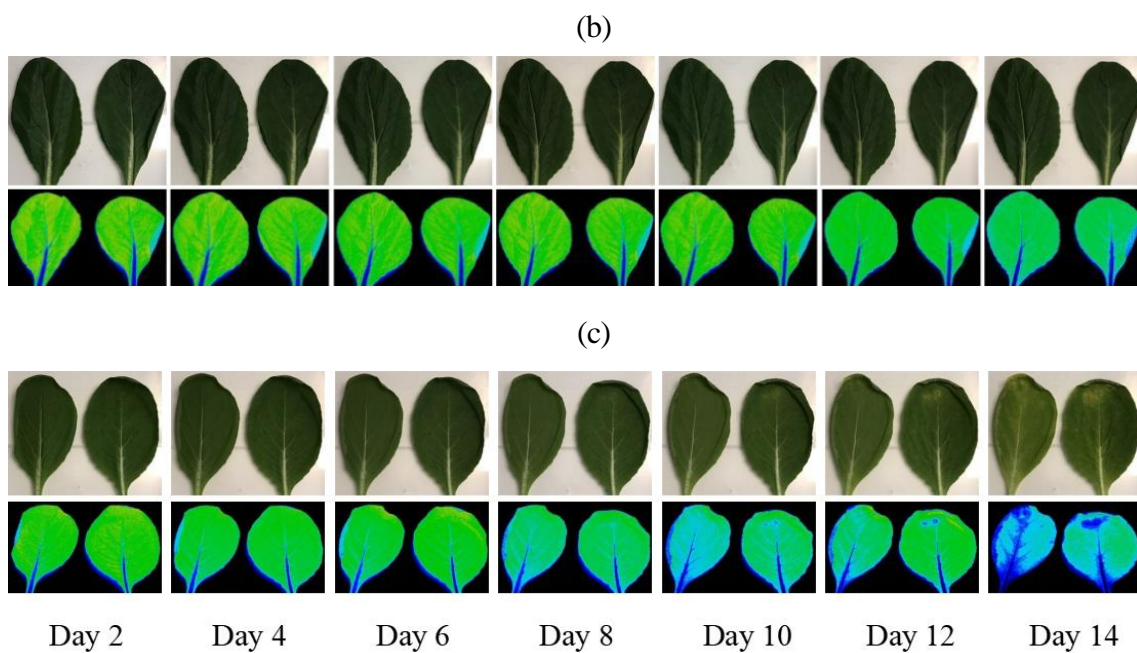
Figure 2-10. Hyperspectral images together with the related digital images of komatsuna over the storage period at various temperatures: (a) 0 °C; (b) 5 °C; (c) 10 °C
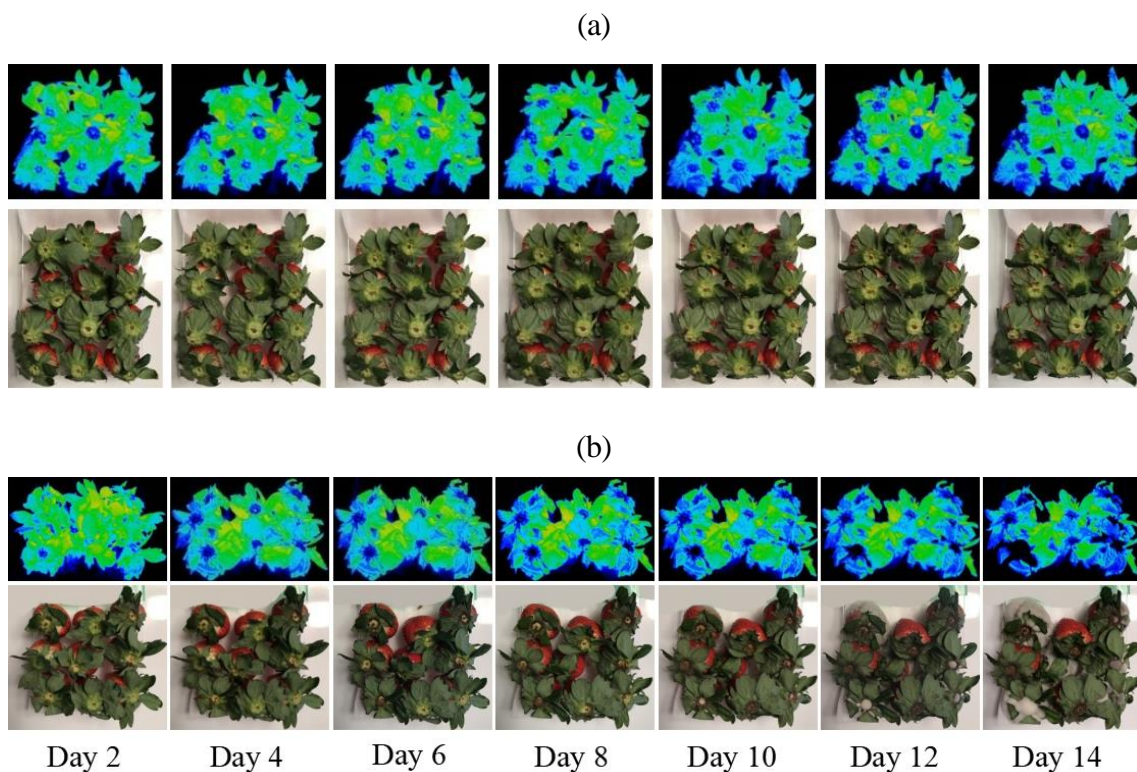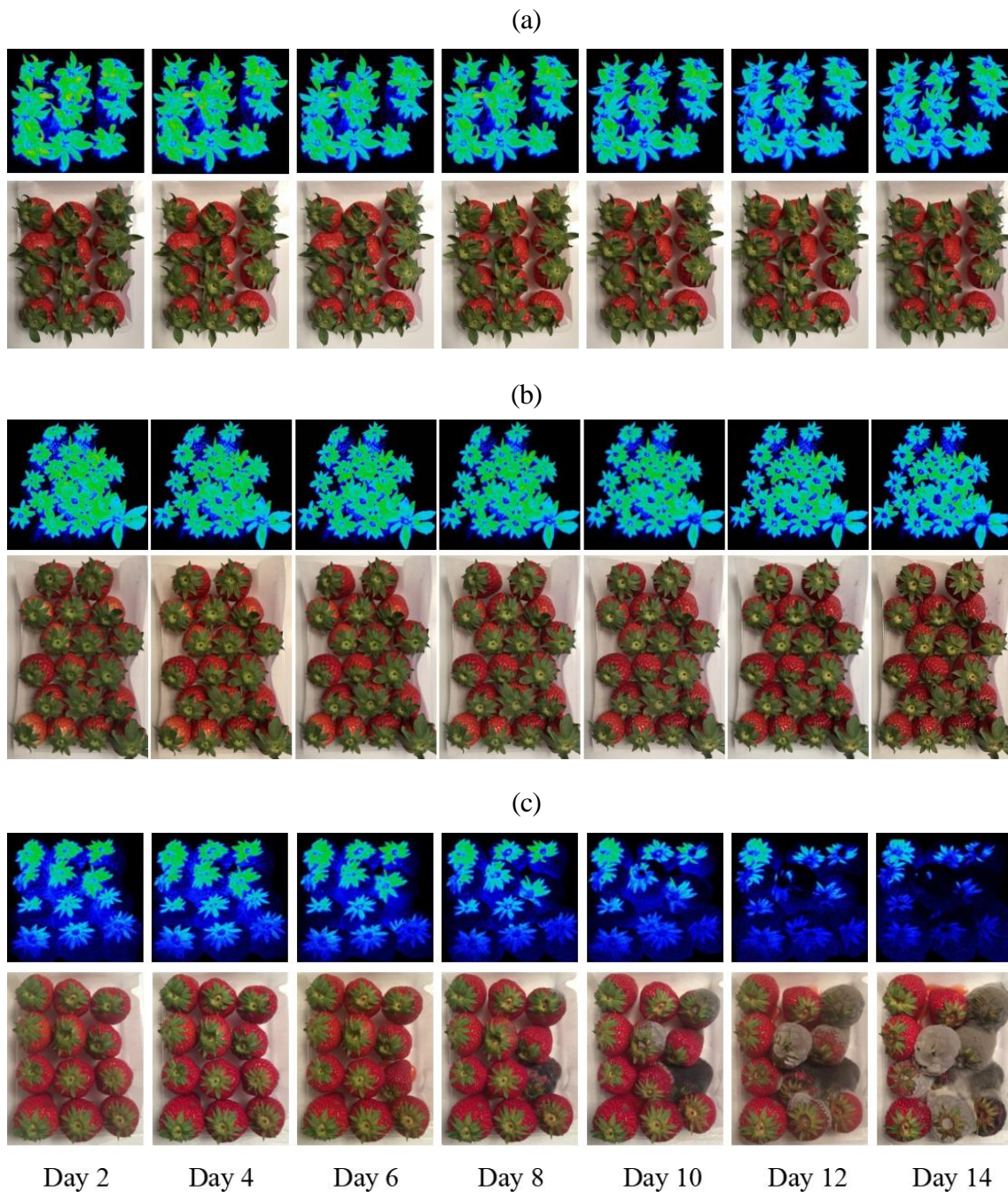
(a)

(b)

| Day 2 | Day 4 | Day 6 | Day 8 | Day 10 | Day 12 | Day 14 |

Figure 2-11. Hyperspectral images together with the related digital images of Yumenoka over the storage period at various temperatures: (a) 0 °C; (b) 5 °C

43

(a)

(b)

(c)

Day 2   Day 4   Day 6   Day 8   Day 10   Day 12   Day 14

Figure 2-12. Hyperspectral images together with the related digital images of Benihoppe over the storage period at various temperatures: (a) 0 ℃; (b) 5 ℃; (c) 10 ℃

As illustrated in Figure 9 and Figure 12, variations in color were detected among the different areas of a leaf/calyx sample, demonstrating that the chemical components in leaves/calyxes are unevenly distributed. Consequently, the spectral characteristics of a leaf/calyx sample are not uniform. Inter-individual differences of chlorophyll distribution in

44

samples were also found in the hypersperal images, which may be caused by the various underlying factors such as the different degrees of change in the cell structures of the leaves or the difference in light conditions at the growing stage.

The color intensity of the hyperspectral images became weaker across the storage period, and this phenomenon became even more apparent when the samples stored at the higher temperatures (as shown in Figure 2-9(c), Figure 2-10(c), and Figure 2-12(c)). The color change in hyperspectal images can be ascribed to the chlorophyll degradation in leaves/calyxes, as confirmed by the digital images, where discoloration of leaves/calyxes can be observed over time, especially at 10 °C. In addition to the discoloration of calyxes in Benihoppe, fungal growth was discovered at 10 °C. The influence of fungal growth on fruit quality can also be reflected in the discoloration of hyperspectral images, as shown in Figure 2-12(c). In order to better identify the feasibility of using hyperspetral imaging for chlorophyll evaluation, we conducted a control experiment that samples of spinach and komatsuna were exposed 14 days to a 30 °C ambient temperature. As can be seen from Figure 2-13, remarkable discolorations were detected in both samples and, especially in komatsuna, the hyperspectral images turned dark which means there were no chlorophyll pigments in the leaves. Thus, we can infer that the distribution of chlorophyll could be identified in situ in sample leaves or calyxes non-destructively by hyperspetral imaging. Moreover, due to the distal portion of the leaf exhibited a much more rapid appearance deterioration and noticeable color change than the other parts of leaf, this portion was defined as the interested region.
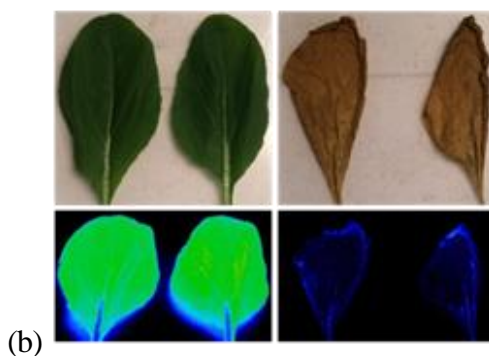

(a)

(b)
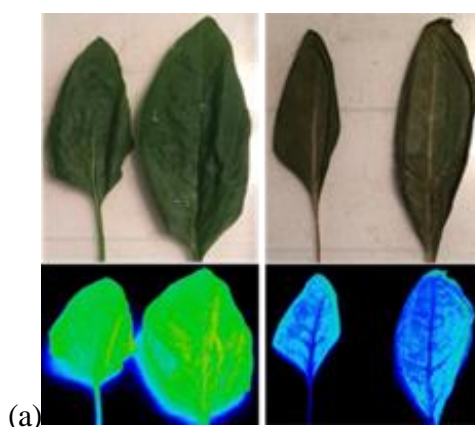
Figure 2-13. Hyperspectral images of (a) spinach, (b) komatsuna exposed at 30 °C ambient temperature

2.6 Normalized reflectance spectrum

As shown in Figure 2-14 and 2-15, the red rectangle part of a sample was selected as the interested region and its average normalized spectral reflectance (is calculated as the ratio of spectral reflectance at each wavelength to the maximum spectral reflectance which often appears at 740 nm) are illustrated in the same figure.
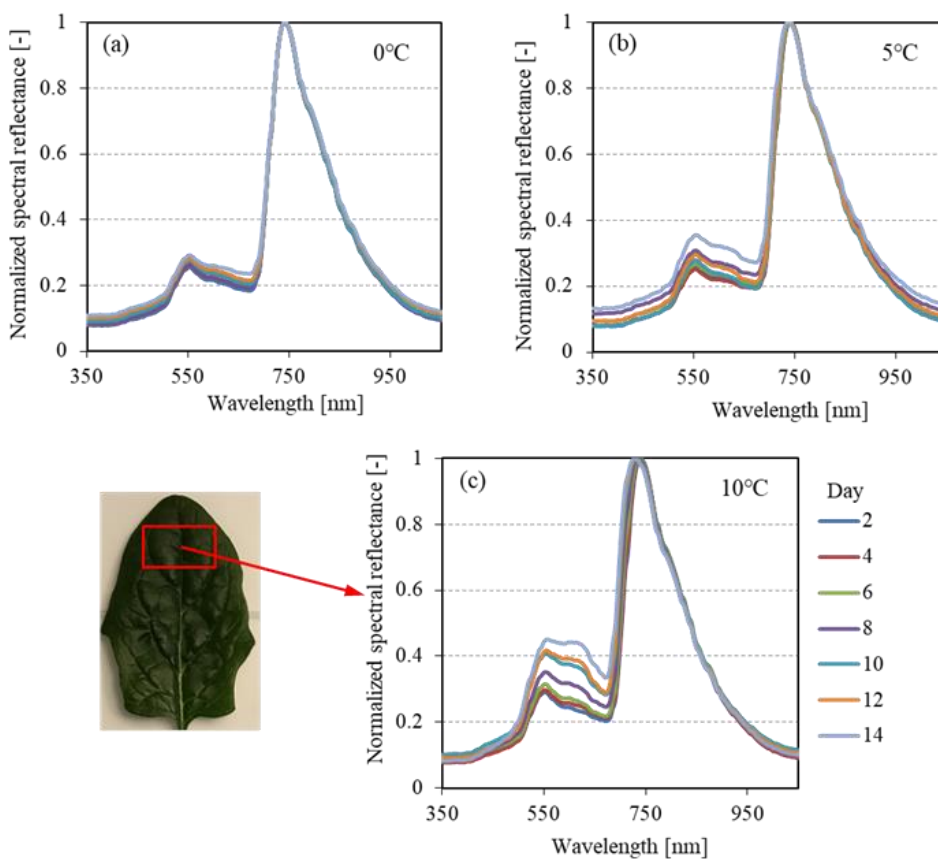
Figure 2-14. The change of spectral reflectance in spinach over the storage period at various temperatures: (a) 0 °C; (b) 5 °C; (c) 10 °C.
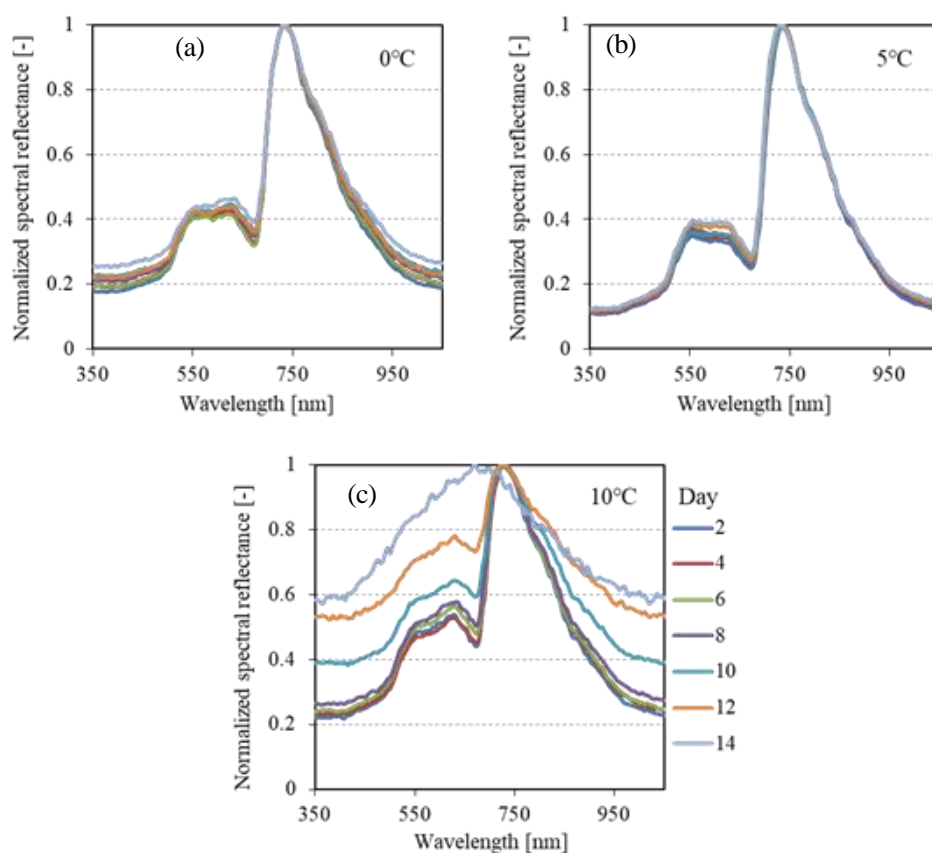

Figure 2-15. The change of spectral reflectance in Benihoppe over the storage period at various temperatures: (a) 0 °C; (b) 5 °C; (c) 10 °C.

As illustrated in Figure 2-14 and Figure 2-15 (except for Figure 2-15(c)), the spectral reflectance in the wavelength region from 350 nm to 500 nm and near 675 nm was low. In the range between 350 nm and 480 nm, where the absorption by carotenoids and chlorophylls take place [4], the reflectance remained basically unchanged and with minimum values less than 0.2. There were two remarkable changes observed in the range of 500 nm to 550 nm which is called the green edge, and in the range of 690 nm to 730 nm which is called the red edge. The maximum value of reflectance was observed at around 740 nm which was irrelevant to the storage period due to the spectral normalization. Then a marked decline towards longer reflectance was measured. The reflectance in the green region increased and the green edge shifted towards shorter wavelengths over the storage

period. The similar spectral character was identified in the red edge region where the reflectance moved towards shorter wavelengths over the storage period.

Higher storage temperatures would accelerate leaf senescence, facilitate plant transpiration and induce thermal stress those contribute to a considerable decrease in the chlorophyll content. The phenomenon of red edge shift was largely influenced by the storage temperatures, as can be seen from the spectral results. Thus, spectra extracted from the red and red edge regions by hyperspectral imaging may provide effective information to evaluate the visual quality change. Leaf senescence or under stress conditions that occur in plants during storage period, accounts for continuous decrease in the concentration of pigments. Thus, spectra extracted from the red edge region by hyperspectral imaging may provide effective information to evaluate the visual quality change.

2.7 Normalized Difference Vegetation Index and visual quality rating

After the analysis of hyperspectral imaging, average spectral values obtained from the interested region of the sample were used to develop the visual quality prediction model. Normalized Difference Vegetation Index (NDVI) is extensively used to assess the chlorophyll content of vegetation [6, 7]. As shown in Equation 1, NDVI is calculated as the difference between the reflectance values in the near infrared (R_{NIR}) and red (R_{RED}) spectral regions, divided by the sum of these two reflectance values.

$$NDVI = \left(R_{NIR} - R_{RED}\right)/\left(R_{NIR} + R_{RED}\right)$$

(2-2)

where R denotes reflectance, and the subscript denotes the corresponding waveband.

The correlation between NDVI and chlorophyll content has been studied by many researchers both at canopy and leaf levels. Many studies [8-10] demonstrated that NDVI was competent to estimate chlorophyll content in plants at low level of chlorophyll. One of the potential reasons for the challenge is the decrease in reflectance-sensitivity to chlorophyll variations in the red region when the chlorophyll content exceeds a threshold value, as mentioned above. The reflectance around 675 nm has been found to be highly associated with the variations in low chlorophyll contents (< 5 μg/cm2), however, has been

proven to be insensitive to the variations in medium to high chlorophyll contents (yellowish-green to dark green leaves) due to the saturation of light absorption [8,11].
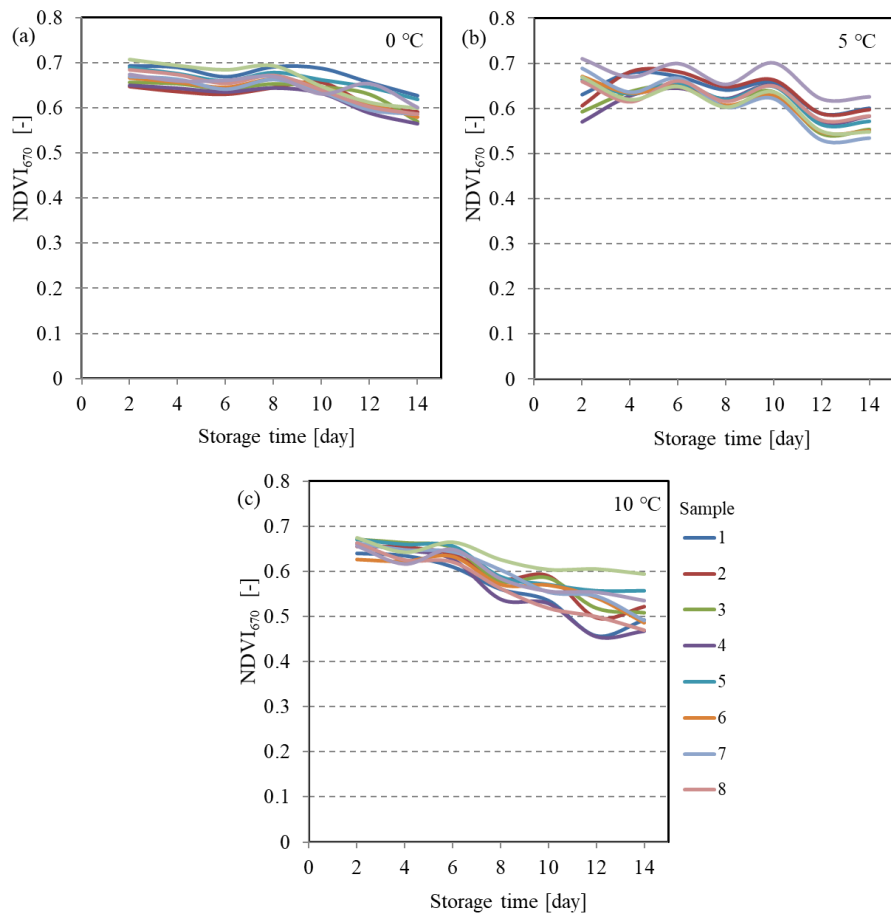

Figure 2-16. $NDVI_{670}$ of spinach over the storage period at various temperatures: (a) 0 °C; (b) 5 °C; (c) 10 °C.

To overcome this obstacle, it requires a waveband that is sensitive to the chlorophyll variations in a wider range of chlorophyll content. The red edge (in the range of 680 ~ 740 nm) is a spectral characteristic of green vegetation, resulting from the combined effect of the strong absorption by chlorophyll in the red region of visible spectrum and the scattering inside the leaf by virtue of leaf internal structure in the near-infrared region [12]. A number of studies [13-15] suggested that the correlation between NDVI and chlorophyll content can be improved by replacing the red wavelength with a wavelength in the red edge region. In contrast to the high light absorption by chlorophyll in red region, the lower one in the red edge can reduce the saturation effect of absorption and remain highly sensitive to

chlorophyll content (up to 44.8 nmol/cm^2) [16]. Moreover, its relationships with the changes of biophysical factors, for instance, leaf orientation, status of the soil, optical properties and solar angle are comparatively poorer [17,18].

Consequently, we investigated and compared two types of NDVI indexes: the first one (NDVI$_{670}$), a conventional index, was computed using spectral reflectance from near infrared (R$_{740}$) and red (R$_{670}$) regions; the second one (NDVI$_{705}$) was calculated by substituting the red edge reflectance (R$_{705}$) for the red reflectance (R$_{670}$), and the equation is given as follow.

$$NDVI_{670} = \left(R_{740} - R_{670}\right)/\left(R_{740} + R_{670}\right) \tag{2-3}$$

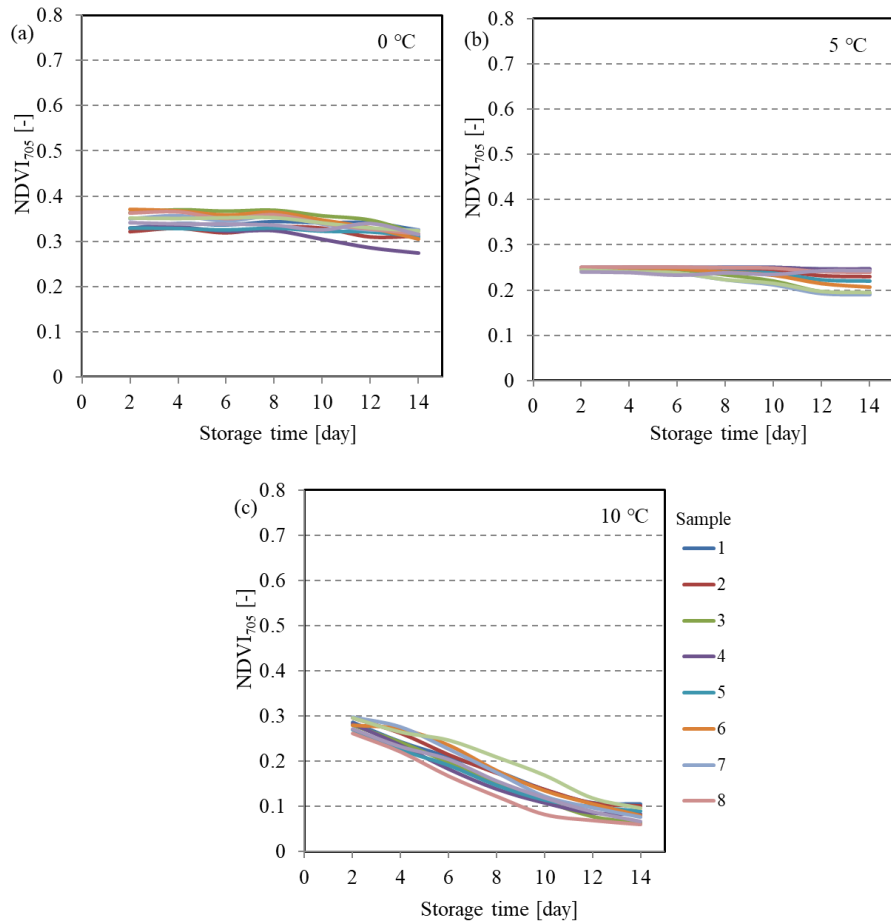$$NDVI_{705} = \left(R_{740} - R_{705}\right)/\left(R_{740} + R_{705}\right) \tag{2-4}$$

Figure 2-17. NDVI$_{705}$ of spinach over the storage period at various temperatures: (a) 0 °C; (b) 5 °C; (c) 10 °C.

In contrast to NDVI$_{670}$, NDVI$_{705}$ has shown a steady decrease over the storage period. This is consistent with the results of previous studies that the reflectance at 705 nm is sensitive to the change of chlorophyll content but less sensitive to biophysical factors, for instance, leaf orientation, status of the soil, optical properties and solar angle are comparatively poorer.
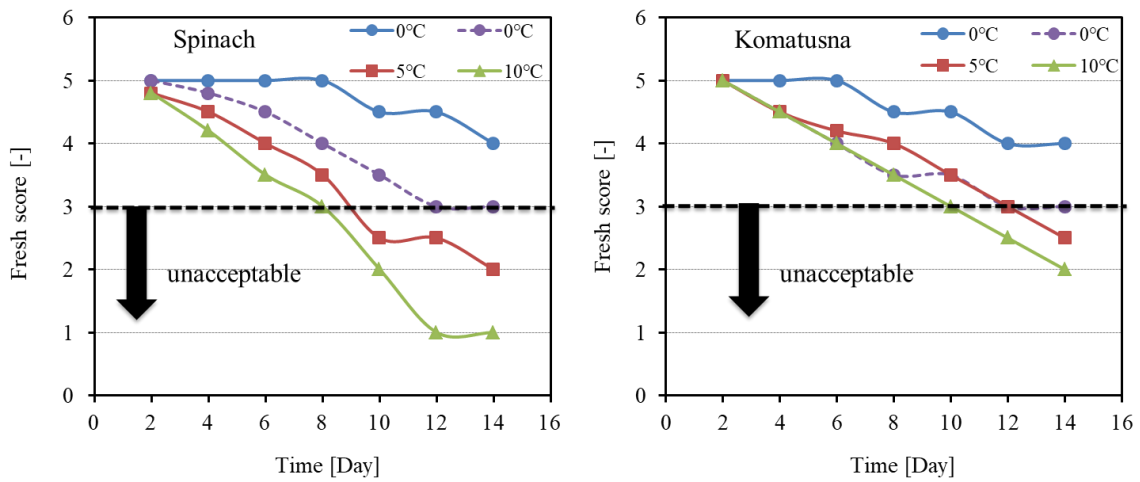

Figure 2-18. Visual quality rating of spinaches and komatsuna during storage periods at various storage temperatures
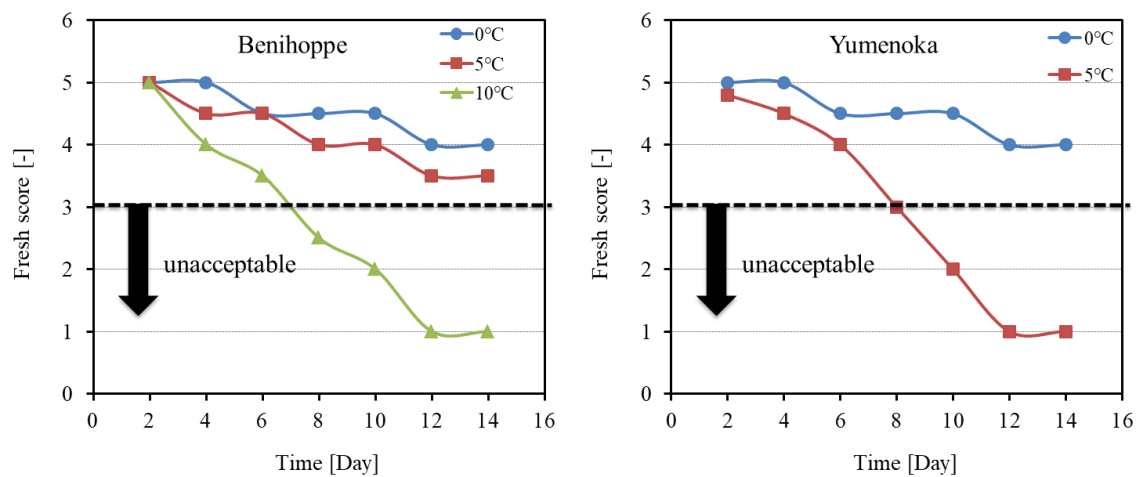

51

Figure 2-19. Visual quality rating of Benihoppe and Yumenoka during storage periods at various storage temperatures

To obtain an alternative method for the visual quality evaluation of fresh products, the correlations of visual quality and NDVI is investigated. Visual quality rating of spinach, komatsuna, and Yumenoka at various storage temperatures are shown in Figure 2-18 and 2-19. However, the visual quality rating is subjective, and the results would vary considerably among inspectors or even if by the same inspector over time [19]. Correlations between visual quality and NDVI changed significantly. One linear regression model could not satisfy all samples studied. Different species or cultivars, and even the same species or cultivars at different storage temperatures have different optimal linear regression models, as shown in Figures 2-20 to 2-23, models with different slopes and intercepts.
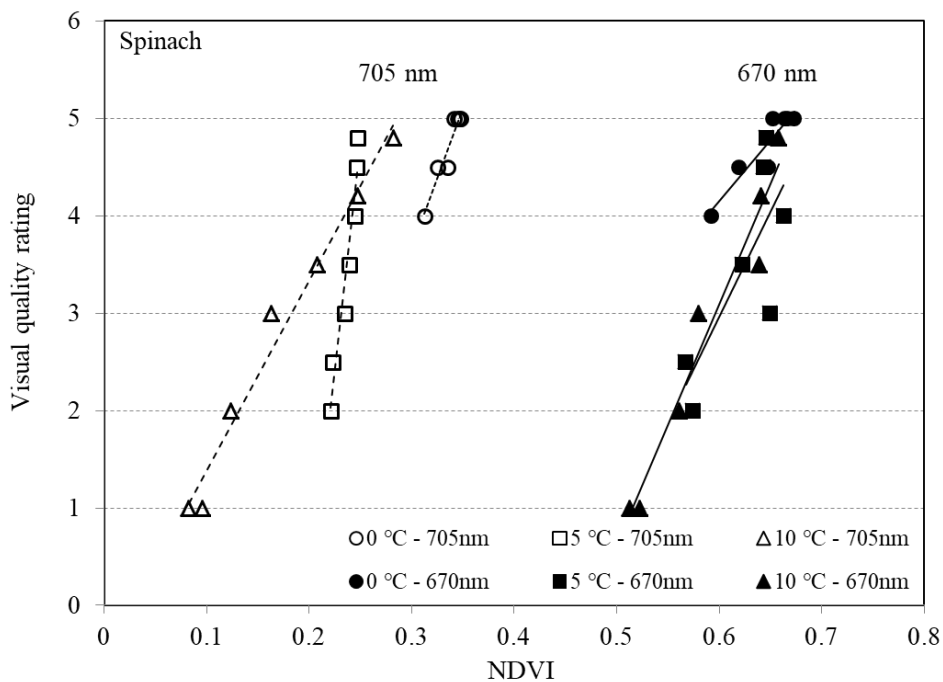

Figure 2-20. Correlations between visual quality rating and $NDVI_{670}$ and $NDVI_{705}$ of spinach at various storage temperatures.
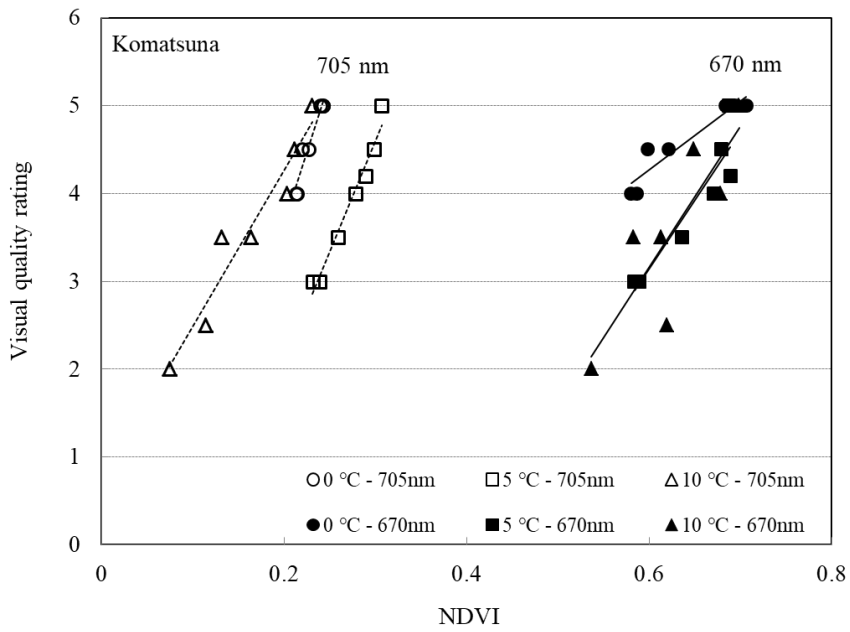
Figure 2-21. Correlations between visual quality rating and NDVI$_{670}$ and NDVI$_{705}$ of komatsuna at various storage temperatures.
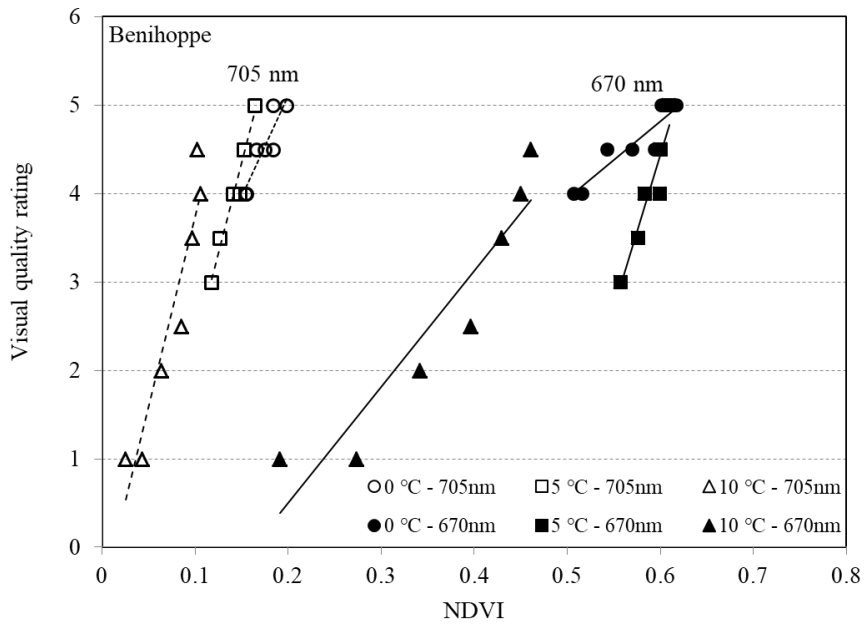

Figure 2-22. Correlations between visual quality rating and NDVI$_{670}$ and NDVI$_{705}$ in Benihoppe at various storage temperatures.
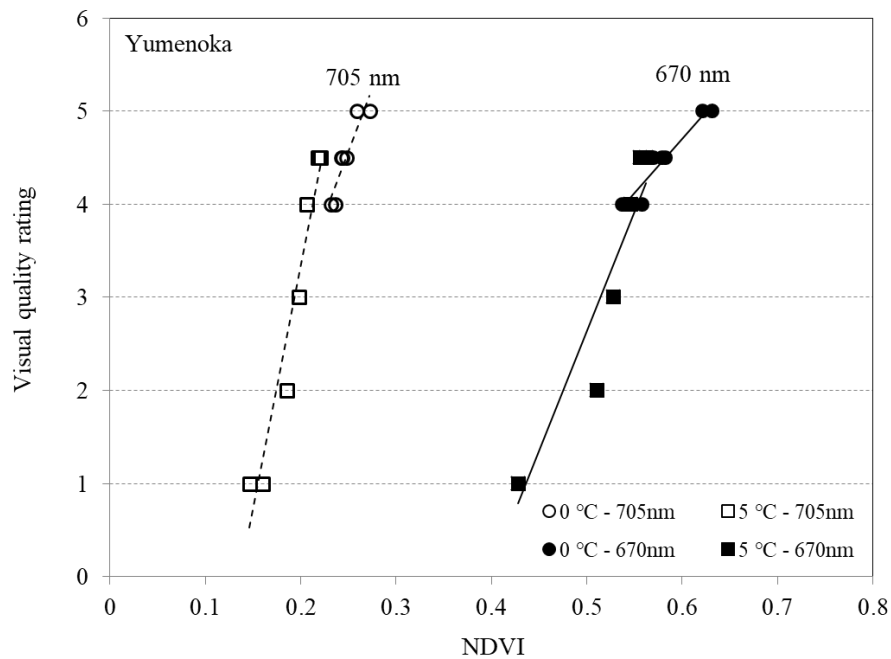
Figure 2-23. Correlations between visual quality rating and $NDVI_{670}$ and $NDVI_{705}$ of Yumenoka at various storage temperatures.

The ranges of visual quality and NDVI had been broadly expanded at higher storage temperatures, mainly due to the higher temperature stress. The coefficients of determination, R^2, between visual quality and NDVI in spinach and komatsuna were higher at 705 nm than at 670 nm are summarized in Table 2-2. However, in contrast to spinach and komatusna, the R^2 values of strawberries stored at 0 °C were higher at 670 nm than at 705 nm. This may be because the visual quality rating of strawberry does not only include the calyx but also the pericarp of the fruit, while the reflectance used to calculate NDVI was measured from the calyx only. At 0 °C, strawberries were maintained at a relatively fresh level and the visual changes of calyx and pericarp were small. Strawberries deteriorated rapidly when stored at higher temperatures, especially in pericarp that generally appeared to deteriorate faster than calyx. In other words, with the increase in storage temperature, the deterioration of pericarp would account for a larger proportion of visual quality rating. On the other hand, NDVI scarcely subjected to the influence from the deterioration of pericarp.

Table 2-2. Coefficients of determination (R^2) of spinach, komatsuna, benihoppe, and yumenoka at various storage temperatures

	0 °C		5 °C		10 °C	
	670 nm	705 nm	670 nm	705 nm	670 nm	705 nm
Spinach	0.8671	0.9345	0.6171	0.9413	0.9534	0.9789
Komatsuna	0.9019	0.9439	0.861	0.9696	0.7154	0.9387
Benihoppe	0.8566	0.831	0.9055	0.9687	0.8794	0.9
Yumenoka	0.9214	0.8674	0.9093	0.9431		

The differences between NDVI and visual quality rating may be explained by the fact that NDVI is analyzed on a continuous scale which involves the visible red wavelength and invisible near infrared wavelength; while visual quality rating is assessed on the basis of rating criteria by human eye can only discern the visible wavelengths. Factors such as surface or internal structure, thickness, chlorophyll content and orientation of the samples and their leaves are responsible for the reflectance spectrum received by hyperspectral camera. Therefore, factors that are invisible to human eye are contributing to NDVI and may confound the correlation between NDVI and visual quality rating. The results indicate that reflectance at 705 nm could be applied to evaluate the visual quality of fresh commodities. This indicates that reflectance at 705 nm had a stronger response to visual quality rating than at 670 nm. As an evaluation of simple correlation, coefficient of determination was computed. It is reasonable to assume that visual quality rating is closely connected to the reflectance of red region due to its visibility.

The experiment-to-experiment variability between the same species that stored at the same condition in visual quality rating may result from the inconsistency of rating scores assigned by evaluator. For example, the evaluator assigned a score of 5 to experiment 2 that would have been rated a 4 on the experiment 1 at the same level of visual quality. Generally speaking, the correlations of $NDVI_{705}$ were higher than the corresponding correlations of $NDVI_{670}$ with visual quality rating, is sensitive to the change of chlorophyll content but less sensitive to biophysical factors, for instance, leaf orientation, status of the soil, optical properties and solar angle are comparatively poorer. The instable prediction performance of

indexes for visual quality evaluation is not only dependent on the selection of interested region and the choice of spectral region but also the species of samples.
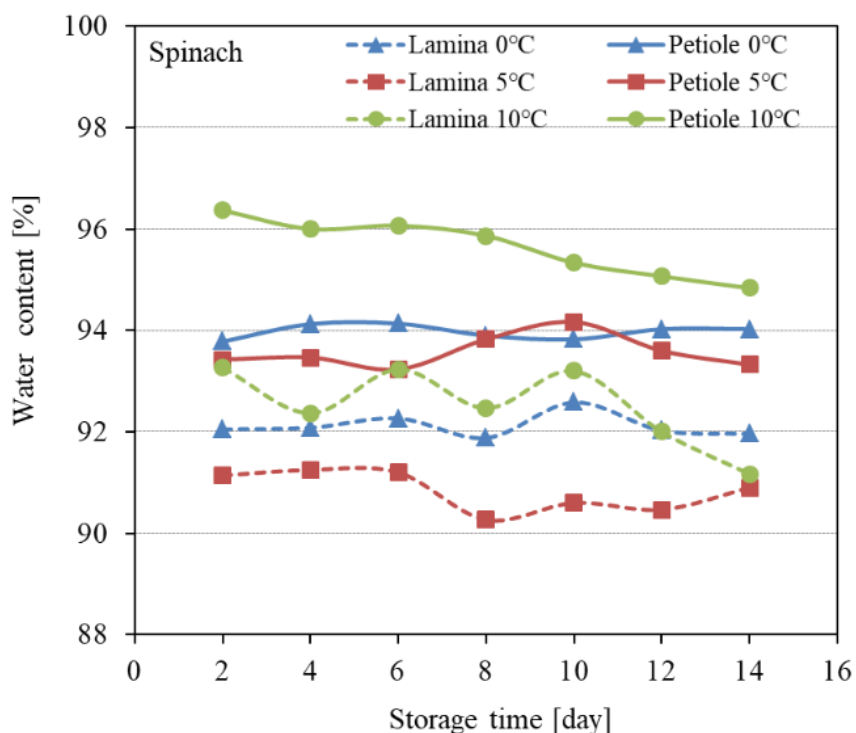
2.8 Water content

Figure 2-24. Water content change over storage time of spinach at various storage temperatures.

As shown in Figure 2-24 and 2-25, moisture content in petiole was higher than that in the blade regardless the type of vegetable analyzed. Differences could be noted on initial moisture contents not only between spinach and komatusna, but also between the same sample (same cultivar) that purchased at different times. Compared to storage at 0 °C and 5 °C spinach stored at 10 °C indicated a rapid decrease in moisture content. After 2 weeks storage, spinach stored at 10 °C reached a moisture loss of about 1.6 % and 2.1 % in petiole and blade respectively, while spinach held at 5 °C and 0 °C, the moisture loss was maintained at a constant level for the whole storage period. On the other hand, however, the moisture contents in komatsuna changed very little in all conditions during storage period.

Spinach was more susceptible to storage temperature than komatsuna with respect to moisture content.
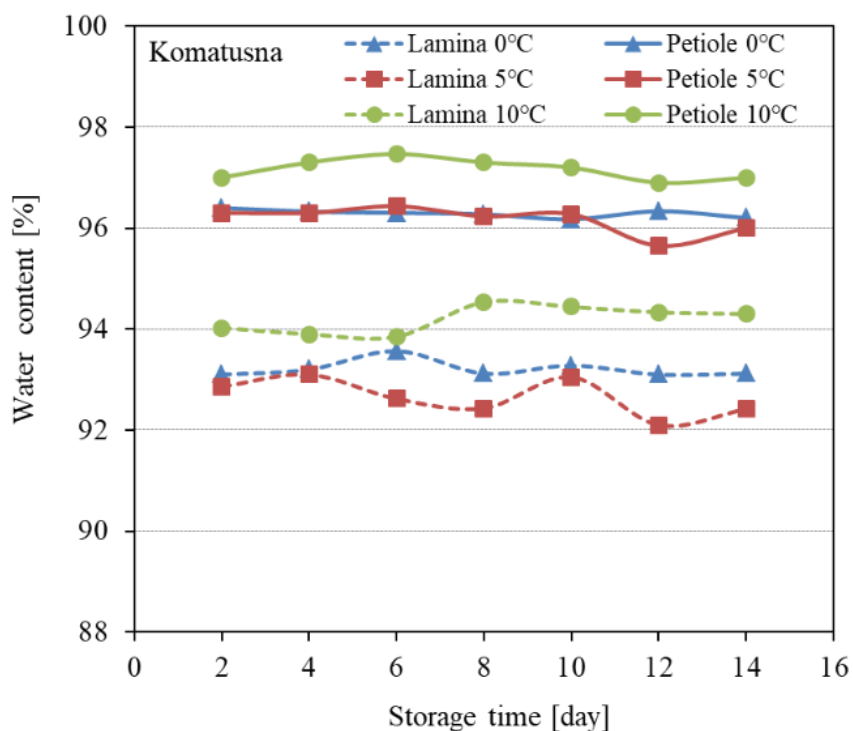

Figure 2-25. Water content change over storage time of komatsuna at various storage temperatures.

2.9 Total soluble solid

Figure 2-27 shows the effect of storage temperatures on total soluble solids in strawberries. Through the whole storage period, there were some fluctuations in the Birx values, but the final values were at a similar level to the first day when stored at 0 °C for both cultivars and at 5 °C for Yumenoka cultivar. However, it was observed that Birx value was decreasing in Benihoppe cultivar stored at 5 °C could be demonstrated by a higher respiratory rate than that at 0 °C. On the basis of above, besides storage temperature and storage period, cultivar is also a critical factor in affecting the shelf-life and post-harvest quality of strawberries.
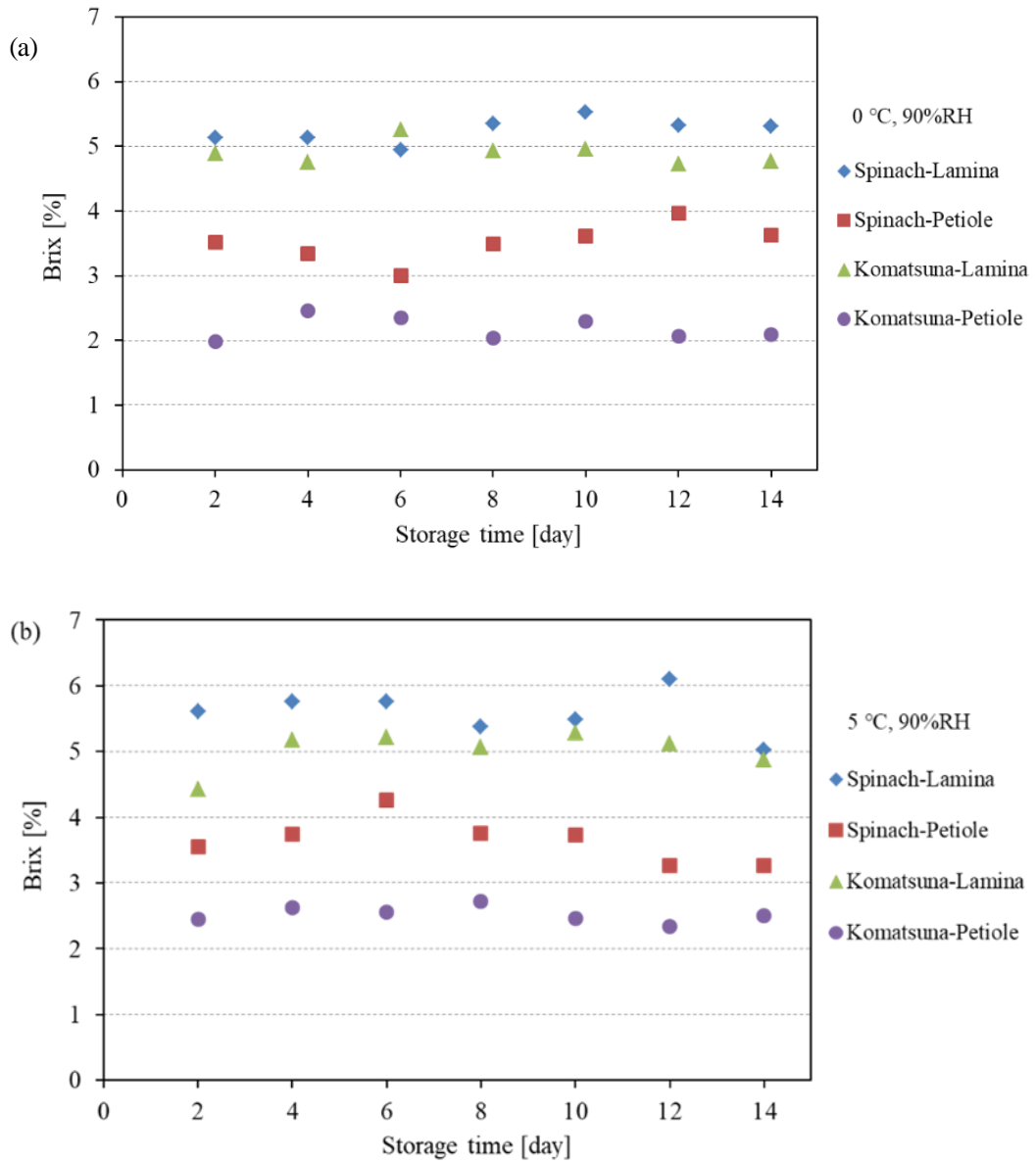
Figure 2-26. Total soluble solid change over storage time of spinach and komatsuna at storage temperature of: (a) 0 °C; (b) 5 °C.
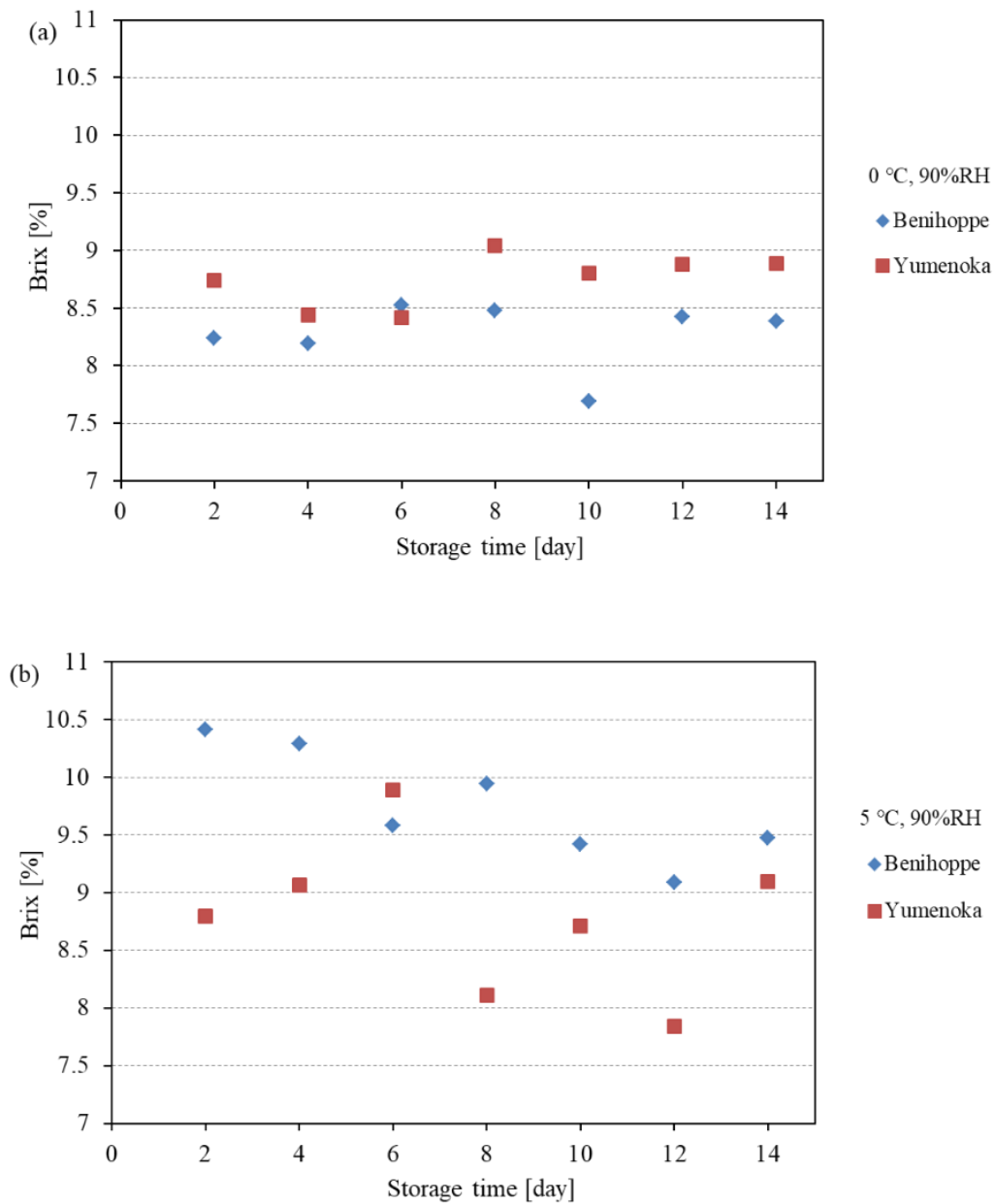
Figure 2-27. Total soluble solid change over storage time of spinach and komatsuna at storage temperature of: (a) 0 ℃; (b) 5 ℃.

According to the research of Kader, in order to satisfy flavor quality of strawberry a minimum Brix value of 7% is recommended [20]. Therefore, the two strawberries cultivars studied were adequate to achieve this market standard. During the storage period, no differences in Brix value among storage temperatures were observed in spinach and komatsuna, as shown in Figure 2-26.

2.10 Summary

The laboratory-based hyperspectral imaging system was established to investigate the chlorophyll distribution in three species of plants for evaluating visual quality. The major conclusions can be summarized as follows.

(1) The hyperspectral imaging is capable of identifying and mapping chlorophyll pigments and their changes in samples non-destructively.

(2) From the hyperspectral images we can acquire the spatially detailed information of chlorophyll distribution in different parts of the samples. After the acquisition of hyperspectral images and data processing, average spectral reflectance extracted from the interested region of sample leaves and calyxes were applied to develop prediction model.

(3) NDVIs as a function of the spectral reflectance at the regions of red (670 nm) and red edge (705 nm) were used to evaluate the visual quality change in samples studied. The changes of sample visual quality at different storage conditions were reasonably well evaluated by both the two indices. In contrast, there was a stronger correlation between $NDVI_{705}$ and visual quality rating than that between $NDVI_{670}$ and visual quality rating, indicating the superiority of spectral reflectance in red edge region for visual quality evaluation.

2.11 Reference

［1］   Jia L, Liu S, Duan X, Zhang C, Wu Z, Liu M, Guo S, Zuo J, Wang L. (2017) 6-Benzylaminopurine treatment maintains the quality of Chinese chive (Allium tuberosum Rottler ex Spreng.) by enhancing antioxidant enzyme activity, Journal of Integrative Agriculture, 16: 1968-1977

［2］   Ben-Yehoshua S, Rodov V, Bartz J, Brecht J. 2003. Transpiration and water stress. In: Postharvest Physiology and Pathology of Vegetables. Marcel Dekker, New York. pp. 111–159.

［3］　　　鮮度保持に関する試験方法·項目，北海道立総合研究機構·農業本部資料 (Local Independent Administrative Agency Hokkaido Research Organization). https://www.hro.or.jp/list/agricultural/research/hanayasai/04hana_yasai_info/02youryou/fresh/veg/yasai.pdf

［4］　　　Kim, D. R., C. W. Jeon and Y. S. Kwak (2015) Studies on Botrytis cinerea density in packing shed and gray mold incidence following storage-temperature in exported strawberry, The Korean Journal of Pesticide Science, 19: 295-300.

［5］　　　Merzlyak, M. N., Gitelson, A. A., Pogosyan, S. I., Chivkunova, O. B., Lehimena, L., Garson, M., ... & Rumyantseva, V. B. (1997). Reflectance spectra of leaves and fruits during their development and senescence and under stress. Russian Journal of Plant Physiology, 44(5), 614-622.

［6］　　　Li, C., Zhu, X., Wei, Y., Cao, S., Guo, X., Yu, X., & Chang, C. (2018). Estimating apple tree canopy chlorophyll content based on Sentinel-2A remote sensing imaging. Scientific reports, 8(1), 3756.

［7］　　　Bell, G. E., Howell, B. M., Johnson, G. V., Raun, W. R., Solie, J. B., & Stone, M. L. (2004). Optical sensing of turfgrass chlorophyll content and tissue nitrogen. HortScience, 39(5), 1130-1132.

［8］　　　Gitelson, A. A., & Merzlyak, M. N. (1997). Remote estimation of chlorophyll content in higher plant leaves. International Journal of Remote Sensing, 18(12), 2691-2697.

［9］　　　Filella, I., Serrano, L., Serra, J., & Penuelas, J. (1995). Evaluating wheat nitrogen status with canopy reflectance indices and discriminant analysis. Crop Science, 35(5), 1400-1405.

［10］　　　Adams, M. L., Norvell, W. A., Philpot, W. D., & Peverly, J. H. (2000). Spectral detection of micronutrient deficiency in 'Bragg'soybean. Agronomy Journal, 92(2), 261-268.

［11］　Wu, C., Niu, Z., Tang, Q., & Huang, W. (2008). Estimating chlorophyll content from hyperspectral vegetation indices: Modeling and validation. Agricultural and forest meteorology, 148(8-9), 1230-1241.

［12］　Cho, M. A., Skidmore, A. K., & Atzberger, C. (2008). Towards red-edge positions less sensitive to canopy biophysical parameters for leaf chlorophyll estimation using properties optique spectrales des feuilles (PROSPECT) and scattering by arbitrarily inclined leaves (SAILH) simulated data. International Journal of Remote Sensing, 29(8), 2241-2255.

［13］　Gamon, J. A., & Surfus, J. S. (1999). Assessing leaf pigment content and activity with a reflectometer. New Phytologist, 143(1), 105-117.

［14］　Delegido, J., Verrelst, J., Alonso, L., & Moreno, J. (2011). Evaluation of sentinel-2 red-edge bands for empirical estimation of green LAI and chlorophyll content. Sensors, 11(7), 7063-7081.

［15］　Peng, Y., Nguy-Robertson, A., Arkebauer, T., & Gitelson, A. A. (2017). Assessment of canopy chlorophyll content retrieval in maize and soybean: Implications of hysteresis on the development of generic algorithms. Remote Sensing, 9(3), 226.

［16］　Gitelson, A. A., & Merzlyak, M. N. (1996). Signature analysis of leaf reflectance spectra: algorithm development for remote sensing of chlorophyll. Journal of plant physiology, 148(3-4), 494-500.

［17］　Kanke, Y., Raun, W., Solie, J., Stone, M., & Taylor, R. (2012). Red edge as a potential index for detecting differences in plant nitrogen status in winter wheat. Journal of plant nutrition, 35(10), 1526-1541.

［18］　Shafri, H.Z.M., Salleh, M.A.M., & Ghiyamat, A., 2006. Hyperspectral remote sensing of vegetation using red edge position techniques. American Journal of Applied Science, 3(6), 1864-1871.

［19］　　Bremer, D. J., Lee, H., Su, K., & Keeley, S. J. (2011). Relationships between normalized difference vegetation index and visual quality in cool-season turfgrass: I. Variation among species and cultivars. Crop science, 51(5), 2212-2218.

［20］　　Kader, A.A. (1999). Fruit maturity, ripening, and quality relationships. Acta Hortic. 485, 203-208

Chapter 3. Application of NH$_3$ adsorption for low carbon refrigerated transport system

The natural refrigerants like water, ammonia, methanol, and ethanol are commonly used in adsorption refrigeration systems. Due to its high latent heat of evaporation (2258 kJ/kg), water is the most frequently employed refrigerant and often used with silica-gel or zeolite. However, its low vapor pressure and freezing point are the dominant constraints on the application, such as ice making or food storage. Although the latent heat of evaporations of methanol, ethanol, and ammonia (1100 kJ/kg, 838 kJ/kg and 1368 kJ/kg, respectively) are inferior to water, they can be applied to produce sub-zero temperatures on account of their low melting points. Methanol will have decomposition problems when the driving temperatures are higher than 120 ℃ [1], while ammonia can remain stable at least 200℃. This makes it applicable to a wider range of driving temperature, such as the waste heat from the gas turbine of a CHP system or the diesel engine of a fishing boat. Despite ammonia is toxic and its corrosivity prohibits the use of copper, the distinctive pungent odor will make it possible to be detected immediately if leakage happened. Unlike the other three refrigerants that operate at subatmospheric pressure, the high working pressure of ammonia leads to a good mass transfer performance.

Due to the high ability of mass transfer and stable adsorption capacity, activated carbon (AC) is the most commonly used physical adsorbent for ammonia [2-5]. However, the large internal surface area results in poor thermal conductivity. On the other hand, alkaline-earth metal chlorides, such as CaCl$_2$ [6], SrCl$_2$ [7], BaCl$_2$ [8], are often used as chemical adsorbents for ammonia owing to they have higher adsorption capacity than physical adsorbents, but the swelling and agglomeration behaviors also make them poor heat and mass transfer performance, and the higher driving temperatures are needed in comparison with physical adsorbents. With the purpose of solving the above problems, numerous investigations related to composite adsorbents have been conducted recently. Up to now, the most common type of chemical adsorbent that used to synthesize composite adsorbents is CaCl$_2$, combined with a porous matrix such as alumina [9], vermiculite [9], activated carbon [10, 11], activated carbon fibre [12], expanded graphite [13], CaSO$_4$ [14].

Results of these researches shown that higher system performances could be achieved by the use of composite adsorbents as the enhancement of heat and mass transfer. The composite adsorbent can also be composed of a physical adsorbent and a porous matrix. Wang et al. [15] presented a composite consolidated adsorbent that consisted of a granular activated carbon and an expanded natural graphite which was treated with sulfuric acid. They obtained a maximum effective thermal conductivity of 34.2 $Wm^{-1}K^{-1}$ which was 150 times larger than that of granular AC. Moreover, the equilibrium adsorption capacity of composite adsorbent didn't change with the addition of porous matrix and had a better desorption performance in comparison with the granular AC.

In order to effectively utilize the exhaust heat from the food storage system, an activated carbon-NH_3 adsorption refrigeration system with high ability and long durability is proposed. The specific surface area, pore size distribution and morphological structure of the activated carbons have been characterized by N_2 adsorption, SEM, and XRD. The adsorption capacities of four kinds of activated carbons were compared based on adsorption isotherms at 30 °C. The performance of NH_3 refrigeration system at various evaporating temperatures and cycle times were experimentally investigated.

3.1 Activated carbon-ammonia adsorption refrigeration system

3.1.1 Characterization of adsorbent

The selection of appropriate adsorbent is indispensable for an adsorption refrigeration system, and the following factors must be taken into account while selecting adsorbent: high adsorption/desorption capacity, low specific heat, excellent thermal conductivity, compatible with refrigerant, noncorrosive and cost effective, etc. [16].

The commonly used physical adsorbents for adsorption refrigeration are silica gel, zeolite, and activated carbon. Compare to silica gel and zeolite, activated carbon has high pore volume and large surface area available for adsorption, and is available in many forms, such as powders, granular, carbon-foam, molecular sieves or fiber, etc. Several activated carbons, as furnished in Table 3-1, have been applied in this research. The specific surface area and pore size distribution of adsorbents have been studied. SEM and XRD have also

been employed for an accurate description of the microstructure and morphological structure of the adsorbents.

Table 3-1. Details of activated carbons

Carbon name	Manufacturer	Starting material	Physical form
BA	Ajinomoto Fine-Techno Co., Inc.	wood-based materials	Powder
GA-H	Cataler Corporation	Organic wastes	Granule
PG-H	Cataler Corporation	N/A	Pellet
MSC-30	KansaiCoke and Chemicals Co., Ltd	Petroleum coke	Powder
BAC	Kureha Corporation	Phyllostachys heterocycla	Granule
CNTs	GIEC, China	N/A	Powder

3.1.2 BET and PSD

The specific surface areas and pore size distributions were measured by N_2 adsorption at 77K, using an automatic adsorption system (ASIQMO002-2, Quantachrome). The samples were degassed at 150 °C for 24 hours to remove surface impurities before the measurements of N_2 adsorption isotherms in the relative pressure range between 10^{-3} and 0.2.

The pore size distributions were calculated by non-local density functional theory model. As indicated in Figure 3-1 and Table 3-2, sample ②~⑤ were mainly microporous, particularly, sample ⑤ contained more than 95% micropores, with the average pore diameter of 0.52~1.48 nm. However, there were almost no micropores in sample ⑥, which

was found to be the most mesoporous, with the mean pore diameter of 36 nm and exhibited the lowest BET surface area of among the samples.

Sample ① had a BET surface area of 3037 m^2/g, was much higher than the other samples, and a large porous volume of 1.49 ml/g, showing the possibility of high adsorption of ammonia. Moreover, sample ① displayed a broad pore size distribution in the range of 0.5~4 nm, which indicated the existence of micropores and narrow mesopores (2~4 nm), but the micropore volume was only 56.4% due to the presence of massive narrow mesopores.

Table 3-2. Specification of activated carbons.

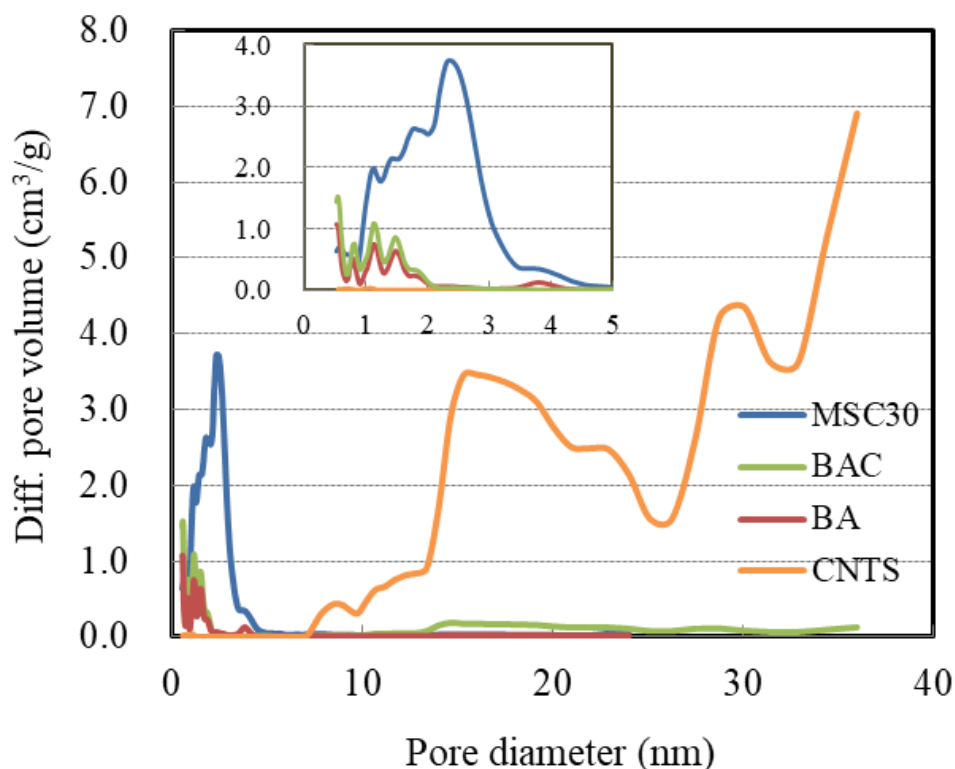| Sample	BET surface area [m^2/g]	Porous Volume [ml/g]	Micropore Volume (%)	Mesopore Volume (%)	Average Pore Diameter [nm]
①MSC30	3037	1.49	56.4	43.6	2.31
②BAC	1231	0.53	88.7	11.3	0.55
③BA	768	0.31	91.2	8.8	0.52
④GA-H	848	0.33	95.1	4.9	0.55
⑤PG-H	630	0.30	74.9	25.1	1.48
⑥CNTs	202	1.47	0.8	99.2	36.00

Figure 3-1. Pore size distributions of activated carbons

3.1.3 SEM of materials

Field Emission Scanning Electron Microscope (JSM-6335F, JEOL Ltd.), giving a resolution of 1.5 mm at 15 kv and 5 nm at 1kv, was used to characterize the morphological structures of the samples. Observations were carried out at ×35 and ×1000 magnifications. SEM images of activated carbons are shown in Figure 3-2.

BACs were highly spherical particles, ranged from 50 ~ 250 μm in size, with a few cracks or visible pore developments appear on the surface, as shown in Figure 3-2 (a). In contrast, the SEM images of the other samples were characterized by heterogeneous structures, demonstrating the presence of irregularly shaped particles with different sizes. The average particle size of BA, GA-H, PG-H, and MSC was about 200, 400, 300, and 90 μm, respectively. Small size particles agglomerations dispersed on large particles can be found in some regions of BA, GA-H, and PG-H.

From the high magnification SEM images, it can be seen clearly that some voids of different sizes were distributed randomly at the surface of MSC30, indicating relatively high specific surface area and a better diffusion of adsorbates than the other samples. This is consistent with the observation from BET.
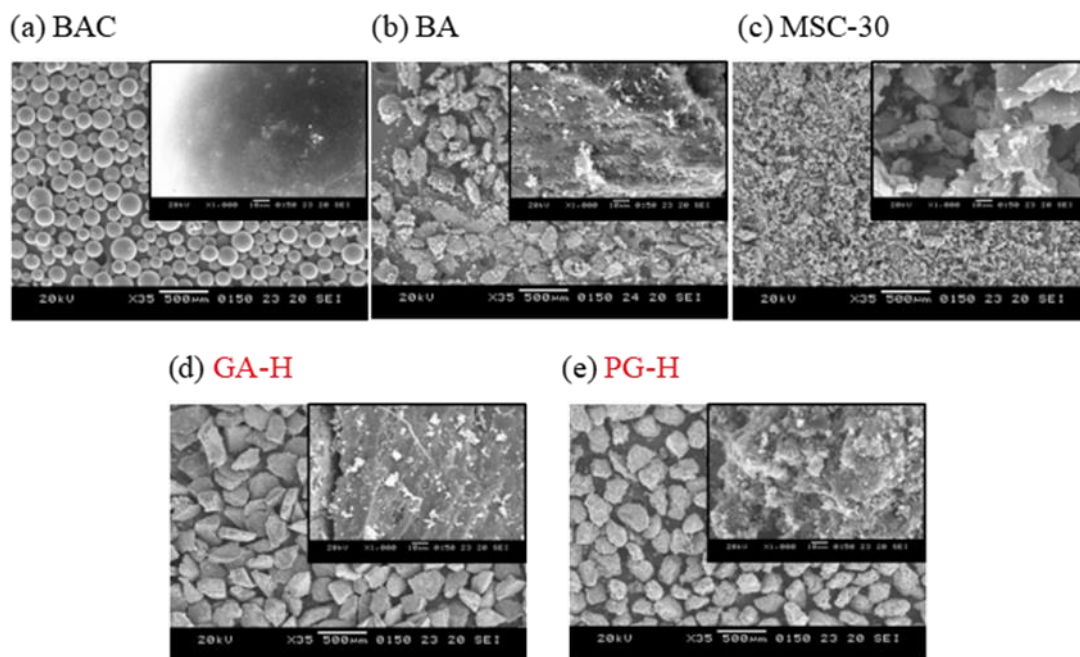

Figure 3-2. SEM images of activated carbons.

3.1.4 XRD of materials

XRD was performed for structural identification of the AC on an ESCALAB-210 spectrometer (VG Scientific Ltd.), using AlKα radiation source at 40 kV and 40 mA. The scan speed was 2°/min with a process size of 0.02 across a range of 20° to 80°. As shown in Figure 3-3, the activated carbons except for MSC30 exhibited two peaks around 2θ value 26° and 44°, which correspond to the diffraction of (002) and (100)/(101) plane of the graphitic structure, respectively. The broad asymmetric peak at 26° indicated that the ACs were amorphous and had a disordered graphitic structure in common. The disappearance of the peak at 26° in MSC30, implying that a more disordered graphitic structure than the others and this was greatly related to the substantial increase in the specific surface area according to [17].
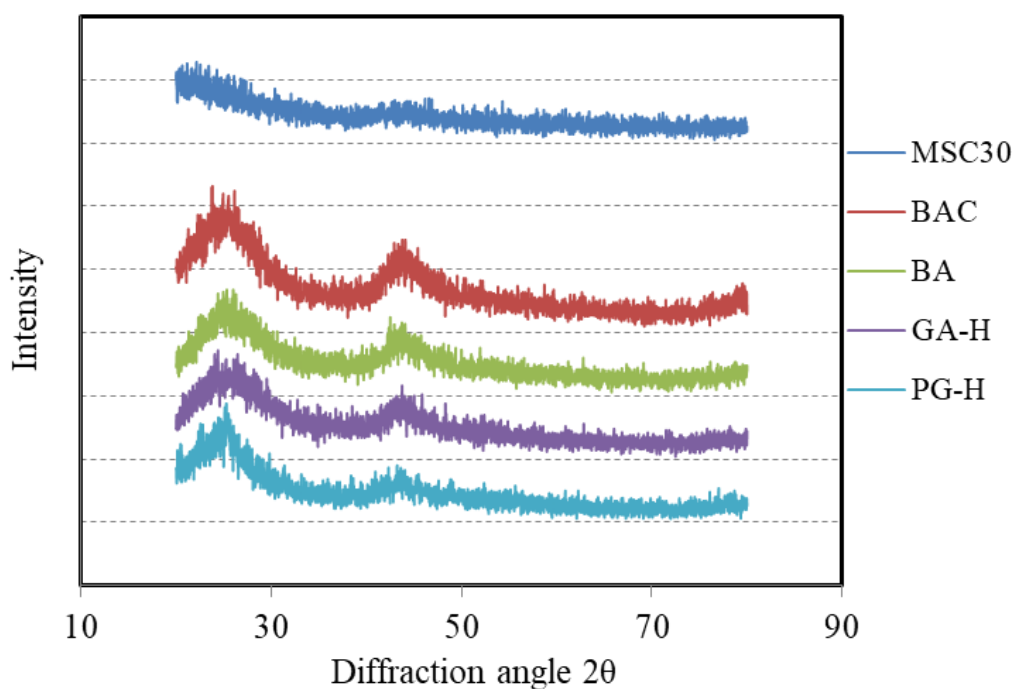
Figure 3-3. XRD patterns of activated carbons.

3.1.5 Experimental apparatus of adsorption isotherm

A schematic diagram of volumetric gas adsorption apparatus is shown in Figure 3-4. The apparatus is mainly composed of three parts: Gas supply system, adsorption system, and gas scrubber system. NH_3 with a purity of 99.9998% (Taiyo Nippon Sanso, the Gas Professionals Co. Lt.) and N_2 gas with a purity of 99.9998% (Taiyo Nippon Sanso the Gas Professionals Co. Lt.) are supplied by the compressed gas tank. The flows of the two gases are regulated and controlled by commercial mass flow controllers. N_2 gas is used to calibrate the system volume and remove the residual ammonia gas in the system. Gas supply system, adsorption system, and gas scrubber system are connected by 316 L stainless tube as shown in Figure 3-4.

The adsorption system mainly includes sample cell, reference cell, a set of actuated valves (Swagelok DP series), filter and a pressure transducer. The sample cell has an inner volume of 58 ml. A filter（Swagelok SS-4F-2, element nominal pore size: 0.5 μm）is installed right above the sample cell to prevent activated carbon particles from flying out of

70

the sample cell while executing adsorption/desorption and vacuum processes. The volume enclosed by V3, V4, V5, V6, pressure transducer (Swagelok PTU-S series, 6 MPa max, accuracy: ≤ 0.5 % of span) and thermometer (Asone TPT-16150L), is defined as reference volume with a size of 197 ml.
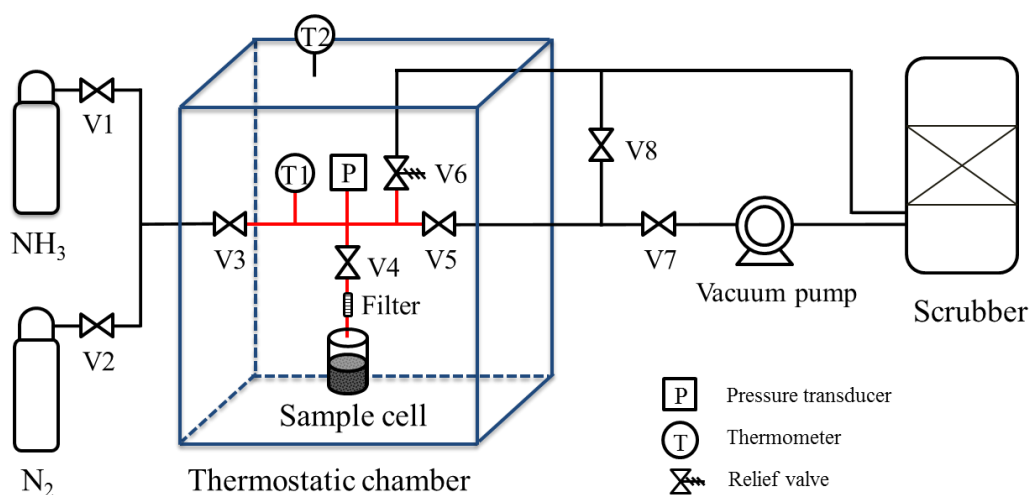

Figure 3-4. Schematic diagram of the adsorption isotherm apparatus.

In order to keep this system at the desired temperature, the sample cell and reference cell are located in a thermostatic chamber, and temperature is controlled via the thermostatic water bath (Eyela NCC-2100, with ± 0.1 °C~0.2 °C accuracy of the set point) and is monitored with a platinum resistance thermometer (Asone TPT-16150L) placed at the center of the chamber. The vacuum pump (Asada, Y93539, ultimate pressure 2.0 Pa [abs]) is connected to the system by a flexible stainless steel hose to V7. All the pressure and temperature devices are connected to the data logger (Keysight 34970A) to monitor and record the results continuously. Due to the corrosivity and toxicity of ammonia, a gas scrubber is used to prevent ammonia leakage accident by providing immediate removal of leaking ammonia.

3.1.6 Experimental procedures of adsorption isotherm

All samples were placed in an electric furnace (V) at 120 °C for 24 hours to dry before the experiments of adsorption measuring procedure. Electronic balance (Mettler Toledo AG204, with a minimum display of 0.1 mg) is used to gauge the mass of samples. 0.5 g of

dried sample was transferred to the sample cell and then the temperature of the thermostatic chamber was set at 80 °C by using hot water circulation. The whole system was evacuated by the vacuum pump at 80 °C for 5 hours to remove the residual gases from the samples wholly. To minimize the risk of sample particles flying out of the sample cell, the pressure of the sample cell was decreased from atmospheric pressure to 1 Pa step by step, with an interval of about 10 kPa.

After finishing the vacuum process, V7 was closed to isolate the vacuum pump and the temperature of the thermostatic chamber was set at 30 °C. As the system temperature reached 30 °C, all the opened valves were closed. Adjusted the NH_3 pressure through the gas cylinder pressure regulator and then opened V1, V3 to allow the NH_3 gas flow into the reference cell. Closed V3 and wait until the temperature of the NH_3 in reference cell reached the adsorption temperature 30 °C, monitored by thermometer T1. The initial pressure in the reference cell was recorded as P_0. V4 was opened slightly allowing NH_3 gas in the reference cell to flow into the sample cell, and then the NH_3 gas began to adsorb on the surface of the samples partly. The adsorption process was run for 2 hours until it reached the thermodynamic equilibrium state. The equilibrium pressure P1 recorded by data logger was used as a basis to calculate the adsorption capacity. Closed V4 and then repeated the above operations at different initial pressures and equilibrium pressures to achieve an adsorption isotherm at 30 °C. To ensure reliable and repeatable experimental results, each sample was tested at least twice with a fresh batch of the sample.

3.1.7 Experimental apparatus of system performance

The experiments to investigate the cooling performance of the MSC30-NH_3 pair at different evaporating temperatures and cycle times were conducted in the experimental apparatus is illustrated in Figure 3-5. This system mainly comprised of an evaporator/condenser (plate type heat exchanger) and an adsorber/desorber (with a finned tubes heat exchanger), both of them were thermally insulated by glass wool to minimize heat dissipation. The temperatures of these instruments were regulated and controlled by thermostatic water baths. And the inlet and outlet temperatures of evaporator/condenser and adsorber/desorber were measured by the platinum resistance thermometers. The system

pressures were measured through pressure transducers (Swagelok S Model, with an accuracy of ≤ 0.5 % LPC). The flow sensors (Keyence FD-SS2A, ± 1% of F.S) and needle valves were applied to measure and adjust the flow rate of the heat transfer fluid, respectively. The influence of evaporating temperature and cycle time on the system performances were investigated, while the temperature of condenser and desorber were fixed at 30°Cand 80°C, respectively. The adsorber has a dimension of 347 mm (length) × 142 mm (width) × 34 mm (height), with a volume of 1.68 L.
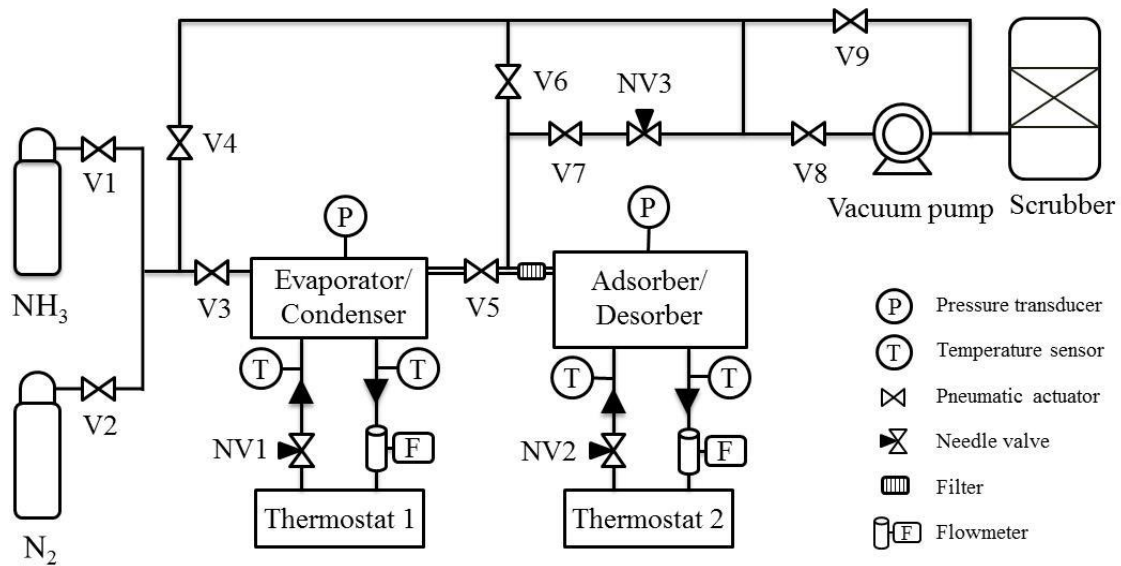
Figure 3-5. Schematic diagram of the system cooling performance apparatus.

3.1.8 Experimental procedures of cooling performance

The adsorber was packed with 66 g MSC30, which had been desiccating in the electric furnace at 120 °C for 24 hours. The adsorbent was overlaid with a stainless steel mesh to avoid adsorbent powders frying out of the adsorbent bed.

For leak detection, opened V2, V4, V5 and V7, adjusted NV3 to control the flow of N_2 into the system until the system pressure up to 1.5 MPa, then closed V2 and monitored the system pressure by data logger for one day. After the leak detection, V9 was opened to remove N_2 from the system. When the system decreased to atmospheric pressure, opened all valves except V9, the whole system was evacuated by operating the vacuum pump for 24 hours and the adsorber was simultaneously heated by the thermostatic water bath 2 at

80 °C. Closed V8 to isolate the system from the vacuum pump and waited 12 hours to make sure that no leak occurred. Meanwhile, set the thermostatic water bath 2 to 30 °C to cool down the adsorbent bed. Opened V1 and V3 while the other valves were closed, charged a certain amount of NH_3 into the evaporator whose temperature was controlled by the thermostatic water bath 1 at 5 °C. Closed V1, V3 and opened V5 to allow NH_3 vapor to transfer from evaporator to adsorber. Liquid NH_3 started to evaporate in the evaporator by absorbing heat from the circulating chilled water, and thus cooling effect was achieved. NH_3 vapor was adsorbed in adsorber, and the heat of adsorption was extracted by 30 °C cooling water which was circulated through thermostatic water bath 2.

After the adsorption process had continued for a particular time (cycle time), V5 was closed, and the temperature of evaporator and adsorber were adjusted to 30 °C and 80 °C respectively. Six different cycle times were investigated in this study. When both of the condenser and desorber pressure reached to the condensing pressure, opened V5 for the desorption process. The desorbed NH_3 gas flowed into the condenser and then was condensed. The cycle time of desorption process was the same as adsorption process. Once the desorption process finished, closed V5 and set the temperature of condenser and desorber to 5 °C and 30 °C respectively. The sensible heat of the adsorber was removed by the cooling water. The experimental conditions are summarized in Table 3-3.

Table 3-3. Experimental Conditions

Evaporating temperature (T_L)	5°C, 10°C,15°C
Adsorption/Condensing temperature (T_M)	30°C
Desorption temperature (T_H)	80°C
Flow rate in the evaporator/condenser	1.5L/min
Flow rate in the adsorber/desorber	0.6L/min

Adsorption/Desorption cycle time	300s, 360s, 420s, 480s, 540s, 600s
Cycle preparation time	150s

After the pressure of evaporator and adsorber reduced to the evaporating pressure, adsorption process was conducted by opening V5 and repeated the operation as mentioned above for the next condition. The COP, SCP, and VCP were calculated by the following equations:

$$COP = \frac{Q_c}{Q_s + Q_{des}}$$

(3-1)

$$SCP = \left(\frac{\Delta q}{\tau_{cycle} + \tau_{pre}} \right) \Delta H_{eva}$$

(3-2)

$$VCP = \left(\frac{\Delta q}{\tau_{cycle} + \tau_{pre}} \right) \left(\frac{W}{V} \right) \Delta H_{eva}$$

(3-3)

where Q_c is the cooling heat (kJ), Q_s is the sensible heat (kJ), Q_{des} is the desorption heat (kJ), Δq is the amount adsorbed (kg-adsorbate/kg-adsorbent), τ_{cycle} is the cycle time (s), τ_{pre} is the preparation time (s), m is the mass of adsorbent (kg), V is the volume of heat exchanger (m^3).

3.1.9 Adsorption isothermal of activated-carbon

Four kinds of activated-carbon (MSC30, BAC, BA, and CNST) were applied to measure the NH_3 adsorption isotherms at 30 °C, and the results are shown in Figure 3-6. The adsorption of the NH_3 on the activated carbons increases with the relative pressure as a consequence of the existence of the more NH_3 molecules, or in another word, the NH_3 gas diffusion rate is enhanced by increasing the pressure. The isotherm shape of MSC30, BAC and BA are similar in general, concave to the relative pressure axis. MSC30 shows a steep uptake up to the relative pressure of about 0.5, revealing that the presence of a broader pore size distribution which including wider micropores and narrow mesopores [18]. Howbeit

75

CNST illustrates a convex curve to the relative pressure axis, which is attributed to its non-microporous property. The adsorption capacity of these four kinds of activated carbons is MSC30 > BAC > BA > CNST at the relative pressure of 0.7, which is strongly related to the specific surface area and the pore volume as summarized in Table 3-2. Moreover, it is evident that the hysteresis of MSC30 isotherm is minimal.
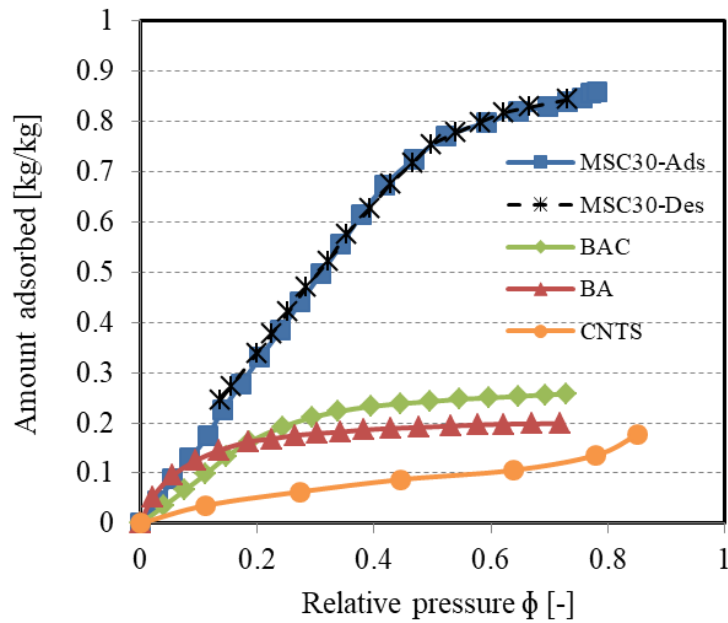

Figure 3-6. Adsorption isotherms of NH_3 on the various activate carbons (30°C).
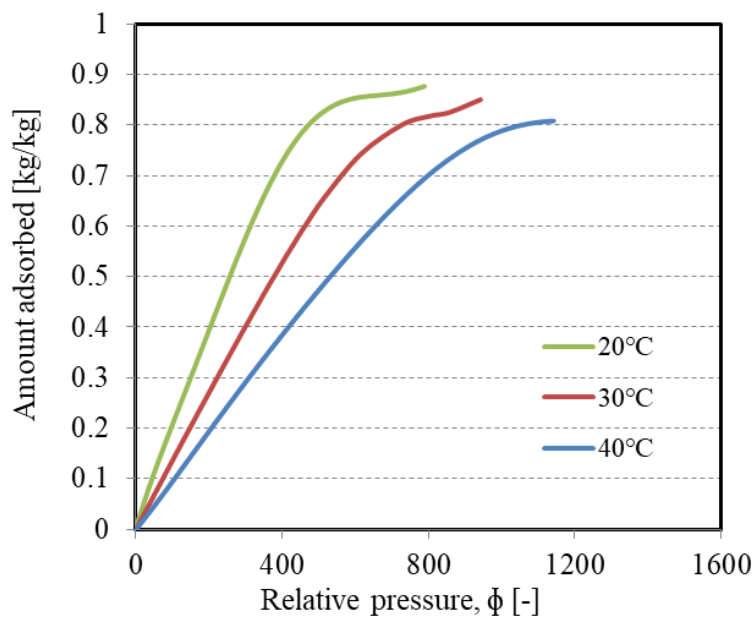
Figure 3-7. Adsorption isotherms of NH_3 on MSC30 at different temperatures.

Due to the excellent adsorption/desorption capacity of NH_3, MSC30 is selected for further studies in this paper. The experimental results of NH_3 adsorption on MSC30 at the temperature of 20, 30 and 40 °C are presented in Figure 3-7. It shows that the amount adsorbed is higher at lower temperatures under the same equilibrium pressure because the NH_3 vapor molecules have much higher internal energy at high temperatures.

3.1.10 Adsorption isotherm model of activated-carbon

The analysis of experimental isotherm results is necessary to establish equation which can describe the results precisely. There are several empirical adsorption isotherms models defined to characterize the experimental data. The most frequently employed models are Langmuir [19-21], Freundlich [19, 20], BET [22], Dubinin-Raduskevich [21, 23], and Dubinin-Astakhov [23, 24].

In this work, the modified Dubinin-Astakhov equation was adopted to evaluate the experimental results. The modified Dubinin-Astakhov equation is given as [25]:

$$q = q_0 \exp\left[-k\left(\frac{T}{T_{sat}}-1\right)^n\right]$$

(3-4)

where q represents the amount adsorbed (kg/kg), q_o is the maximum amount adsorbed (kg/kg), T is the adsorption temperature (K), T_{sat} is the saturation temperature of refrigerant (K), n and k are coefficients. Equation x can be linearly rewritten in the following form with a logarithmic operation.

$$\ln\left[\ln\left(\frac{q_0}{q}\right)\right] = \ln k + n \ln\left(\frac{T}{T_{sat}}-1\right)$$

(3-5)

The coefficients of the equation were obtained by the intercept and slope of the linear plot of $\ln[\ln(q_0/q)]$ against $\ln(T/T_{sat}-1)$. Besides, the coefficient of determination (R^2) and the standard error of estimate (SEE) were applied to assess the agreement between the predicted values and experimental results. R^2 demonstrates the proportion of variation in y (dependent variable) that is interpreted by x (independent variable), and can be expressed by the following equation [26]:

$$R^2 = \frac{\sum\limits_{i=1}^{n}(\widehat{y}_i - \overline{y})^2}{\sum\limits_{i=1}^{n}(y_i - \overline{y})^2}$$

(3-6)

where y_i is the ith experimental value, $\widehat{y}_i$ is the predicted value, $\overline{y}$ is the mean value of y, the numerator represents the regression sum of squares, and the denominator refers to the total sum of squares. The standard error of estimate (SEE) is an indicator of the accuracy of predicted values, given as:

$$SEE = \sqrt{\frac{\sum\limits_{i=1}^{n}(y_i - \widehat{y}_i)^2}{n-2}}$$

(3-7)

where n-2 represents the degrees of freedom, is calculated by subtracting the number of parameters in the equation with the number of experimental result points.
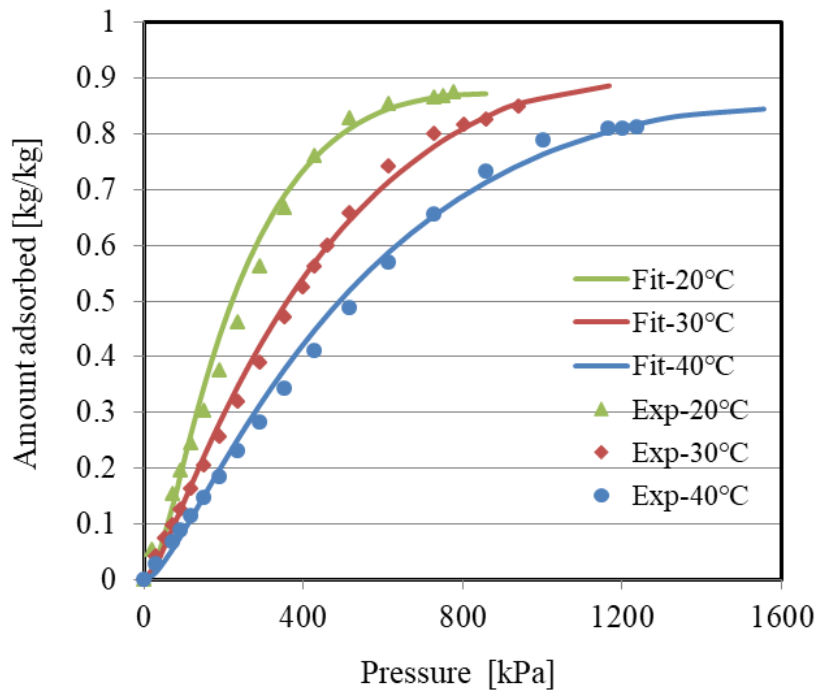
Figure 3-8. Comparisons between the experimental isotherms and the isotherms calculated by the modified Dubinin-Astakhov equation.

Figure 3-8 exhibits the fitting results of the modified Dubinin-Astakhov equation for MSC30-NH$_3$ at adsorption temperatures of 293K, 303K, and 313K. It is clear that the calculated values have good agreement with the experimental values. Table 3-4 includes the parameters achieved by equation (4) and the values of R^2 and SEE for MSC30-NH$_3$ at different adsorption temperatures.

Table 3-4. Characteristic parameter values of Equation (4)

	Adsorption temperature		
	20 °C	30 °C	40 °C
q$_0$ [kg/kg]	0.874	0.887	0.845
k	31.31	16.01	17.32
n	2.07	1.63	1.72
R^2	0.9874	0.9937	0.9910
SEE	0.0376	0.0179	0.0217

The constant n gives an estimation of the heterogeneous degree of the adsorbent surface and can be used as an empirical indicator of pore size distribution of adsorbent. It is observed that, in general, for adsorbents with narrow micropore size distribution, such as molecular sieve carbons, n is around 3; for adsorbents whose micropore size distributions are broad, like activated carbons, n is smaller than 3 (varies from 1.2 ~ 1.8 for strongly activated carbon with heterogeneous micropores); for adsorbents having exceptionally narrow micropore size distribution, like zeolites, n lies between 3 ~6 [27]. The n values obtained in this work were 1.63 ~ 2.07, indicating that MSC30 has a broad micropore size distribution and is regarded as a heterogeneous adsorbent. These conclusions are in accord with the findings obtained in material characterization. According to the R^2 and SEE, it can be inferred that the modified Dubinin-Astakhov equation can describe the adsorption behavior of MSC30-NH$_3$ pair accurately.

3.2 Isosteric heat of MSC30 NH_3 adsorption

Isosteric heat of adsorption (ΔH_{ads}), as one of the critical kinetic study parameters, is an indicator of the interaction strength between the adsorbate and the adsorbent. The Clausius-Clapeyron equation is commonly employed to calculate the ΔH_{ads}, and can be written as:

$$\ln\left(\frac{p_1}{p_2}\right) = -\frac{\Delta H_{ads}}{R}\left(\frac{1}{T_1} - \frac{1}{T_2}\right)$$

(3-8)

where R is the universal gas constant; P_1 and P_2 are the equilibrium adsorption pressures corresponding to the adsorption temperatures of T_1 and T_2 at the same amount adsorbed, respectively. The ΔH_{ads} was computed from the experimentally obtained isotherms at 20 °C and 30 °C, and the result is shown in Figure 3-9.
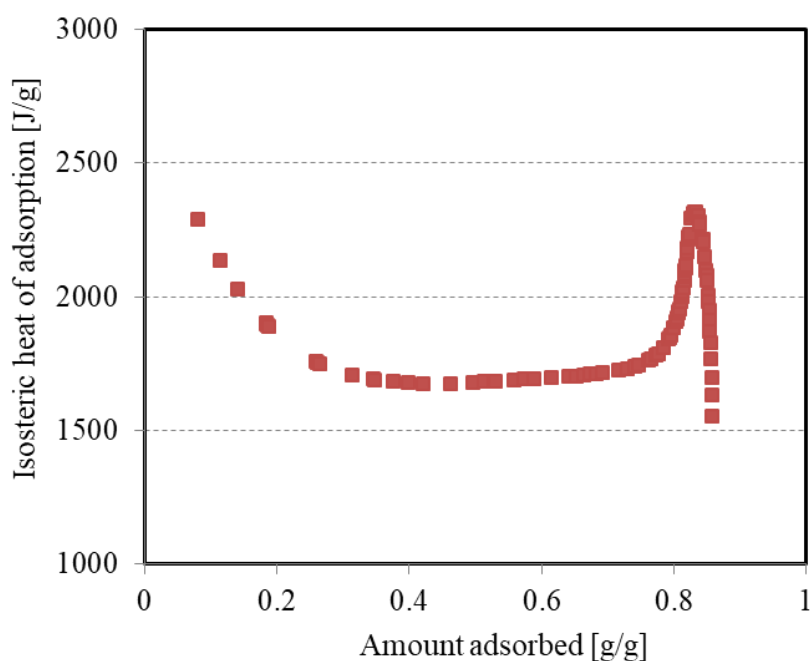
Figure 3-9. Dependence of the isosteric heat of adsorption on the amount adsorbed.

It is apparent that the isosteric heat of adsorption declined rapidly at the initial stage of adsorption (< 0.25 g/g) followed by a gentle change (0.25 g/g ~ 0.7g/g) with increasing the amount adsorbed, indicating that the surface of MSC30 is energetically heterogeneous by reason of the existence of different energetic adsorption sites. Higher ΔH_{ads} values at the

low amount adsorbed demonstrated stronger interactions of NH_3 with some high energetic adsorption sites existed on the surface of MSC30. However, there was a marked increase in the high amount adsorbed region (0.83 g/g ~0.85 g/g), which may be attributed to the presence of strong lateral interactions between the adsorbed NH_3 molecules [28, 29]. The ΔH_{ads} obtained in this study was in the range from 1552 to 2317 kJ/kg, with an average value of 1922 kJ/kg which was a little smaller than those reported in [30] (2000 ~ 2700 kJ/kg.).

3.3 Cooling performance of MSC30-NH_3 adsorption system

Figure 3-10 presents the influence of cycle time on COP at various evaporating temperatures. It is observed that the COP apparently profited from high evaporating temperature. The maximum COP obtained at 5, 10 and 15 °C were 0.24, 0.31, and 0.35 respectively. However, as the cycle time increased, the growth of COP at low evaporating temperature was more conspicuous than that at high evaporating temperature. This is because the adsorption rate decreased with the increase of adsorption ratio, which is the ratio of the amount adsorbed to the equilibrium adsorption capacity (can also be regarded as the degree of adsorbent saturation), as illustrated in Figure 3-11. The decline of adsorption rate resulted in the decreased in the cooling effect.
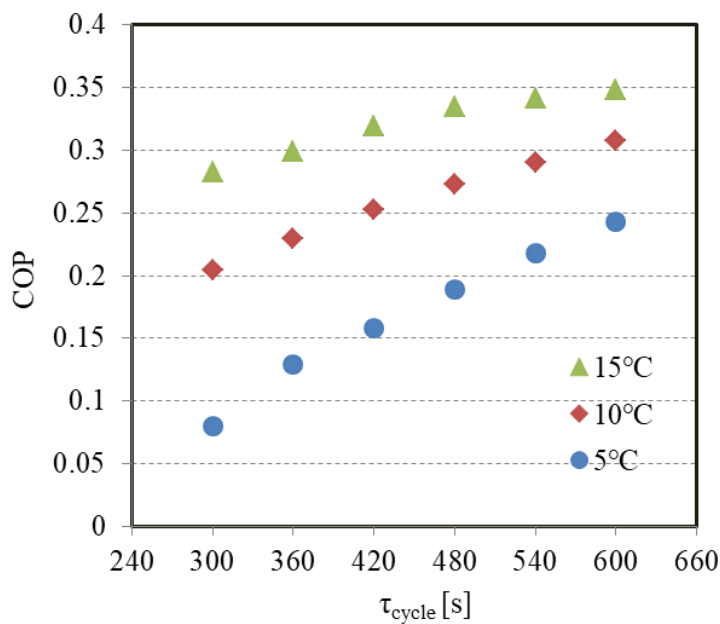
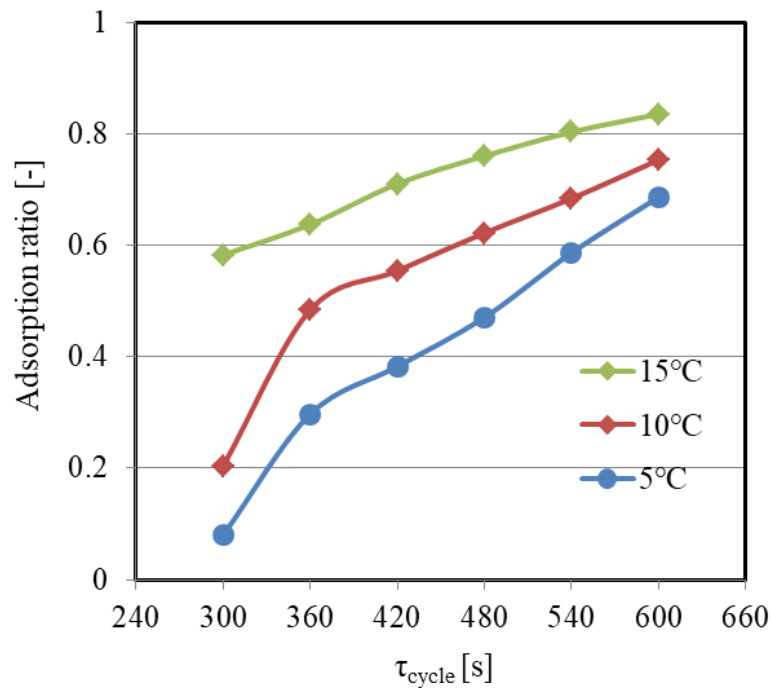**Figure 3-10.** The influence of cycle time on COP at various evaporating temperatures.

Figure 3-11. The adsorption ratio against cycle time at different evaporating temperatures.
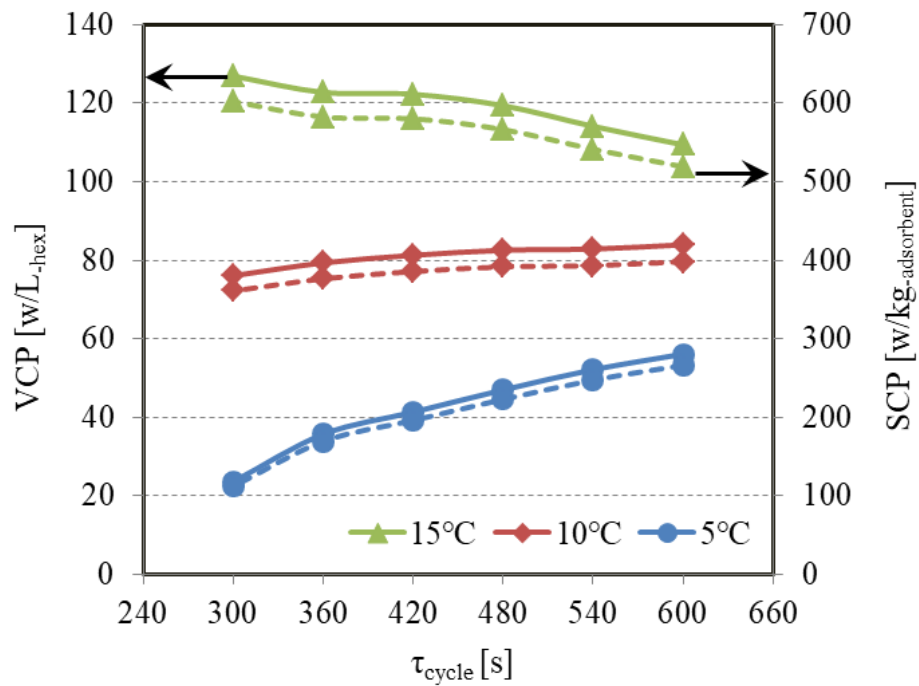

Figure 3-12. The variation in VCP and SCP versus cycle time at different evaporating temperatures.

Figure 3-12 shows the variation in VCP and SCP versus cycle time at different evaporating temperatures. The two measurements of VCP and SCP were directly proportional to one another and increased with increasing evaporating temperature. The VCP increased from 23.6 to126.9 W/L-heat exchanger, approximately 5.4 times enhancement, when evaporating temperature increased from 5 °C to 15 °C at the cycle time of 300 s; whereas, SCP rose from 112.1 to 602.3 W/kg-absorbent. However, with the increase in cycle time, the influence of evaporating temperature on the VCP and SCP decreased. As can be seen from Figure 3-12, the VCP and SCP increased with the cycle time when the evaporating temperature at 5 and 10 °C, while decreased at 15 °C. This can also be explained by the adsorption ratio. The high evaporating temperature displayed higher adsorption ratio in the same cycle time, albeit the increase in adsorption ratio was more pronounced for low evaporating temperature with increasing the cycle time. The higher the evaporating temperature, the larger the amount adsorbed that means a greater adsorption heat generated. The heat exchanger could not remove the adsorption heat immediately at 15 °C resulted in the rose in adsorbent temperature which impeded the adsorption kinetics, that's why the VCP and SCP decreased with increasing the cycle time.

Due to the thickness and the void fraction of the packed bed were only about 10 mm and 0.53 respectively, and the high vapor diffusion of ammonia, the mass transfer performance was not the primary limiting factor of VCP and SCP. The heat transfer performance of the adsorbent bed and heat exchanger are the key limiting factors to maximum VCP and SCP. We will endeavor to resolve these problems for further study.

3.4 Durability of MSC30-NH$_3$ adsorption system

The durability of adsorbent is an essential factor concerning the development of sustainable and economic adsorption system. In order to analyze the durability of the MSC30 during the NH$_3$ adsorption/desorption process, the effect of cycle number on adsorption performance of MSC30-NH$_3$ adsorption system was experimentally investigated. 80 consecutive adsorption/desorption cycles with a cycle time of 2000 s were performed by using the apparatus illustrated in Figure 3-13.
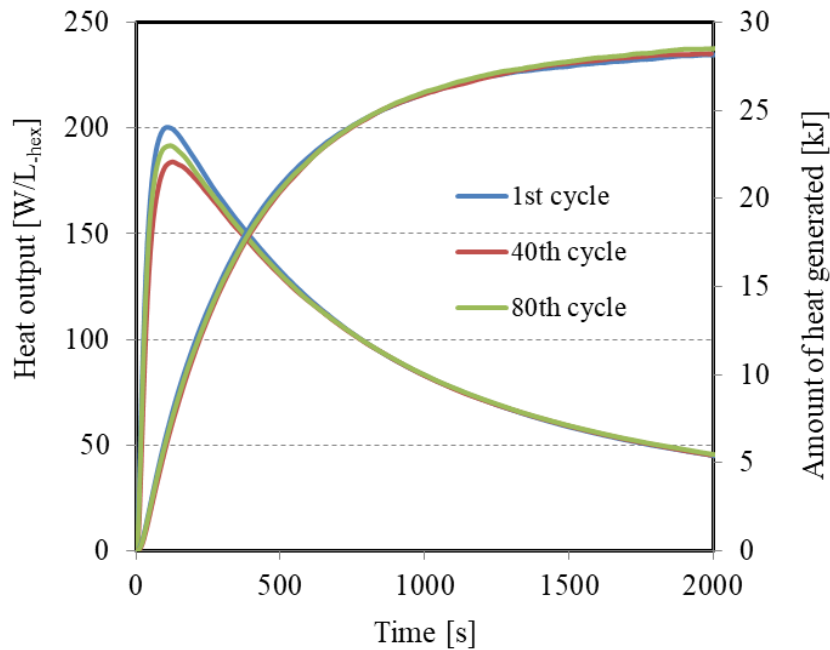
Figure 3-13. The effect of cycle number on adsorption performance.

The evaporating, adsorption/condensing and desorption temperature process were performed at10, 30 and 80 °C, respectively. The flow rate of adsorber heat exchanger was set at 600 mL/min, and the inlet and outlet temperatures were measured to calculate volumetric heat generation (W/L-heat exchanger) and amount of heat generation (kJ) of the adsorber. The results of the 1st, 40th, and 80th cycle are shown in Figure 3-13. As can be seen from Figure 3-13, no noticeable reduction in volumetric heat generation and the amount of heat generation was observed after 80 consecutive adsorption-desorption cycles. MSC30 behaves excellent reversibility of NH_3 adsorption under the tested conditions. Therefore, this performance could make MSC30 an attractive and promising candidate as the adsorbent for NH_3 adsorption refrigeration in the practical application.

3.5 Summary

An activated carbon-NH_3 adsorption refrigeration system with high ability and long durability is proposed. The performance of NH_3 refrigeration system at various evaporating temperatures and cycle times were experimentally investigated. The major conclusions can be summarized as follows.

(1) MSC30 had an excellent adsorption capacity of NH_3 due to it possessed both higher specific surface area and higher pore volume than the other tested activated carbons.

(2) The adsorption isotherms of NH_3 on MSC30 at 5, 10, and 15 °C could be described by the modified Dubinin-Astakhov equation successfully. The n values obtained were 1.63 ~ 2.07, indicating the existence of a broad micropore size distribution and heterogeneous structure in MSC30.

(3) Isosteric heat of adsorption of MSC30-NH_3 was evaluated by using the Clausius–Clapeyron equation and was found in the range of 1552 to 2317 kJ/kg (with an average value of 1922 kJ/kg) depending on the amount adsorbed.

(4) The cooling performances varied with different evaporating temperatures and cycle times. The COP, VCP, and SCP increased as the evaporating temperature decreased. However, it is hard to satisfy both COP and VCP/SCP at the same cycle time. The COP, VCP, and SCP obtained were 0.35, 109 W/L-heat $_{exchanger}$, and 520 W/kg$_{-absorbent}$, respectively, at the condition of 15 °C and 600s. Results indicated that the system needs improvement on the heat transfer performance in the adsorbent packed bed and the heat exchanger.

(5) A long-term operation without degradation for MSC30-NH_3 adsorption/desorption process was experimentally demonstrated from the repetition operations, showing the MSC30-NH_3 is a promising pair for adsorption refrigeration system on the heat transfer performance in the adsorbent packed bed and the heat exchanger.

3.6 Reference

［1］　　Hu, E.J. (1998) A Study of Thermal Decomposition of Methanol in Solar Powered Adsorption Refrigeration Systems. Solar Energy, 62, 325-329.

［2］　　Tamainot-Telto, Z., Metcalf, S.J., Critoph, R.E., Zhong, Y. and Thorpe, R. (2009) Carbon-Ammonia Pairs for Adsorption Refrigeration Applications: Ice Making, Air Conditioning and Heat Pumping. International Journal of Refrigeration, 32, 1212-1229.

［3］　　Hirota, Y., Kobayashi, N., Watanabe, F., Hasatani, M., Uda, S. and Inaoka, H. (2008) Development of the Adsorber in the Ammonia and AC Combination Adsorption Heat Pump. Journal of Japan Society of Energy and Resources, 29, 35-41.

［4］　　Sadhikh, M. and Skaria, J.J. (2016) Development of Waste Heat Fired Activated Carbon Ammonia Adsorption Chiller. International Journal of Thermal and Environmental Engineering, 11, 131-135.

［5］　　Wójtowicz, M.A., Cosgrove, J.E. and Serio, M.A. (2015) Adsorption of Ammonia on Regenerable Carbon Sorbents. 45th International Conference on Environmental Systems, Washington, ICES-2015-179.

［6］　　Pal1, M., Boer, R. and Veldhuis, J. (2013) Experimental Setup for Determining Ammonia-Salt Adsorption and Desorption Behavior under Typical Heat Pump Conditions: Experimental Results. International Symposium on Innovative Materials for Processes in Energy Systems, Fukuoka, IMPRES2013-084.

［7］　　Ammitzbøll, A.L., Lysgaard, S., Klukowska, A., Vegge, T. and Quaade, U.J. (2013) Surface Adsorption in Strontium Chloride Ammines. The Journal of Chemical Physics, 138, Article ID: 164701. https://doi.org/10.1063/1.4800754

［8］　　Duenas, C., Pilatowskya, I., Romeroa, R.J., Oskama, A. and Finck, P.A. (2001) Dynamic Study of the Thermal Behavior of Solar Thermochemical Refrigerator: Barium Chloride-Ammonia for Ice Production. Solar Energy Materials and Solar Cells, 70, 401-413.

［9］　　Sharonov, V.E., Veselovskaya, J.V. and Aristov, Y.I. (2006) Ammonia Sorption on Composites "CaCl2 in Inorganic Host Matrix": Isosteric Chart and Its Performance. International Journal of Low-Carbon Technologies, 1, 191-200.

［10］　Chen, C.J., Wang, R.Z., Wang, L.W. and Lu, Z.S. (2007) Studies on Cycle Characteristics and Application of Split Heat Pipe Adsorption Ice Maker. Energy Conversion and Management, 48, 1106-1112.

［11］　Goshayeshi, H.R., Gewad, M. and Nazari, H. (2015) Investigation on Evaluation of a Solar Intermittent Refrigeration System for Ice Production with Ammonia/Calcium Chloride and Activated. Energy and Power Engineering, 7, 433-439.

［12］　Tokarev, M.M. (2010) Novel Ammonia Sorbents "Porous Matrix Modified by Active Salt" for Adsorptive Heat Transformation: 2. Calcium Chloride in ACF Felt. Applied Thermal Engineering, 30, 845-849.

［13］　Li, S.L., Xia, Z.Z., Wu, J.Y., Li, J., Wang, R.Z. and Wang, L.W. (2010) Experimental Study of a Novel CaCl2/Expanded Graphite-NH3 Adsorption Refrigerator. International Journal of Refrigeration, 33, 61-69.

［14］　Wang, L., Chen, L., Wang, H.L. and Liao, D.L. (2009) The Adsorption Refrigeration Characteristics of Alkaline-Earth Metalchlorides and Its Composite Adsorbents. Renewable Energy, 34, 1016-1023.

［15］　Wang, L.W., Metcalf, S.J., Critoph, R.E., Thorpeb, R. and Tamainot-Telto, Z. (2012) Development of Thermal Conductive Consolidated Activated Carbon for Adsorption Refrigeration. Carbon, 50, 977-986.

［16］　Parash Goyal, Prashant Baredar, Arvind Mittal, Ameenur. R. Siddiqui. Adsorption refrigeration technology–An overview of theory and its solar energy applications. Renewable and Sustainable Energy Reviews 53 (2016) 1389–1410.

［17］　Shaobin Yang, Haoquan Hu, Guohua Chen. Preparation of carbon adsorbents with high surface area and a model for calculating surface area. Carbon 40 (2002) 277–284.

［18］　Thommes, Matthias, et al. Physisorption of gases, with special reference to the evaluation of surface area and pore size distribution (IUPAC Technical Report). Pure and Applied Chemistry, 2015, 87.9-10: 1051-1069.

［19］　Dada, A.O, Olalekan, A.P, Olatunya, A.M., DADA, O. Langmuir, Freundlich, Temkin and Dubinin-Radushkevich isotherms studies of equilibrium sorption of Zn2+ unto phosphoric acid modified rice husk. Journal of Applied Chemistry. Volume 3, Issue 1(Nov.- Dec. 2012), PP 38-45.

［20］　A. EBRAHIMIAN, E. SABERIKHAH, M. S. EMAMI and M. SOTUDEH. Study of biosorption parameters: isotherm, kinetics and thermodynamics of basic blue 9 biosorption onto foumanat tea waste, Cellulose Chem. Technol., 48 (7-8), 735-743 (2014).

［21］　CHEN, Lei, et al. Application of Langmuir and Dubinin–Radushkevich models to estimate methane sorption capacity on two shale samples from the Upper Triassic Chang 7 Member in the southeastern Ordos Basin, China. Energy Exploration & Exploitation, 2017, 35.1: 122-144.

［22］　Rangabhashiyam, S., Anu, N., Giri, N., Selvaraju, N. (2014). A Novel approach of the modified BET Isotherm towards continuous column study. Journal of scientific & Industrial research. Vol. 73, July 2014, pp. 489-494.

［23］　SAEIDI, Navid; PARVINI, Mehdi. Accuracy of Dubinin-Astakhov and Dubinin-Radushkevich Adsorption Isotherm Models in Evaluating Micropore Volume of Bentonite. PeriodicaPolytechnica Chemical Engineering, [S.l.], v. 60, n. 2, p. 123-129, oct. 2015. ISSN 1587-3765.

［24］　Vinod Kumar Singh, E. Anil Kumar. Anil. Experimental investigation and thermodynamic analysis of CO_2 adsorption on activated carbons for cooling system. Journal of CO_2 Utilization, 2017, 17: 290-304.

［25］ Tamainot-Telto Z. , R.E. Critoph, Adsorption refrigerant using monolithic carbon–ammonia pair, International Journal of Refrigeration 20 (2) (1997) 146–155.

［26］ CORNELL, J. A.; BERGER, R. D. Factors that influence the value of the coefficient of determination in simple linear and nonlinear regression models. Phytopathology, 1987, 77.1: 63-70.

［27］ Do DD. Pure component adsorption in microporous solids. In: Adsorption Analysis: Equilibria and Kinetics. London: Imperial College Press; 1998. Chapter 4 161~162.

［28］ Sircar, S.; Rao, M. B., in: Surfaces of Nanoparticles in Porous Materials, Schwarz, J.A., Contescu, C., Ed., Marcel and Dekker, New York, 1999, 501-518.

［29］ J. Julis. Differential heats of adsorption. Chem. zvesti 29 (5) 653-659 (1975).

［30］ Eliza Wolak and Stefan Kraszewski. An overview of adsorptive processes in refrigeration systems. E3S Web of Conferences 10, 00104 (2016)

Chapter 4. Mechanical booster pump - assisted adsorption chiller cycle

Since the Industrial Revolution, energy consumption has increased. This has led to an increase in the amount of industrial waste heat as well. Cogeneration systems have attracted increasing attention over the past two decades due to the high energy efficiency (e.g. 80% when a gas turbine with waste heat boiler is used). The energy efficiency of cogeneration system can also be improved with the use of a heat energy conversion apparatus. Adsorption chiller, as one of the heat energy conversion apparatus, can use low-temperature heat source of 60 °C ~ 100 °C to generate the desired cooling effect for reducing air-conditioning loads. The refrigeration cycle generates the cooling effect by means of adsorption, absorption, and chemical reaction phenomena [1-3]. In particular, the adsorption chiller cycle has recently been receiving a lot of attention. The adsorption chiller cycle can be used to store waste heat and supply cold energy at low temperatures. Water-zeolite [4], Water-silica gel and Ammonia-activated carbon pairs [5] are some of the most common refrigerant-adsorbent pairs used in adsorption chillers. An adsorption chiller cycle using H_2O or NH_3 refrigerant is considered to be an environment-friendly product. In a previous study, Kakiuchi et al. [6] introduced a new Functional Adsorbent Materi-al-Zeolite 01 (FAM-Z01), which is an AFI-type structure Ferroaluminophoshate Ze-olite (FAPO-5) with iron content of 2 ~ 8 mol% [6]. It was suggested that the adsorption capacity of FAM-Z01 was four times than that of silica gel at a desorption temperature of 60 °C. However, the adsorption chiller cycle still has a few problems in practical use; by reason of the cooling power per unit volume of the adsorber and the COP are smaller than that of absorption chiller or vapor compression chiller.

4. 1 Proposal of hybrid adsorption chiller with mechanical booster pumps

To solve the problems associated with the adsorption chiller cycle, we proposed a hybrid adsorption chiller which contained a mechanical booster pump (MBP) in the adsorption process or desorption process. Figure 4-1 shows the schematic diagram of the hybrid adsorption chiller cycle. It consists of an evaporator, a condenser, an MBP and an

adsorber. All the units are connected under reduced pressure. The MBP is set either between the evaporator and the adsorber or between the adsorber and the condenser. The adsorption core which is installed in the adsorber consists of a heat exchanger filled with adsorbents. The heat associated with the adsorption or desorption phenomenon is removed or supplied by heat exchanger. The adsorption chiller cycle consists of an adsorption process and a desorption process. In the adsorption process, the refrigerant vapor moves from the evaporator to the adsorber, and then be adsorbed. In the desorption process, the desorption heat is supplied to the adsorber, and the desorbed refrigerant vapor moves to the condenser. In the hybrid cycle, MBP, which runs on electricity, pumps the refrigerant vapor from the evaporator to the adsorber to increase the adsorber pressure of vapor in adsorption cycle or pumps the refrigerant vapor from the adsorber to the condenser to decrease the adsorber pressure of vapor in desorption cycle. The change of pressure improves the adsorption capacity of the adsorbent.

Figure 4-2 shows the adsorption isotherms of water on FAM-Z05. From Figure 4-2 ①, it can be seen that FAM-Z05 can generate 15 °C cold heat at the desorption temperature of 55 °C. However, it cannot generate 10 °C cold heat when it desorbs at 50 °C or less (②). On the other hand, in the hybrid adsorption cycle, for example when the evaporator temperature is 10 °C, the refrigerant vapor from the evaporator at the saturation pressure of 1.2kPa can be compressed by the MBP, when the adsorber pressure rises to 1.7kPa, the amount of adsorption is increased and has the same value as the condition that the evaporator temperature is 15 °C without MBP. In the hybrid desorption cycle, desorption can take place when the vapor pressure of the adsorber is depressurized to 1kPa at 50 °C by MBP. The amount of desorption is equal to that of desorption under the condition of desorption temperature is 55 °C without MBP. In this way, we can use MBP to expand the amount of adsorption or desorption by increasing or decreasing the vapor pressure of the adsorber. Therefore, the hybrid chiller cycle can be used at a large range of operation temperatures.

Figure 4-1. Schematic diagram of hybrid adsorption chiller cycle with MBP.

Figure 4-2. Adsorption isotherms of water on FAM-Z05.

In this study, we investigated the laboratory scale hybrid chiller cycle which consists mainly of an MBP and an adsorber with the FAM-Z05 adsorption core. We evaluated the cooling output and desorption heat input of the hybrid chiller cycle and researched the effect of the input electrical power of the MBP on the performances of hybrid cycle.

4.2 Experimental procedure of hybrid adsorption chiller with mechanical booster pumps

Figure 4-3 shows the schematic diagram of the experimental apparatus. Falling liquid film heat exchangers were used in the evaporator and the condenser, which had high heat transfer performance. Figure 4-4 shows the adsorption cores in the adsorber. Three pairs of adsorption cores were connected in series in the adsorber, and each pair was composed of two flat webbed tube and corrugated fin heat exchangers in parallel and FAM-Z05, had an average particle diameter of 5 μm, was coated around the tubes and fins of heat exchangers by epoxy binder. The coating thickness of adsorbent was 100 μm. MBP (MBS-052 type, ULVAC Inc.) was connected with stainless tubes and the rotating speed was controlled by Lab View (National Instrument Inc.). When MBP was driven, we measured the electrical power consumption of it.
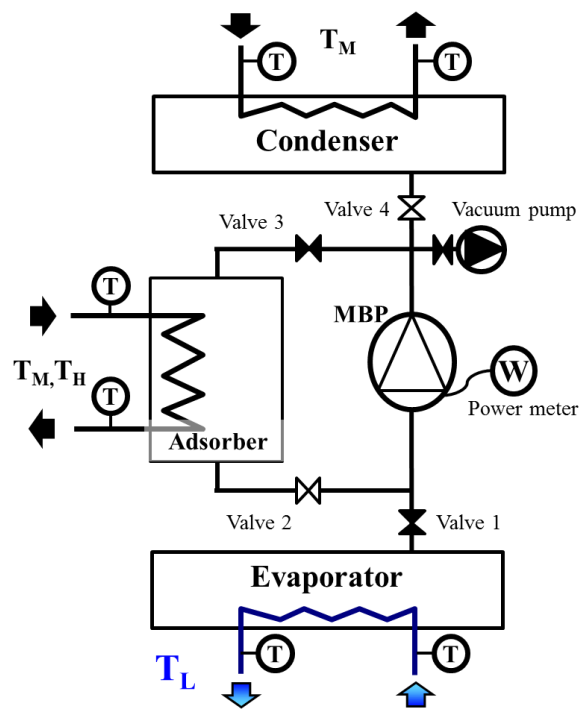
Figure 4-3. Schematic diagram of hybrid adsorption chiller cycle with MBP.

Figure 4-4. Photo of adsorption cores in the adsorber

Table 4-1. Experimental conditions of hybrid adsorption chiller cycle with MBP

process	Adsorption process	Desorption process
Evaporator	10,15 °C	15 °C
Adsorption temperature	30 °C	30 °C
Desorption temperature	60 °C	60,55,50,45 °C
Condenser	30 °C	30 °C
MBP power	20,60,100 W	50,60,100 W

The experimental conditions are summarized in Table 4-1. The condenser temperature was maintained at 30 °C by thermostat bath. The evaporator temperature was set at 10 °C and 15 °C. The desorption temperature was set at 45 °C, 50 °C, 55 °C and 60 °C. The flow rate of the heat transfer fluid of all the units was set at a constant value of 4.5 L/min. The temperature of the fluid flow was measured by a Platinum resistance temperature sensor. This was followed by the calculation of cooling heat output W_{eva} (W), desorption heat input W_{des} (W), amount of cooling heat Q_{eva} (J), amount of desorption heat Q_{des} (J), COP based on electricity input $COP_{electricity}$, COP based on heat input COP_{heat}, and COP based on total energy input (the sum of electricity and heat) COP_{total} using the following equations:

$$W_{eva} = Cp_{fluid} \cdot \rho_{fluid} \cdot F_{fluid} \cdot \Delta T_{eva,average} \tag{4-9}$$

$$W_{des} = Cp_{fluid} \cdot \rho_{fluid} \cdot F_{fluid} \cdot \Delta T_{des,average} \tag{4-10}$$

$$Q_{eva\ or\ des} = \int_0^t W_{eva\ or\ des} dt \tag{4-11}$$

$$COP_{electricity} = \frac{Q_{eva}}{Q_{electricity}} \tag{4-12}$$

$$COP_{heat} = \frac{Q_{eva}}{Q_{des} + Q_s} \tag{4-13}$$

$$COP_{total} = \frac{Q_{eva}}{Q_{des} + Q_s + Q_{electricity}} \tag{4-14}$$

where Cp_{fluid} is the specific heat of heat exchange fluid at constant pressure (kJ/kg/K), ρ_{fluid} is the density of heat exchange fluid (kg/m^3), F_{fluid} is the volume flow rate of heat exchange fluid (L/min), $\Delta T_{eva,average}$ is the average temperature difference between heat exchange fluid at the inlet and outlet of evaporator (K), $\Delta T_{des,average}$ is the average temperature difference between heat exchange fluid at the inlet and outlet of desorber (K), and Q_s is the sensible heat evaluating by the following equation:

$$Q_s = \int_{T_M}^{T_H} \left(mq_{ads}Cp_{water,l} + mCp_{ad} + m_{hex}Cp_{hex} \right) dT \tag{4-15}$$

where q_{ads} is the amount adsorbed (kg-adsorbate/kg-adsorbent), m is the mass of adsorbent (kg), m_{hex} is the mass of heat exchanger (m^3), $Cp_{water,l}$ is the specific heat of liquid water at constant pressure (kJ/kg/K), Cp_{ad} is the specific heat of adsorbent at constant pressure (kJ/kg/K) and Cp_c is the specific heat of heat exchanger at constant pressure (kJ/kg/K).

4.3 Effects of MBP on adsorption process

Figure 4-5 shows the cooling heat output change over time at evaporator temperature of 15 °C and 10 °C, respectively. Figure 4-6 shows the variation of adsorber pressure with time at 15 °C. The valve 1 and 3 were opened and MBP was switched on at 0 s. In Figure 4-5, the cooling heat output without MBP is also indicated. The maximum cooling heat

95

output obtained without MBP was 250 W. On the other hand, the maximum cooling heat output with MBP at the input electrical power of 120 W was 380 W. The obtained cooling heat output increased with increasing the input electrical power of MBP. The refrigerant vapor from the evaporator was compressed by MBP, and then was adsorbed by FAM-Z05. The adsorber pressure increased quickly by using MBP resulted in a faster adsorption rate and a higher cooling heat output. However, when the input electrical power of MBP was 20 W, the cooling heat output was lower than that of without MBP. In Figure 4-6, the adsorber pressure of 1.7 kPa is the saturation pressure at 15 °C. The adsorber pressure was higher than the evaporator pressure when the MBP power was high. Time taken to reach the evaporator pressure was 2300 s at 20 W. The vapor transport between the evaporator and the adsorber was hampered by MBP, due to the rotational speed of MBP was extremely low at 20 W. It resulted in a very slow vapor transport rate, which was slower than that of without MBP and the adsorption rate. Figure 4-7 shows the amount of cooling heat in the adsorption process. As can be seen from the results, the amount of cooling heat obtained with MBP was more than twice as much as that of without MBP at 15 °C. Furthermore, it was possible to obtain cooling heat at the evaporator temperature of 10 °C, which cannot be acquired without MBP. Therefore, the hybrid cycle with MBP can improve the cooling heat at low evaporator temperature was confirmed. Figure 4-8 shows the effect of input electrical power of MBP on $COP_{electricity}$ which is the ratio of the cooling heat to the input electrical power of MBP. As can be seen from the results, the $COP_{electricity}$ decreased with increasing the input electrical power of MBP. When the evaporator temperature was 15 °C, the $COP_{electricity}$ for the input electrical power of 20 W, 60 W, and 120 W was 7.0, 5.0 and 3.0, respectively. In addition, the $COP_{electricity}$ at the evaporator temperature of 10 °C exhibited the same tendency as the results of 15 °C. When the input electrical power of MBP was high, the $COP_{electricity}$ of the hybrid cycle was less than or equal to that of mechanical chiller cycle. Due to the saturation pressure of water is lower than the conventional refrigerants, such as HFC and ammonia, which are commonly used in the mechanical chiller.
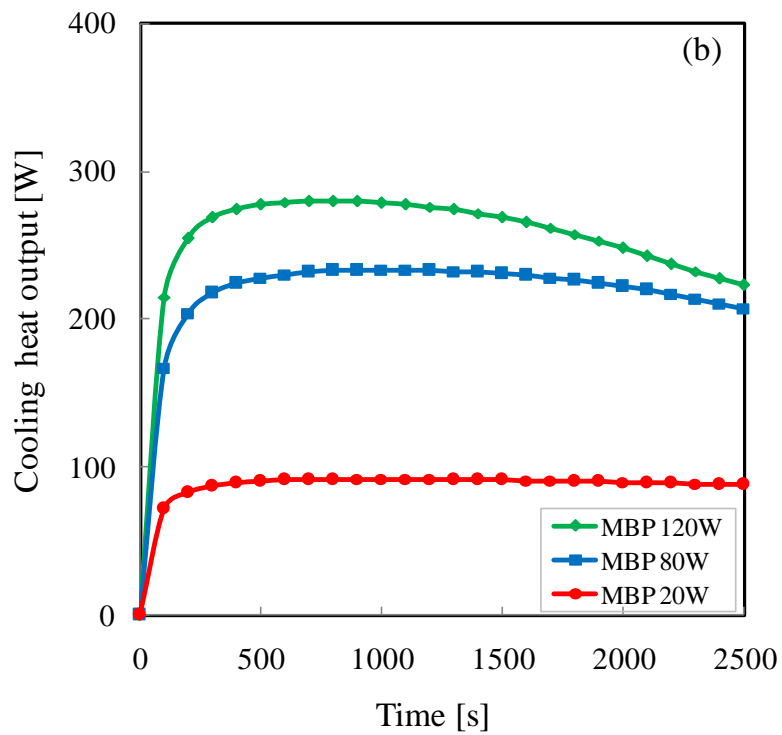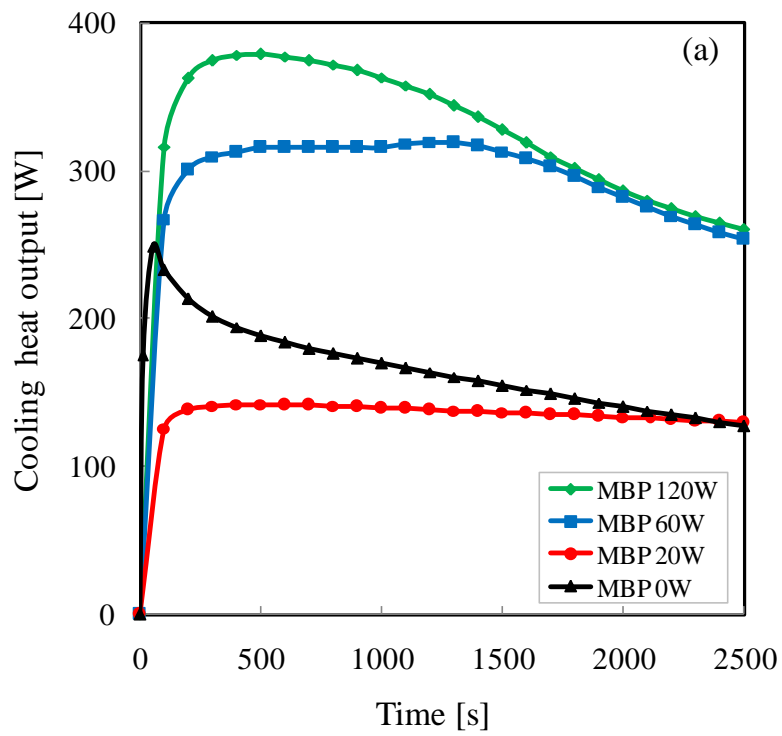
Figure 4-5. Time variation of cooling heat output for different MBP powers at 15 °C (a) and 10 °C (b)
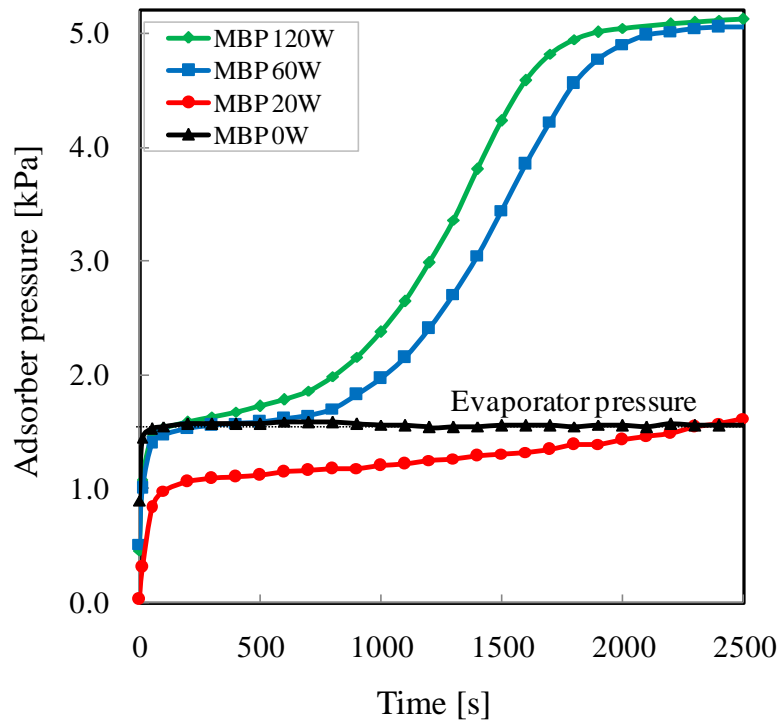
Figure 4-6. Effect of MBP power on the adsorber pressure in adsorption process.
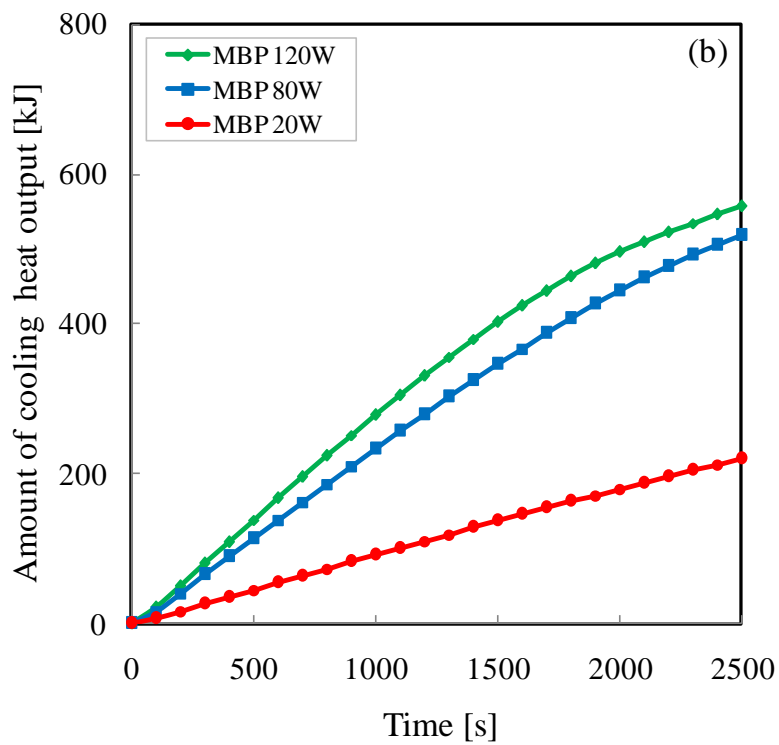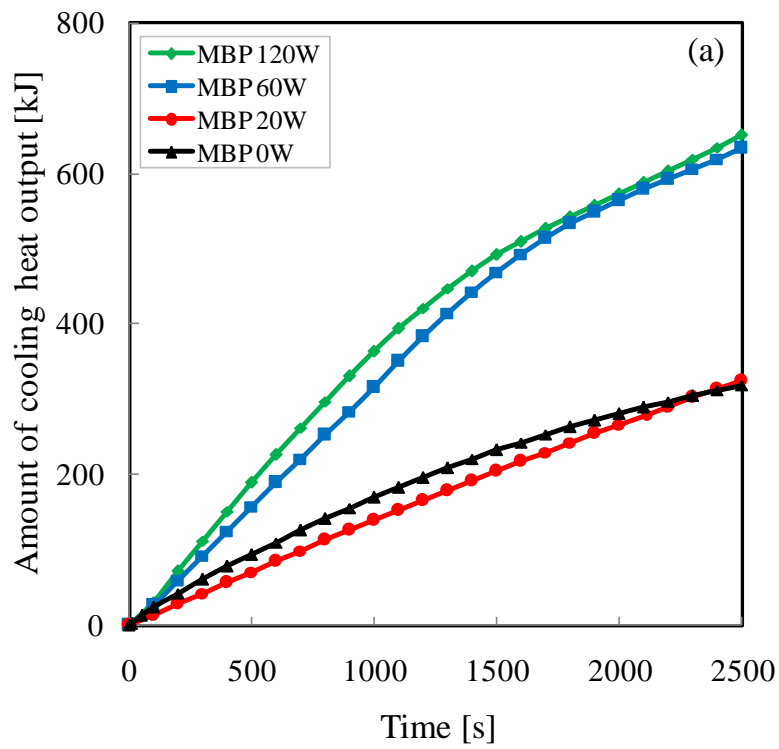
Figure 4-7. Time variation of cooling heat for different MBP powers at 15 °C (a) and 10 °C (b)
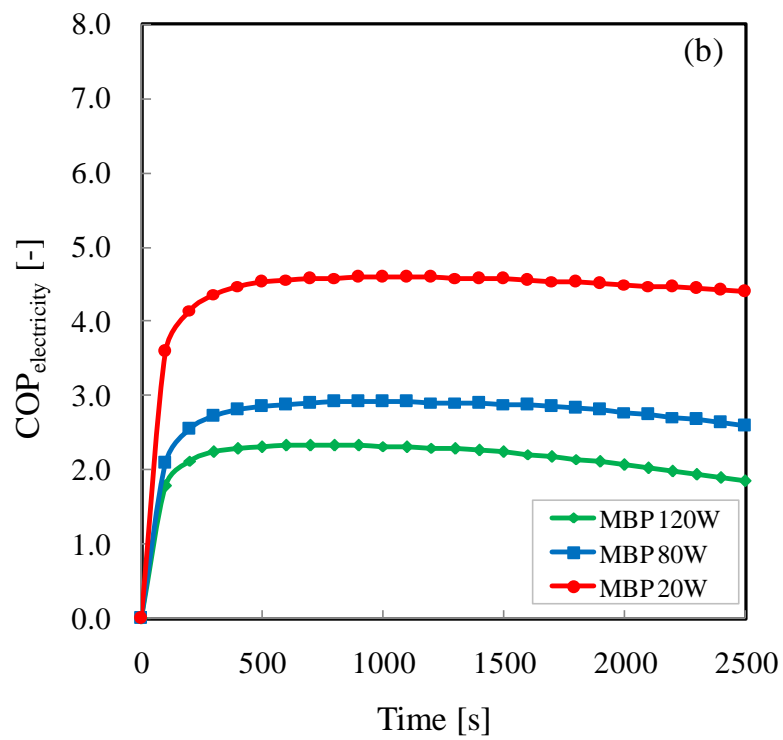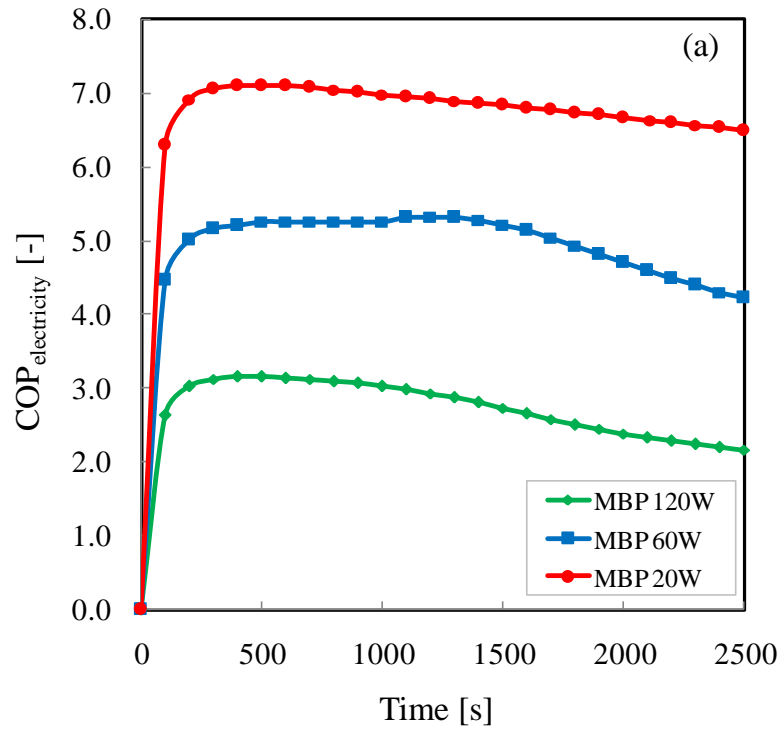
Figure 4-8. Effect of MBP power on the $COP_{electricity}$ at the evaporator temperature of 15 °C (a) and 10 °C (b).
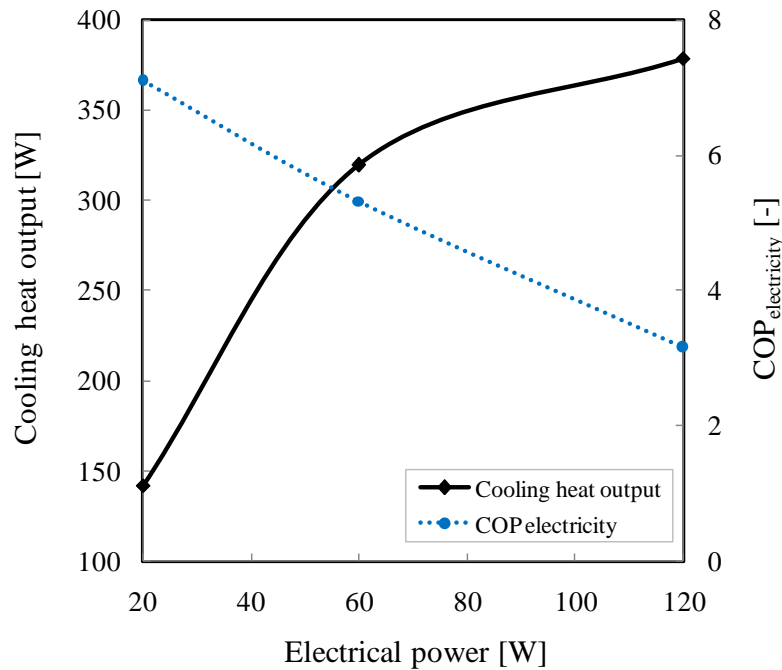
Figure 4-9. Effect of MBP power on the cooling heat output and the $COP_{electricity}$ at 15 °C.

Figure 4-9 shows the effect of the input electrical power of MBP on the maximum cooling heat output and $COP_{electricity}$ at the evaporator temperature of 15 °C. As shown in Figure 4-9, the cooling heat output increased as the input electrical power of MBP increased, whereas the $COP_{electricity}$ displayed the opposite trend. The tradeoff between cooling heat output and $COP_{electricity}$ was thus confirmed.

Figure 4-10 and Figure 4-11 illustrate the effect of input electrical power of MBP on COP_{heat} and COP_{total}, respectively. As shown in Figure 4-10, COP_{heat} increased with the increase of input electrical power and obtained COP_{heat} values of 0.69 and 0.68 at 1500 s that is 1.2 times and 1.1 times higher than that of without MBP (0.62) at 15 °C when the input electrical power was 60 W and 120 W, respectively. At 10 °C, COP_{heat} of about 0.67, 0.66, and 0.55 could be obtained at 1500s when the input electrical power was 20 W, 80 W and 120 W, respectively. The COP_{heat} values obtained at higher input electrical power (60 W and 120 W for 15 °C, 80 W and 120 W for 10 °C) were almost the same, indicating that the input electrical power of 60 W was sufficient at both cases. This could also be confirmed from Figure 4-11 that COP_{total} decreased with the increase of operation time

101

when the input electrical power at 60 W and 120 W due to the adsorption capacity of adsorbent nearly reached the saturation state. Consequently, there is an optimum input electrical power for acquiring a maximum cooling power and COP_{total} at different conditions.
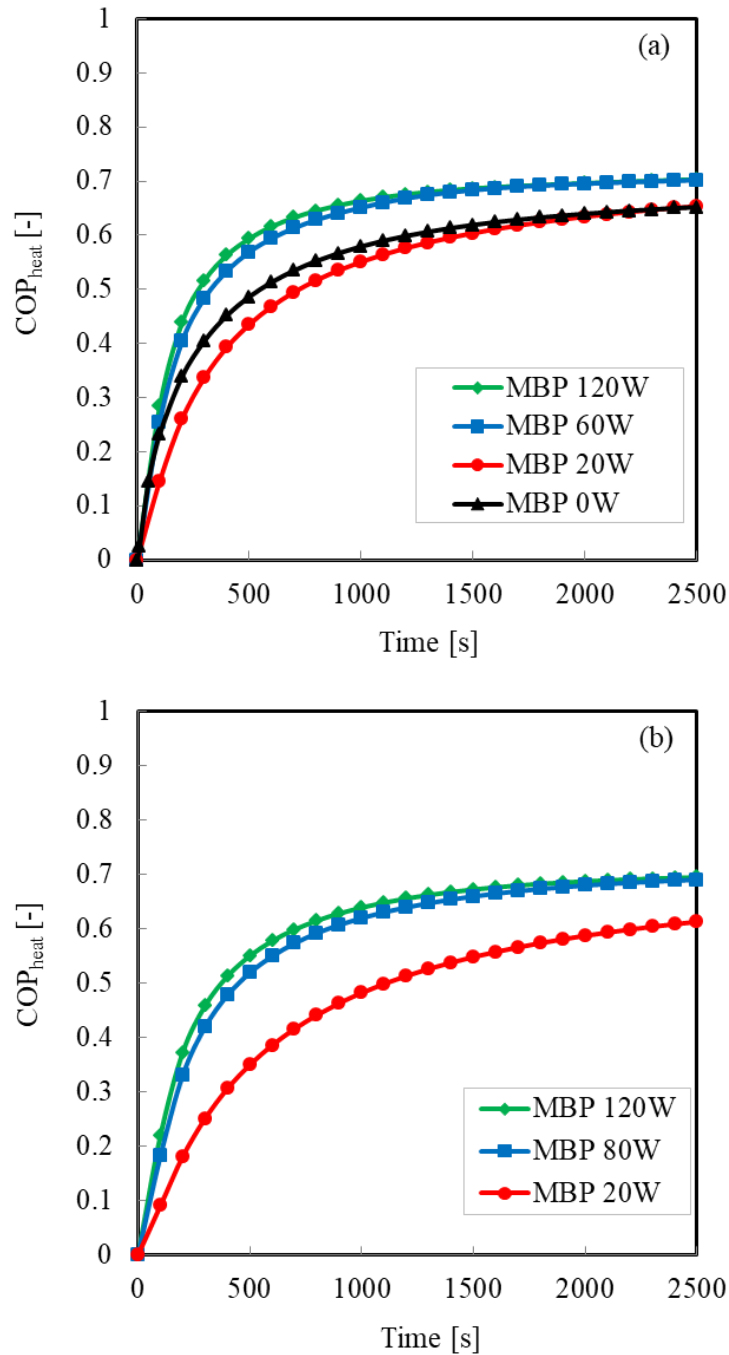

Figure 4-10. Effect of MBP power on the COP_{heat} at the evaporator temperature of 15 °C (a) and 10 °C (b).
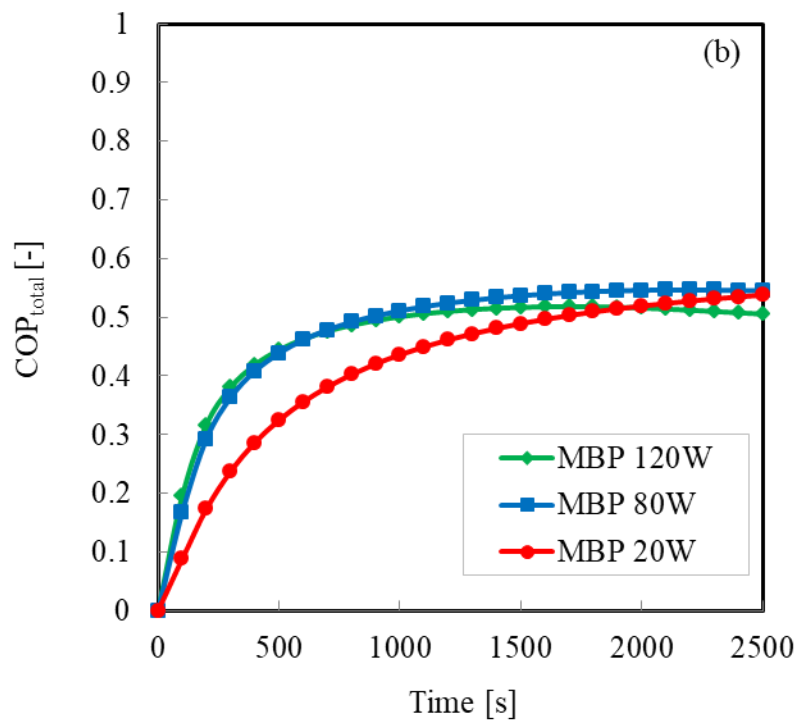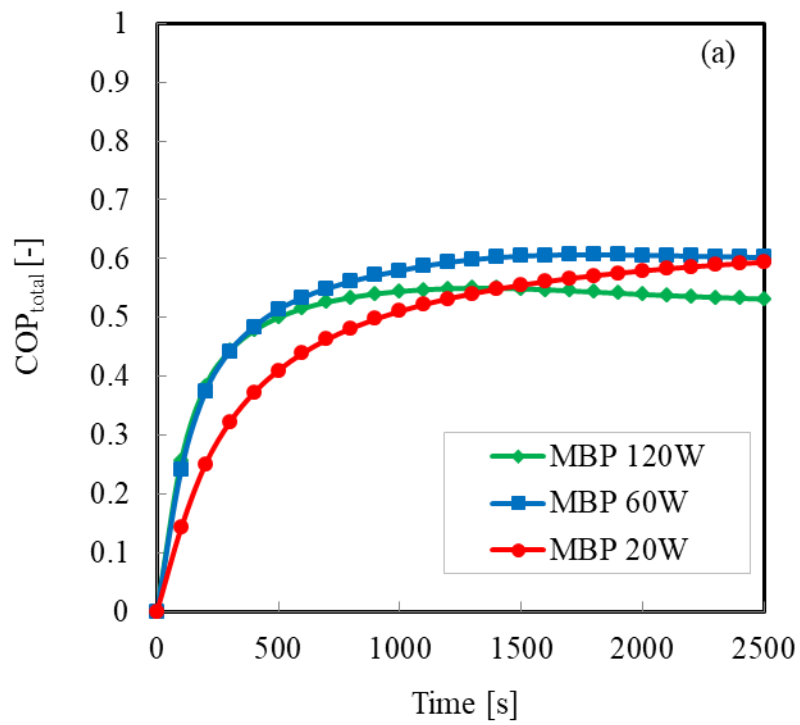
Figure 4-11. Effect of MBP power on the COP_{total} at the evaporator temperature of 15 ℃ (a) and 10 ℃ (b).

4.4 Effects of MBP on desorption process

We also studied the desorption process without and with MBP. The experimental apparatus was the same as that of the adsorption process. The desorption process was carried out after the adsorption process which had been conducted under the evaporator temperature of 15 °C without MBP. Closed the valve 1 and 3, and then increased the adsorber temperature from the adsorption temperature to the desorption temperature. When the adsorber pressure became equal to or higher than the condenser pressure, valve 3 and 4 were opened so that the refrigerant vapor can transport into the condenser spontaneously. On the other hand, when the MBP was running and the valve 2 and 4 were opened instead of valve 3 and 4, the refrigerant vapor was compressed into the condenser by MBP. The desorption temperature was set at 50 °C and 60 °C for the cycle without MBP, 55 °C, 50 °C and 45 °C for the cycle with MBP.
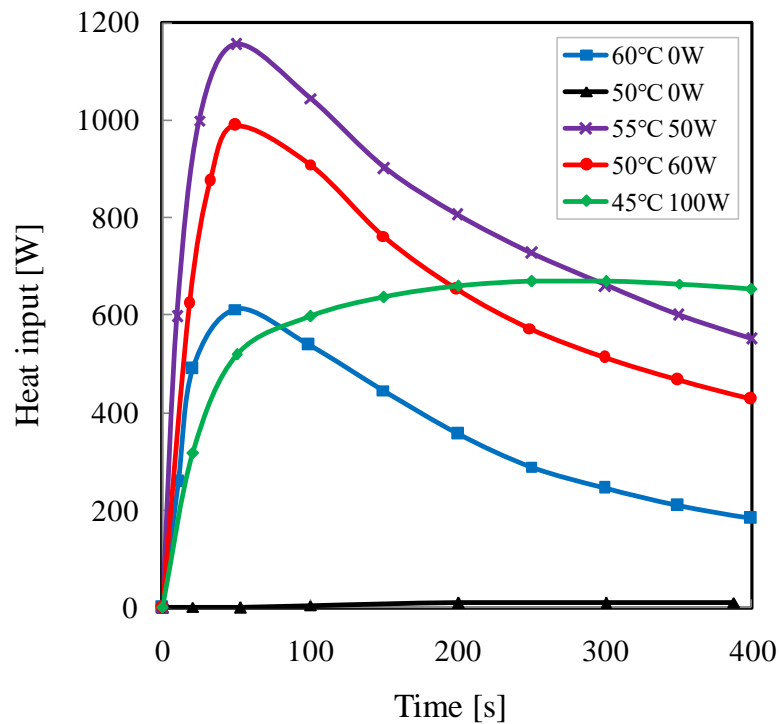

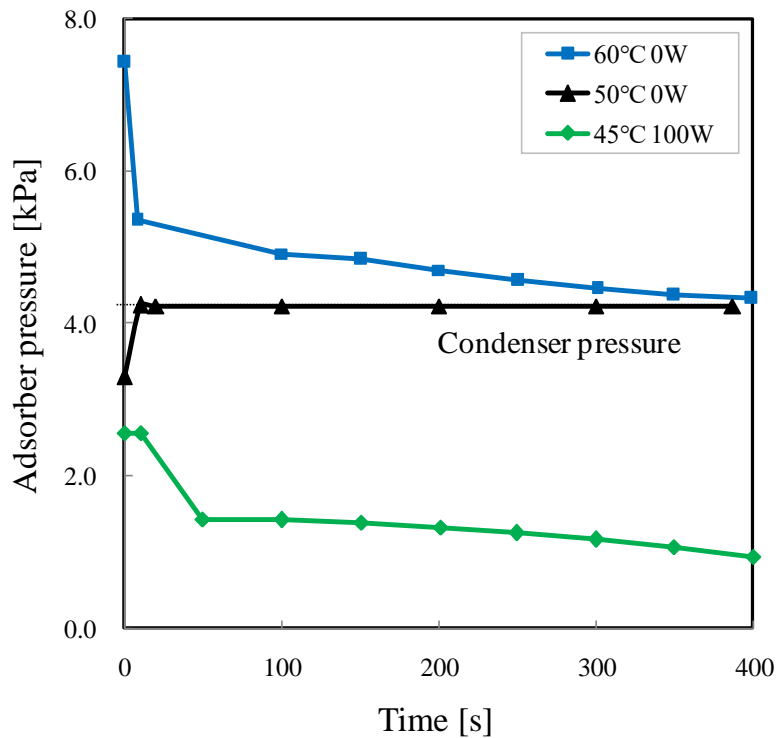**Figure 4-12.** Time variation of desorption heat input for different MBP powers.

Figure 4-13. Effect of MBP power on the adsorber pressure in the desorption process.

Figure 4-12 shows the variation of desorption heat input with time. 0 s of the horizontal axis corresponds to the timing of valve opening and MBP running. The results show that the desorption of refrigerant could proceed without MBP at 60 °C, reaching a maximum desorption heat input of approximately 600 W. However, no desorption heat input can be obtained at 50 °C without MBP, due to the poor adsorption capacity at this desorption temperature as can be seen from Figure 4-2. On the other hand, high desorption heat input was obtained with MBP at the desorption temperature of 50 °C and 55 °C. When the input electrical power of MBP was 50 W, the maximum desorption input power of about 1150 W was obtained at 50 °C, which was higher than that of at 60 °C without MBP. The higher the input electrical power of MBP the lower the desorprion temperature can be used. Figure 4-13 shows the adsorber pressure change during desorption process. In the desorption process, the vapor transport rate is proportional to the pressure difference between the absorber and condenser. As can be seen from Figure 4-13, when valve 3 and 4 were opened, the adsorber pressure decreased to the condenser pressure immediately at 60 °C without MBP and the desorption heat input was obtained. However, due to the

adsorber pressure at 50 °C was lower than the condenser pressure, when valve 3 and 4 were opened, the refrigerant vapor transported from condenser to adsorber, the opposite transport direction to 60 °C, resulted in the desorption of refrigerant could not proceed and no heat input was obtained. It would have been the same situation as at 50 °C if MBP had not been used in the desorption process at 45 °C. When MBP was operating at 100 W, the vapor from adsorber was compressed into condenser by MBP, and therefore the desorption heat input was acquired at 45 °C.
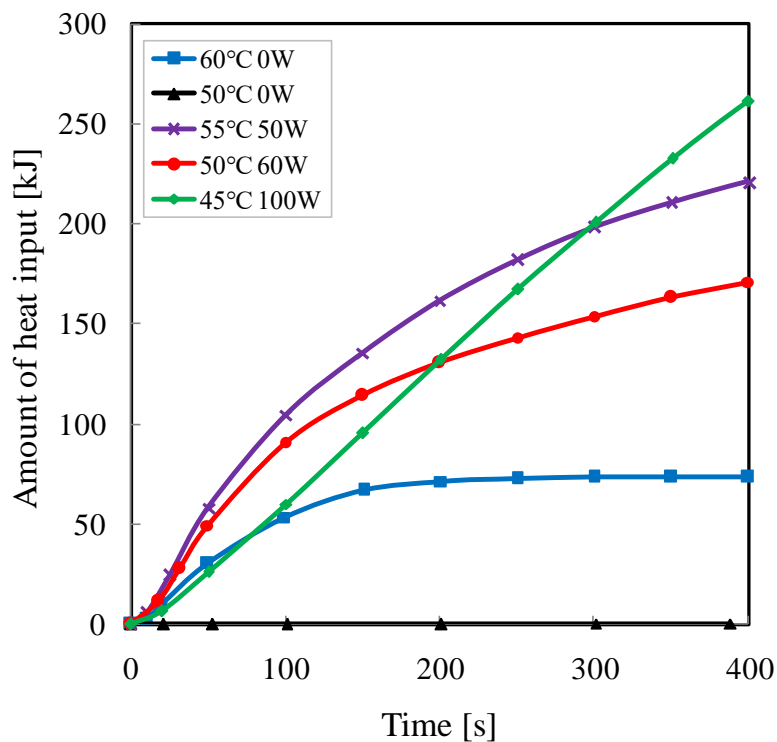
Figure 4-14. Time variation of amount of desorption heat for different MBP powers.

Figure 4-14 shows the amount of desorption heat. From Figure 4-14, it can be seen that the desorption heat could be obtained in less time by operating the MBP with an input electrical power of 100 W, at the low desorption temperature of 45 °C. Thus, we confirmed that in comparison with the cycle without MBP, hybrid cycle could obtain cooling heat at lower desorption temperature.

4.5 Summary

A lab-scale FAM-Z05/H_2O type adsorption chiller cycle with and without MBP was analyzed. The major conclusions can be summarized as follows.

(1) The cooling heat output and the amount of cooling heat were improved and increased with the input electrical power of MBP. Moreover, the adsorption chiller could be operated at a lower evaporator temperature lever. On the other hand, COP electricity decreased with increasing the input electrical power of MBP and was less than or equal to mechanical chiller cycle at the high input electrical power.

(2) The desorption heat input and the amount of heat input were improved and increased with the input electrical power of MBP. Desorption cycle could be effectively driven by a relatively low desorption temperature such as 45 °C, in comparison with the cycle without MBP.

4.6 Reference

［1］　　Wu, W., Wang, B., Shi, W. and Li, X. (2014) Absorption Heating Technologies: A Review and Perspective. Applied Energy, 130, 51-71.

［2］　　Demir, H., Mobedi, M. and Uˇlku, S. (2008) A Review on Adsorption Heat Pump: Prob-lems and Solutions. Renewable and Sustainable Energy Review, 12, 2381-2403.

［3］　　Lahmidi, H., Mauran, S. and Goetz, V. (2006) Definition, Test and Simulation of Ther-mochemical Storage Process Adapted to Solar Thermal Systems. Sol. Energy, 80, 883-893.

［4］　　Palomba, V., Vasta, S., Giacoppo, G., Calabrese, L., Gulli`, G., La Rosa, D. and Freni, A. (2015) Design of an Innovative Graphite Exchanger for Adsorption Heat Pumps and Chillers.

［5］   Hirota, Y., Kobayashi, N., Watanabe, F., Hasatani, M., Uda, S. and Inaoka, H. (2008) Development of the Adsorber in the Ammonia and AC Combination Adsorption Heat Pump. Journal of Japan Society of Energy and Resources,29(3), 35-41.

［6］   Kakiuchi, H., Shimooka, S., Iwade, M., Oshima, K., Yamazaki, M., Terada, S., Watanabe, H. and Takewaki, T. (2005) Novel Water Vapor Adsorbent FAM-Z01 and its Applicability to an Adsorption Heat Pump. Kagaku Kogaku Ronbunshu (Japan), 31(5), 361-364.

Chapter 5. Conclusions and future works

5.1 Conclusions

In this study, the development of a high-quality food storage system with low carbon transportation have been experimentally investigated. The main conclusions in this study are shown as follows.

In chapter 2, The laboratory-based hyperspectral imaging system was established to investigate the chlorophyll distribution in three species of plants for evaluating visual quality. The hyperspectral imaging is capable of identifying and mapping chlorophyll pigments and their changes in samples non-destructively. From the hyperspectral images we can acquire the spatially detailed information of chlorophyll distribution in different parts of the samples. After the acquisition of hyperspectral images and data processing, average spectral reflectance extracted from the interested region of sample leaves and calyxes were applied to develop prediction model. NDVIs as a function of the spectral reflectance at the regions of red (670 nm) and red edge (705 nm) were used to evaluate the visual quality change in samples studied. The changes of sample visual quality at different storage conditions were reasonably well evaluated by both the two indices. In contrast, there was a stronger correlation between $NDVI_{705}$ and visual quality rating than that between $NDVI_{670}$ and visual quality rating, indicating the superiority of spectral reflectance in red edge region for visual quality evaluation.

In Chapter 3, an activated carbon-NH_3 adsorption refrigeration system with high ability and long durability is proposed. The performance of NH_3 refrigeration system at various evaporating temperatures and cycle times were experimentally investigated. MSC30 had an excellent adsorption capacity of NH_3 due to it possessed both higher specific surface area and higher pore volume than the other tested activated carbons. The adsorption isotherms of NH_3 on MSC30 at 5, 10, and 15 °C could be described by the modified Dubinin-Astakhov equation successfully. The n values obtained were 1.63 ~ 2.07, indicating the existence of a broad micropore size distribution and heterogeneous structure in MSC30. Isosteric heat of adsorption of MSC30-NH_3 was evaluated by using the

Clausius–Clapeyron equation and was found in the range of 1552 to 2317 kJ/kg (with an average value of 1922 kJ/kg) depending on the amount adsorbed. The cooling performances varied with different evaporating temperatures and cycle times. The COP, VCP, and SCP increased as the evaporating temperature decreased. However, it is hard to satisfy both COP and VCP/SCP at the same cycle time. The COP, VCP, and SCP obtained were 0.35, 109 W/L-heat exchanger, and 520 W/kg-absorbent, respectively, at the condition of 15 °C and 600s. Results indicated that the system needs improvement on the heat transfer performance in the adsorbent packed bed and the heat exchanger. A long-term operation without degradation for $MSC30-NH_3$ adsorption/desorption process was experimentally demonstrated from the repetition operations, showing the $MSC30-NH_3$ is a promising pair for adsorption refrigeration systement on the heat transfer performance in the adsorbent packed bed and the heat exchanger.

In Chapter 4, a lab-scale $FAM-Z05/H_2O$ type adsorption chiller cycle with and without MBP was analyzed. The cooling heat output and the amount of cooling heat were improved and increased with the input electrical power of MBP. Moreover, the adsorption chiller could be operated at a lower evaporator temperature lever. On the other hand, COP electricity decreased with increasing the input electrical power of MBP and was less than or equal to mechanical chiller cycle at the high input electrical power. The desorption heat input and the amount of heat input were improved and increased with the input electrical power of MBP. Desorption cycle could be effectively driven by a relatively low desorption temperature such as 45°C, in comparison with the cycle without MBP.

5.2 Future works

In order to achieve high-quality food storage system with low carbon transportation, following works and suggestions should be done in the future.

1) There is still much work needs to be done for further analysis and statistical assessment of measuring data. For example, enlarge the sample size or increase the number of visual quality inspectors. Moreover, further study should be conducted to explore factors that may contribute to the correlation between NDVI

and visual quality;

2)   The COP of the MSC30-NH$_3$ adsorption/desorption process for effectively utilize the exhaust heat from the food storage system still need to be enhanced compared with vapor-compression refrigeration system. Furthermore, in order to increase the utilization time for the transportation process, the durability of MSC30-NH$_3$ adsorption system should be furtherly confirmed.

Nomenclatures

NDVI	$=$	normalized difference vegetation index	[-]
R	$=$	reflectance	[-]
R^2	$=$	coefficient of determination	[-]
T	$=$	temperature	[K]
T_L	$=$	Evaporating temperature	[K]
T_M	$=$	Adsorption/Condensing temperature	[K]
T_H	$=$	Desorption temperature	[K]
P	$=$	pressure	[Pa]
P_L	$=$	saturated pressure at T_L	[Pa]
P_M	$=$	saturated pressure at T_M	[Pa]
P_H	$=$	saturated pressure at T_H	[Pa]
q	$=$	amount adsorbed	[kg-adsorbate/kg-adsorbent]
q_{ads}	$=$	equilibrium amount adsorbed in adsorption process	[kg-adsorbate/kg-adsorbent]
q_{des}	$=$	equilibrium amount adsorbed in desorption process	[kg-adsorbate/kg-adsorbent]
Δq	$=$	difference of adsorption amount	[kg-adsorbate/kg-adsorbent]
ϕ_{ads}	$=$	relative pressure of adsorption process	[-]
ϕ_{des}	$=$	relative pressure of desorption process	[-]
ε	$=$	porosity	[-]
Q_c	$=$	cooling heat	[kJ]
Q_s	$=$	sensible heat	[kJ]
Q_{des}	$=$	desorption heat	[kJ]
Q_c	$=$	cooling heat	[kJ]
τ_{cycle}	$=$	cycle time	[s]
τ_{pre}	$=$	preparation time	[s]

m	=	mass	[kg]
V	=	volume	[m^3]
ρ	=	density	[kg/m^3]
C_p	=	specific heat	[kJ/kg/K]
ΔH_{eva}	=	heat of evaporation	[kJ/kg]
ΔH_{ads}	=	heat of adsorption	[kJ/kg]
ΔH_{des}	=	heat of desorption	[kJ/kg]
COP	=	coefficient of performance	[-]
SCP	=	specific heat power	[W/kg]
VCP	=	volumetric cooling power	[W/L]

<Subscript>

NIR	=	near infrared region
RED	=	red spectral region
ads	=	adsorption
des	=	desorption
eva	=	evaporation
con	=	condensation
L	=	low
M	=	middle
H	=	high
ad	=	adsorbent
hex	=	heat exchanger
ref	=	refrigerant

Acknowledgements

List of Publications

論文題目	公表の方法及び時期	著者
I. Journal Papers		
1. Research progress of adsorption refrigeration using ammonia as adsorbate	Advance in new and renewable energy Vol, 5, No, 2, pp. 146-150, 2017	Tao Zeng Zhaohong He Noriyuki Kobayashi Hongyu Huang
2. Evaluation of performance of thermal and electrical hybrid adsorption chiller cycles with mechanical booster pumps	Journal of Materials Science and Chemical Engineering Vol, 5, No, 5, pp. 22-32, 2017	Tao Zeng Esaki Takehiro Jun Li Noriyuki Kobayashi Hongyu Huang
3. Performance of an activated carbon-ammonia adsorption refrigeration system	Natural Resources Vol, 8, No, 10, pp. 611-631, 2017	Tao Zeng Hongyu Huang Noriyuki Kobayashi Jun Li
4. Visualization of chlorophyll change in spinach by hyperspectral imaging	Journal of Chemistry and Chemical Sciences Vol, 8, No, 12, pp. 1201-1209, 2018	Tao Zeng Jun Li Noriyuki Kobayashi Hongyu Huang
II. Conference Papers		
1. Ammonia combustion with oxygen-enriched air	10th Asia-Pacific Conference on Combustion, Beijing, China, July, 2015. (Oral)	Jun Li Hongyu Huang Zhaohong He Yugo Osaka Tao Zeng Nannan Wang Noriyuki Kobayashi
2. Activated carbon ammonia adsorption heat pump	SCEJ 47th Autumn Meeting, Hokkaido, Japan, September, 2015. (Oral)	Tao Zeng Noriyuki Kobayashi Hongyu Huang Jun Li